the latter looks at the surface features. The diffraction limit is valid in the former and therefore the resolution is limited. In the latter, a resolution of the order of 20 nm has been demonstrated. Obviously, one may then come to the conclusion that nanoscale objects cannot be imaged by far field techniques. But this is not true. The way in which imaging nanoscale objects is done is through confocal microscopy.

2.4.1 Confocal Microscopy

Confocal means 'having the same focus'. In such a microscope, a point-like light source, generally a laser, is used. This point source is derived by passing the light through a pinhole, which can be conveniently achieved by using a fiber-optic connector. This is directed to the specimen through a beam splitter and an objective, which illuminates a spot. The point of illumination can be moved across the sample by a scanner and there are several ways by which this can be done. The emitted light from the sample, generally fluorescence (or less common scattered light, as in the case of Raman spectroscopy), passes through the detecting pinhole and forms a point-like image on the detector. The light is scanned across the sample to obtain a two-dimensional image or the depth from which the light is collected is varied by moving either the objective or the sample thus giving a three-dimensional image of the sample. All these three points, namely the illumination pinhole, sample spot and the detector pinhole, are optically conjugated together, thus giving the confocal microscope (Fig. 2.21). The confocal microscope is therefore a confocal scanning optical microscope. The optical sectioning aspect is the most important advantage of confocal microscope. The sections can be as thin as the wavelength of light and its spatial resolution of the microscope is the best that can be achieved by using optical microscopy.

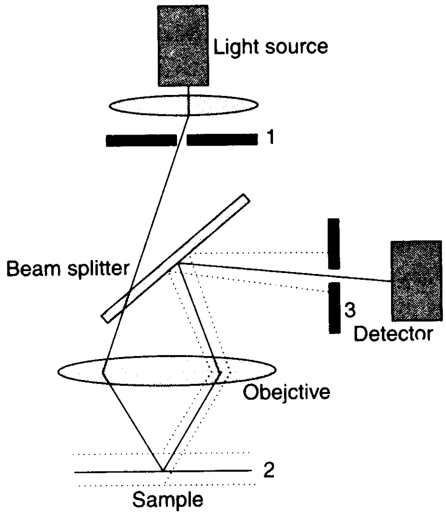

Fig. 2.21 : *Schematic of a confocal microscope. 1 and 3 are confocal pinholes. Light emanating from another plane of the sample, indicated in dotted line, is not detected. 1, 2 and 3 are optically conjugated in the arrangement.*

Collecting the imaging involves scanning the light. The simplest approach would be to move the sample as the optical system is optimized. This process is slow as the piezoelectric scanners take time and real-time observation of processes is impossible. The other approach is to have a set of two mirrors to scan the laser in the *xy* plane, by first doing an *x*-scan and then making a *y*-shift, then an *x*-scan again and so on. The laser beam itself can be split into several smaller beams and all the beams may be simultaneously used for imaging. In this way, each beam needs to be moved only for a short distance for imaging the entire sample. This methodology uses a Nipkow disk, in which thousands of microlenses are mounted on a disk and the light is focused into thousands of pinholes created on another disk. All the beams are focused by the objective simultaneously and the light coming out from the sample is collected through the pinholes and microlenses and detected parallely. The holes can be arranged in a spiral fashion so that the entire space can be scanned by rotating the disk. Increasing the speed of rotation will increase the speed of imaging.

As can be seen in Fig. 2.21, the signal collected from the sample is confined to specific illumination volume by the use of an aperture. Thus the aperture sits at the same focal point of the objective, rejecting all light that comes from other regions. This facilitates localization of the illumination volume. Thus an object whose spatial dimension is smaller than the wavelength of light can be studied by localizing the illumination volume. In this illumination volume, one can look at the fluorescence of a molecule or a quantum dot. These can be part of a living cell or a polymeric composite. Thus direct localization of the illumination volume smaller than the resolution of light microscopy, is possible in the confocal technique.

The principal advantage of confocal microscopy is the image contrast, which is achieved by rejecting light that comes from other focal planes of the sample. The smaller the slit, larger is the rejection, but the overall signal quality decreases in this way.

The most important recent development in confocal is 4pi confocal microscopy. In this technique, two objectives are used to illuminate or collect light from the sample. An interference pattern is created by using the light from the objectives. This pattern has one major central peak and several side lobes. The central peak has a reduced axial spread, which is less than the peak that one would get from a pinhole. Depending on how the interference pattern is created, it is possible to get even an FWHM, which is one-sixth of the wavelength of illumination. This results in increased resolution images by detecting only the central peak, and avoiding the side lobes.

The most important application of confocal microscopy in nanoscience is in the investigation of the interactions of nanosystems with biological components. There are numerous examples of this kind wherein nanoparticles, nanoshells, nanotubes and such other objects are made to interact with cells, bacteria, viruses, etc. The interaction takes place within the cell in most cases and confocal microscopy is used to monitor the processes. For this purpose, a fluorescent tag is often attached to the nanosystem or the nanosystem itself is fluorescent as in the case of a semiconductor quantum dot. A typical example is shown in Fig. 2.22 (Plate 2) (Ref. 12).

2.4.2 Scanning Nearfield Optical Microscopy

The finite resolution of conventional optical microscopy shows that the limit of resolution is approximately $\lambda/2$, where λ is the wavelength of light used for illumination. In his three papers presented during the

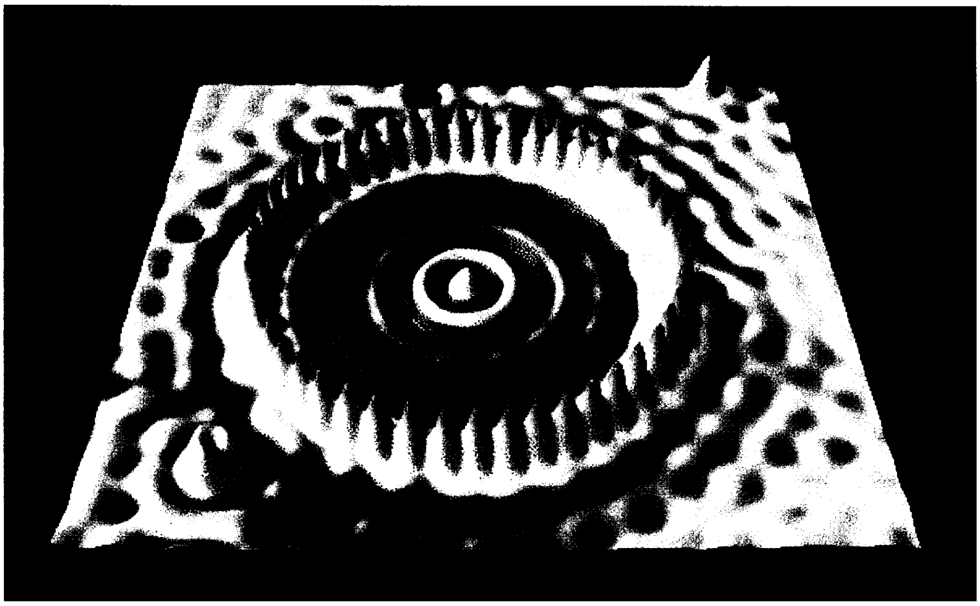

Fig. 2.17: *Quantum corral made of 48 Fe atoms on a Cu(111) surface. Color image taken from the website, http://www.almaden.ibm.com/vis/stm/stm.html. Original image was published in Crommie, et al., 1993 (Ref. 7). Reprinted with Permission from Ref. 7. Copyright (1993) AAAS.*

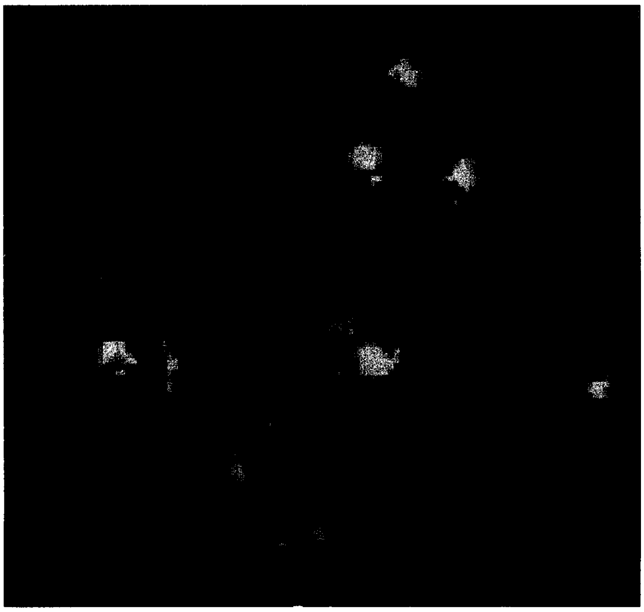

Fig. 2.22: *Confocal fluorescence image of human promyelocytic leukemia (HL 60) cells after incubation with fluorescein isothiocyanate labeled single wall carbon nanotube solution for 1 h. The image shows that nanotubes have been delivered into the cells. Reprinted with permission from Nadine Wong Shi Kam, et al. Copyright (2004) American Chemical Society.*

Plate 3

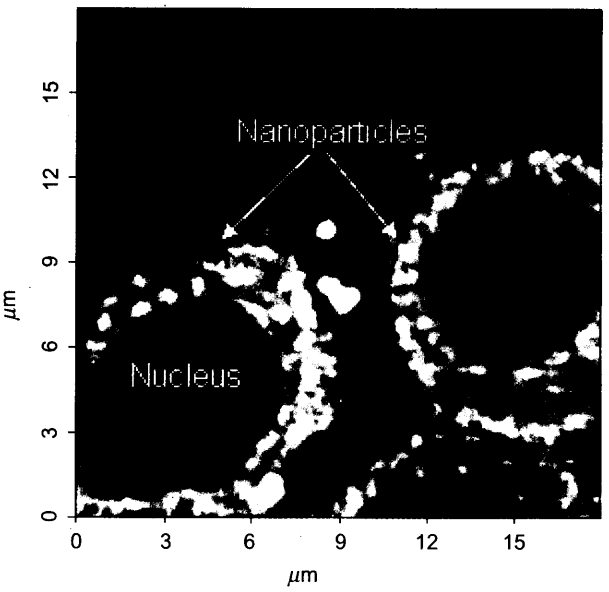

Fig. 2.24: *SNOM image of SiHa cells incubated with gold ions showing the formation of nanoparticles in the cytoplasm (From the author's work).*

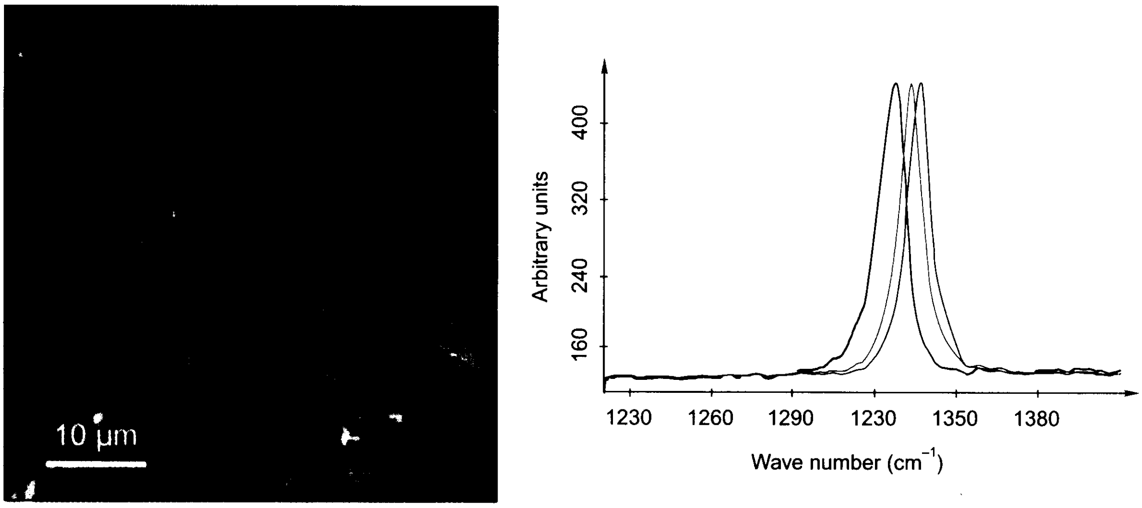

Fig. 2.31: *Raman micrograph of a CVD grown diamond film. The spectra from various regions are shown on the right. Spectra of different colours are used to construct the images of the same colours. Data and image are with the courtesy of www.witec.de.*

period 1928–32, E.H. Synge (Ref. 13) has shown that this limit can be overcome if the illumination volume is reduced to a dimension that is smaller than the wavelength of light. The fundamental aspect is that the nearfield light intensity decreases rapidly when the aperture dimension is small. This was realized experimentally in 1983 and 1984 by two independent groups soon after the discovery of STM. In this method, the light source dimension is reduced by using one of the several tools discussed below. The probe is a tip which interacts with the sample at a close distance ($d \ll \lambda$). The sample–light interaction is detected by the photodetector placed at a distance away from the sample. The distance between the sample and the tip is kept very small, by the use of a feedback mechanism which is typically based on the modulation of the quartz tuning fork. The sample or the tip is scanned so as to construct an image of the sample. This process is illustrated schematically in Fig. 2.23.

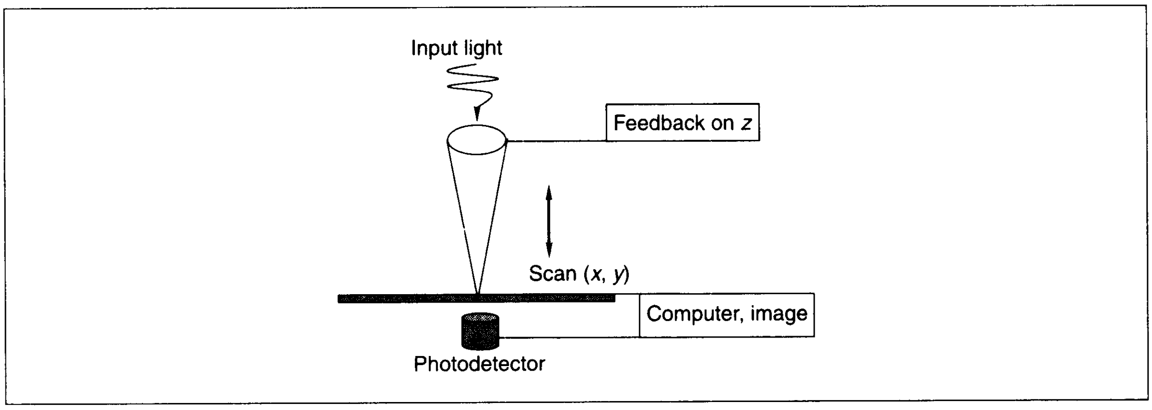

Fig. 2.23: *Schematic of a scanning nearfield optical microscope.*

There are numerous ways in which probes suitable for SNOM are made. One approach is to make probes from fibres, with one end tapered. The outer surface of the fibre is coated with a metal film and the very end of the fibre is exposed. This allows the light to pass through the tip. The standard approach to make a tapered fibre is the pulling technique in which a fibre is held in a stretched position and the middle of the stretched region is melted by a CO_2 laser or a heating filament. This allows both the ends to get stretched, which creates tapered ends. The other approach is to acid-etch the glass to produce a sharp tip. The fibre is then coated with a metal film such as aluminium or gold and the coating at the tip is removed. There are several approaches for making such an opening. The more common approach is the shadowed evaporation method. Here the metal is evaporated at a titled direction in comparison to the probe axis. This facilitates evaporation of the metal all over, except at the tip. A uniform coating on all sides is achieved by rotation. This method makes it possible to batch process tips, but the uniformity of the tips is a problem, which depends upon the angle of evaporation, rotation, etc. The other methods used are electro-erosion and ion beam milling. Tips with physical holes are also possible. In this approach, tips are micro-machined in the same way as AFM tips. Holes are then made on tips by reactive ion etching or electron beam lithography. With this technique, uniform 50 nm diameter holes have been made on Si_3N_4 cantilevers.

There are several ways in which SNOM measurements are done. Illuminating the object at farfield and collecting light at nearfield, nearfield illumination and farfield collection, and illumination and collection at nearfield are the common approaches. The other approach is by illuminating the object with evanescent waves and collecting the light with a nearfield probe. In this approach, the sample is transparent and total internal reflection of the light occurs. The evanescent waves penetrate a few hundred nanometers above the interface and they propagate into the aperture when it is brought close to the surface. This is sometimes referred to as scanning tunneling optical microscopy (STOM) or photon scanning tunneling microscopy (PSTM). While all the above methods use tips with an aperture, apertureless tips are also employed which utilize the interaction between the tip and the sample to enhance or scatter the nearfield signal. This depends on the tip–sample interaction. The sample is illuminated at farfield and the collection is also done at farfield.

The most important application of SNOM is in the study of single molecules. Here the signal, usually fluorescence, of a single molecule is detected. The dynamics of the molecules, the local environment of the molecule, the polarization dependence of emission and thereby the orientation of the dipole moment of the molecule, photobleaching, etc. have been investigated.

The lateral resolution obtained by the technique is given approximately by the diameter of the aperture. There are practical limitations to the aperture diameter. Penetration of light to the metal coating of the tip and therefore the thickness of the coating determines the illumination volume. The amount of light that can be transmitted at farfield is reduced drastically at very small aperture sizes. Increasing the light output by the sample using the field enhancement of fluorescence, for example, is a way in which one can increase the signal to noise. Nanoparticles-attached probes can be used to enhance local fluorescence intensity. Among other approaches, fluorescence resonance energy transfer (FRET) is a promising method in which the excitation energy of a probe is non-radiatively transferred to an acceptor at a very short distance. The energy transfer efficiency decreases rapidly with distance and also requires an overlap of the spectra of the molecules concerned. If one of the molecules involved in FRET is attached to the probe and the other is in the sample, probing molecular distances becomes feasible. Currently, lateral resolution of the order of 15 nm has been reported.

Light can be used for vibrational excitations as well. Of all the techniques, Raman microscopy has been used well with SNOM. However, the main problem in this is the poor Raman intensity that one gets for normal molecules and materials. The enhancement of Raman by attaching molecules on nanoparticles of noble metals or rough surfaces, called the surface enhanced Raman effect, has been used for the detection of Raman signals from single molecules.

A SNOM image of human cells (SiHa) is shown in Fig. 2.24 (Plate 3) (Ref. 14). This image was taken in the author's laboratory after the cells were incubated with Au^{3+} ions for 96 hours. The cells were removed and were embedded in a polymer matrix. Thin slices of 70 nm thickness of the processed material were taken with an ultramicrotome. The image shows the growth of gold nanoparticles in the cytoplasm of the cells. There are small nanoparticles in the nucleus of the cells too (as shown by TEM), but these are not revealed here as the resolution is poor.

2.5 Other Kinds of Microscopies

2.5.1 Secondary Ion Mass Spectrometry (SIMS)

Ion-based tools are important in nanotechnology. Two of the common tools are the focused ion beam-based lithography and secondary ion mass spectrometry (SIMS). Ion lithography can make structures in the sub 10 nm regime today. In the spatially resolved mode, SIMS can help obtain chemically specific, isotopically resolved elemental information, at a spatial resolution of 50 nm, which is impossible in the case of any other technique. As ion ejection is extremely surface-sensitive and surface damage can be reduced, nanometer thin films grown on surfaces can be analyzed with isotope specificity. This analysis can be done at trace levels and also quantitatively. These attributes make SIMS imaging extremely important.

In SIMS, one is concerned with the mass spectrometry of ionized particles resulting from the impact of primary particles on a surface. The surface can be liquid or solid and the primary particles may be electrons, ions, neutrals or photons. The secondary particles emitted from a surface are electrons, neutral or ionic atoms or molecules, and neutral or ionic clusters. In SIMS, one is concerned only with the ions. The neutrals ejected are post-ionized and subjected to mass analysis in some cases (sputtered neutral mass spectrometry, SNMS). The process of decoupling emission and ionization allows for quantitative elemental analysis. Most of the current applications are in dynamic SNMS and can be done by using lasers (see below for an explanation of the term "dynamic").

Secondary particle emission is referred to as 'sputtering'. Most of the particles emitted will be neutrals but a few ions are also emitted. Mass analysis of these ions is carried out in one of several ways, such as time-of-flight, quadrupole and magnetic sector-based methods.

SIMS can be dated back to 1910 when Sir J.J. Thompson observed the emission of positive ions from the surface of a discharge tube upon its impact with primary ions. In the present-day instruments, the principal components are: ion gun which gives ions or atoms of 0.5–50 keV, ion optics to transfer the ions to a mass spectrometer, followed by the detector. The mass spectrometer can be of the magnetic, quadrupole or time-of-flight type. A schematic of the instrument is shown in Fig. 2.25.

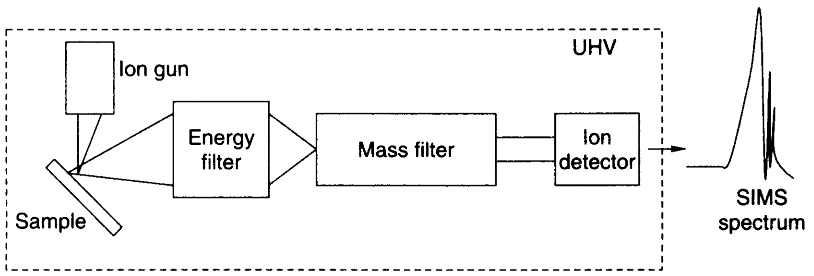

Fig. 2.25: *Schematic diagram of the main components of the SIMS experiment.*

In SIMS imaging, the mass spectral intensities collected from a surface are used to construct images. The spatial resolution of the method depends on the dimension of the sampled area. Thus it is necessary to have either a highly focused ion beam or a highly focused collection of ions. SIMS imaging is generally done in two ways. A focused ion beam is rastered across the sample and the spectrum at each point is collected. This method is called the 'microprobe mode' and its lateral resolution is of the order of sub-micron levels. The other mode is the microscope mode or the direct mode. Here the ions are collected from specific points on the sample simultaneously by electron lenses and are detected on a position-sensitive detector. The primary ion beam is not rastered.

The ion beams commonly used are Cs^+, O_2^+ or O^- or Ga^+. Although highly pointed beams of Ga^+ are possible, the secondary ion emission yield is small and therefore the first two are commonly used today. While Cs^+ enhances the negative ions, O_2^+ and O^- enhance the positive ions.

SIMS is operated in two modes. The first is the dynamic mode, wherein the primary ion flux is large and the rate at which the material is removed is high. This allows a fresh surface to get exposed to the primary beam continuously. In the case of static SIMS, only a small fraction (less than 0.1 per cent) of the surface is sampled. This results in minimal surface damage. High quality collection is necessary and therefore, the analyzer used in static SIMS is usually related to time-of-flight (TOF) based methods. As a result, static SIMS is also called TOF SIMS. In the dynamic SIMS, quadrupole and magnetic sector analyzers are used.

With the current innovations in instrumentation, imaging SIMS can acquire a lateral resolution of 50 nm. Its application areas include metallurgy, heterogeneous catalysis, biology, etc. Selective accumulation of ions of catalysts, incorporation of specific molecules in cell structures, and the separation of ions at grain boundaries, etc. are among the interesting problems that one can study. With sub-100 nm resolution, many of the cell organelles are accessible for high quality chemical imaging.

In the case of an ion or atom bombardment at a surface, the energy of the primary projectile is transferred through a billiard ball type process. This is followed by a collision cascade between the target atoms. Some of these collisions return to the surface, resulting in the emission of atoms and clusters, some of which are ionized in the course of ejection. The major concern in SIMS quantification is that the ionization coincides with sputtering. This means that calibration is a very important aspect in quantification. Particle bombardment changes the surface continually and the doses of bombardment have to be kept low to achieve meaningful surface analysis.

2.5.2 Other Mass Spectrometric Techniques of Interest to Nanoscience

Another method of carrying out SIMS is to use the fission fragments of ^{252}Cf to cause sputtering (plasma desorption mass spectrometry, PDMS). These fragments have MeV energies and when they collide at the rear of a thin foil coated with the analyte, molecular ions of high masses can get ejected. High-energy ions of $^{127}I^+$ from a tandem accelerator have also been used to achieve the same objective. High energy neutral atoms are also used for sputtering. This form of mass spectrometry, referred to as fast atom bombardment (FAB) mass spectrometry, is generally practised for organic analytes, with appropriate matrices. This results in soft ionization of the analyte species. 'Soft' implies ionization with lower internal energy for the ion formed, leading to lower fragmentation. Soft methods are especially important for the analyses of clusters as they are bound by lower energy and it is easy to fragment them during ejection to the gas phase. Today, the analysis of nanoparticles by mass spectrometry is becoming popular and the use of soft ionization methods is extremely important for achieving this goal. Laser desorption is another soft method used for desorption ionization. This is done by a technique called matrix-assisted laser desorption ionization mass spectrometry (MALDI MS), in which a low power ultraviolet laser (generally a 337 nm N_2 laser) is used to desorb the analyte. The analyte is mixed with a matrix so that the analyte concentration is small (typically in a 1:10 ratio). The mass analysis is generally done by the time-of-flight method as the laser is pulsed to help give a start time for data collection and the ions are collected at a high efficiency. An additional advantage of time-of-flight analysis is that there is no mass limit for the analysis in principle and the technique is well-suited for large biomolecules. The other soft ionization technique used is electrospray ionization mass spectrometry (ESI MS) wherein ions are produced from a solution, which is sprayed to form fine droplets in a high electric field. The solution sent through a fine needle is electrosprayed and the ions thus produced are generally multiply charged. This facilitates an analysis of large molecules in low mass range machines as their m/z value is small. Both these techniques are highly sensitive and femtomole analysis is possible with high resolution.

2.5.3 Focused Ion Beam (FIB)

The focused ion beam technique utilizes a liquid metal ion source and the interaction of high energy ion with the sample is used to investigate or modify the sample. Elastic and inelastic collisions take place when the ion beam strikes the sample. Elastic collisions lead to the sputtering of atoms and inelastic collisions yield secondary electrons and X-rays. Ions are also ejected. The ions and electrons ejected can be used for imaging the surface. The ion beam itself can be used for milling applications. In the presence of organometallic species, the ion beam can result in the deposition of materials and can be used for material repair applications. Ion beam milling can be used for sample preparation, especially for TEM.

Ions are particles with a higher momentum in comparison to the electrons used for a given acceleration energy, though they travel at a lower velocity. This leads to increased sputtering. The ion penetration depth is much smaller than that of electrons.

In SEM and FIB, the particles to be examined are scanned on the surface. The secondary particles (ions and electrons) are used for imaging in FIB. As the ions travel at much lower velocities, their Lorentz force is lower. (Lorentz force is the force exerted on a charged particle in an electromagnetic field. The particle will experience a force due to electric field qE, and due to the magnetic field, $qv \times B$. When combined, they give the Lorentz force: $F = q(E + v \times B)$, where E is the electric field, B is the magnetic field, q is the charge of the particle, v is its instantaneous velocity, and × is the cross-product.)

In addition to imaging, FIB is used for ion milling. Selective sputtering can be achieved by a method known as gas-assisted etching (GAE) in which one of the halogen gases is introduced to the work surface thus forming a volatile species. The decomposition of an already deposited organometallic molecule on the surface can lead to the deposition of certain atoms, such as Pt getting deposited from a Pt precursor molecule in the presence of the ion. The gas phase deposition process can be used to nucleate certain growth at the surface and the subsequent growth can be achieved by chemical vapor deposition (CVD). FIB can also be used for implantation.

In addition to single ion beam, an ion beam and an electron beam combination may be used, which will combine the capabilities of FIB and SEM. This can help achieve lithography, imaging and characterization together. Such an instrument has several applications in nanotechnology.

2.5.4 Photoelectron Spectroscopy

Photoelectron spectroscopy (PE) is concerned with a broad range of analytical techniques, all of which are based on Einstein's photoelectric equation, $h\nu = \mathrm{KE} + \phi$, where $h\nu$ refers to the photon energy, ϕ refers to the work function and KE refers to the kinetic energy of the ejected electron. Depending on the type of photon used for photoemission, there are several kinds of photoelectron spectroscopic techniques. The principal PE techniques are X-ray photoelectron spectroscopy (XPS), which uses X-rays, and ultraviolet photoelectron spectroscopy (UPS) which uses soft X-rays and ultraviolet radiation for photoelectron emission. XPS is generally used for the analysis of solids and surfaces whereas UPS is also used for gaseous samples.

Photoelectron spectroscopy is related to a broader class of techniques referred to as electron spectroscopy. There are principally five analytical techniques in this branch, all of which deal with the kinetic energy of electrons ejected or reflected from materials. While photoelectron spectroscopy pertains to electron emission from materials, there are also electron spectroscopic techniques dealing with inelastically scattered electrons called electron energy loss spectroscopy (EELS). Kinetic energy analysis of Aüger electrons constitutes another electron spectroscopic technique, namely Aüger electron spectroscopy (AES). The last technique is called Bresstrahlung isochromat spectroscopy (BIS). While XPS, UPS and AES are used to investigate occupied energy states, BIS is used to study unoccupied states. EELS is used for the investigation of excitation between the occupied and unoccupied states and also for the study of molecular vibrations, especially when the molecule is adsorbed on a surface. Modern developments in XPS can be largely attributed to the work of Kai Siegbahn and his colleagues in Uppsala, Sweden. In recognition of his contributions he was awarded part of the Nobel prize in Physics for the year 1981. His father, Manne, has also been a Nobel laureate (1924).

There are several variations in each of the spectroscopic techniques mentioned. For example, in ultraviolet photoelectron spectroscopy depending upon the kind of photon source, different spectroscopic techniques such as HeI UPS, HeII UPS, laser-induced UPS, etc. exist. Each of these techniques can be applied for different kinds of samples. The instrumentation for these techniques can be different thus giving different types of information. Single colour spectroscopy can be replaced with multi-colour spectroscopy, analyzers of one kind can be replaced with others, energy analysis of the electron can be done near the threshold of ionization and wavelength can be varied over a window thus giving rise to a range of experimental techniques. Conventional photoelectron spectroscopy on stable gases or solids can be replaced with that of liquids, high temperature molecules, thin films, adsorbates, single crystals, etc., thereby offering wider sample coverage.

By studying the electron energy of a series of metals as a function of photon energy, Hertz proved the Einstein relation and determined the values of '*h*'. The early photoelectron spectrometers were made in the 1950s. In today's experiment as shown in Fig. 2.26, we have a photon source, which produces monochromatic radiation and is falling on a sample, which can be a solid, gas or liquid. The photoelectrons emitted are analyzed for their kinetic energies by an electron energy analyzer and are detected. The photoelectron spectrum is a plot of the intensity of the photoelectrons as a function of electron kinetic energy. The electron kinetic energy can be directly related to the ionization potential or the binding energy (in the case of a solid) by the expression, $E_{\text{kinetic energy}} = h\nu - \phi - E_\nu$, where ϕ is the work function as mentioned earlier, E_ν is the new quantity, which is the binding energy of the photoelectron. Binding energy refers to the energy of the level from which photoemission occurs, referenced to the Fermi energy, E_F, which is taken as zero in the case of solids. In a general discussion of photoelectron spectroscopy, the spectrometer and the sample are assumed to be in equilibrium so that their Fermi levels overlap. The quantity ϕ is the energy which is the difference between the Fermi energy and the vacuum level. The spectrometer may be used to study various aspects of photoemission such as the emission angle, spin of photoelectron, etc. In the simplest instrument, only the kinetic energy of the electron is investigated.

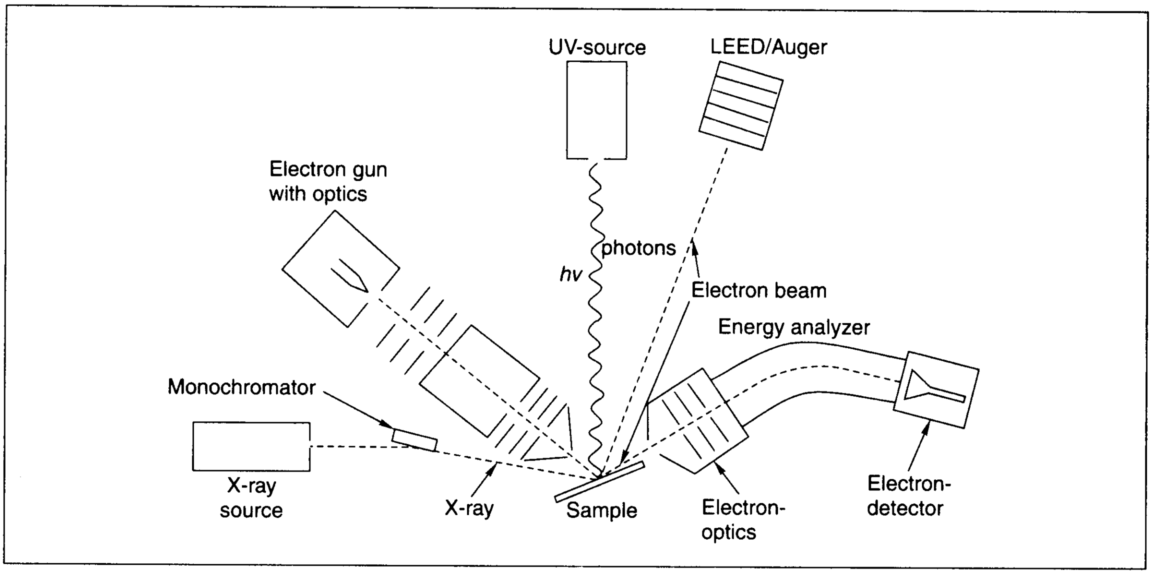

Fig. 2.26: *Schematic of a modern PES instrument. Several techniques are available in one chamber. A surface science apparatus of this kind has multiple techniques.*

In photoelectron spectroscopy, the electron kinetic energy that one normally encounters is of the order of 10–1000 electron volts. For electrons of this energy, the distance travelled before an inelastic encounter occurs is of the order of 20–30 Å. This distance corresponds to about 10 atomic layers of the material, in most cases. Therefore, while analyzing kinetic energy of electrons, we observe that the electrons of maximum intensity which do not suffer energy loss due to inelastic collisions, are principally coming from the very top of the surface and therefore, the technique is extremely surface-sensitive. Thus photoelectron spectroscopy is inherently sensitive to nanometer thin samples. However, the irradiation area is generally much larger, of the order of several mm^2 in typical measurements. This can be reduced to facilitate microscopy. The distance just mentioned (the distance in which inelastic collisions do not occur) is called the inelastic mean free path and this quantity is very difficult to measure. In experimental situations, what one normally measures is the attenuation length wherein both elastic and inelastic contributions are included. This has been determined for a large number of materials and the universal attenuation length is shown in Fig. 2.7.

For the KEs normally encountered in photoelectron spectroscopy, the attenuation length is within 20 Å for most materials. Therefore, it can be seen that if a given surface is contaminated to a few tens of Å, it is difficult to obtain a photoemission signal from the underlying material. It may be noted that in poor vacuum conditions, such as 10^{-6} torr, several tens of overlayers of contaminants can be produced in just a few minutes of exposure of a clean surface into the system. Thus, in order to be surface-sensitive, it is necessary for the surface to be sufficiently clean and devoid of overlayers. Because of its extreme surface sensitivity, photoemission spectroscopy is referred to as a surface spectroscopy. Therefore, if one is interested in the surfaces of materials, photoelectron spectroscopy is done in ultra high vacuum (vacuum better than 10^{-9} torr) where it takes about a few tens of minutes to form a complete overlayer on the surface.

Photoelectron spectroscopy pertains to electronic structure. The ionization potential that one measures corresponds to the difference between the initial ground state from which photoelectron emission occurs and the final state produced upon photoemission. To a first approximation, one can assume that the only difference between the two is that there is one electron less in the latter. This gives the most commonly used approximation, called the Koopmans' approximation, stating that $IP(k) = -\varepsilon(k)$, where $\varepsilon(k)$ is the orbital energy of the *k*th orbital. This assumption disregards the orbital relaxation effects, correlation effects and relativity effects. Thus the observed ionization potential can be calculated if the other effects are also included in the calculation such that, $IP(k) = -\varepsilon(k) - \delta\varepsilon_{\text{relaxation}} + \delta\varepsilon_{\text{correlation}} + \delta\varepsilon_{\text{relativistic}}$.

Depending upon the kind of photon used for photoemission, the levels accessed are different. Generally, the photons used are He I, He II, Al K_α, Mg K_α, Na K_α, Si K_α, etc. The He I (21.22 eV) photon corresponds to the de-excitation of the $^1P_0$ to $^1S_0$ level of He. The same is the case with He II, which corresponds to the corresponding transition of He^+ (40.8 eV). The Al $K_{\alpha\,1,2}$ corresponds to the de-excitation of $2p$ to 1s (1486.6 eV). The same is the case with Mg $K_{\alpha\,1,2}$ (1253.6 eV). These X-ray sources do not penetrate matter too deep and are called soft X-rays. (Note: The $K_{\alpha\,1,2}$ symbolism is explained in the section on X-ray diffraction.)

Most of the valence electrons are involved in bonding and it is possible to access these valence levels by using ultraviolet photons. The core levels, which are not participating in bonding, occur in the range of a few tens to 100 electron volts and can be accessed by soft X-rays. The deeper core levels of heavy elements can be accessed by hard X-rays. In photoelectron spectroscopy, one is generally concerned with energy levels of the order of 1000 eV and below.

The photoelectron spectrum is characterized by specific ionization energy and also by a width. The width has contributions from the inherent width of the state formed, the line width of the photon source used and the specific resolution of the analyzer. If all these are favourable, it is possible to measure the fine structures such as vibrational and rotational features accompanying photoionization in the case of molecules. In the case of materials and surfaces, vibrational features and other fine structures such as multiplet splitting and plasmon losses can also be measured.

Let us look at the spectrum of gaseous nitrogen as an example (Fig. 2.27). The spectrum corresponds to three different electronic states of ionized nitrogen. The potential energy curves of these ionic states are shown here with vibrational levels in them. Each band shows vibrational excitations. In fact the photoelectron spectrum is a reflection of the potential energy curves of the system. Using 21.22 eV photon, it is possible to access only these three levels. If we used sufficiently energetic photons, it would have been possible to look at other deeper levels. The photoelectron spectrum also gives an idea about the kind of energy levels involved in the ionization process. These levels actually correspond to orbitals, which participate in bonding. Ionization from these levels can give us information about the kind of bonding possible in the system. In this particular case, the first excitation corresponds to the removal of electron from a non-bonding orbital. The second corresponds to the removal of an electron from a bonding orbital. The third corresponds to the removal of an electron from a weakly anti-bonding orbital. Now it is quite clear why vibrational spacing of the first ionic state is quite similar to that of the ground state. There is no change in the bonding characteristics when an electron is removed from this level. For the second one, the vibrational spacing is smaller than that of the ground state. For the third one, the vibrational spacing is larger than that of the ground state. If an electron is removed from a non-bonding orbital, obviously the bonding characteristics

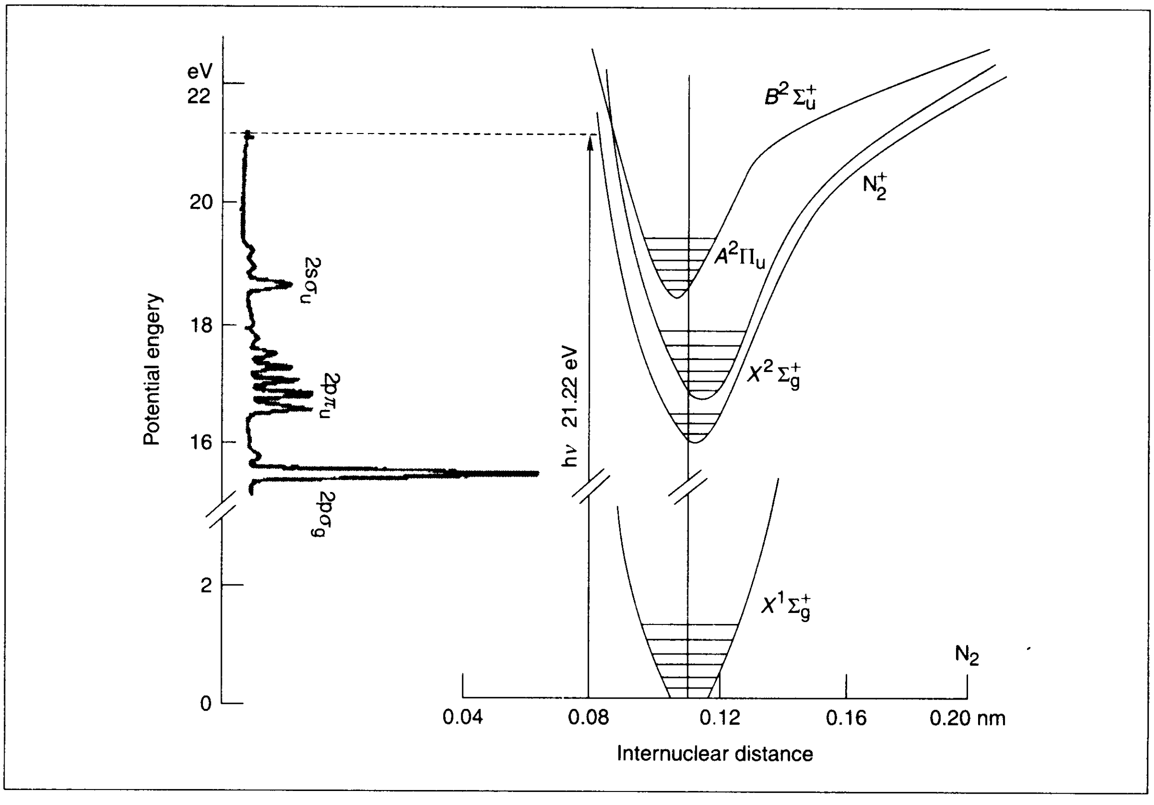

Fig. 2.27: *Photoelectron spectrum of nitrogen molecule showing that it is a reflection of the potential energy curves.*

of the molecule are not disturbed.Therefore, the internuclear distance remains unchanged and vibrational separation is largely the same. If one removes an electron from a bonding orbital, the state that is created has less bonding character, the internuclear distance can increase and therefore, the vibrational quantum may be reduced. If one removes an electron from an anti-bonding orbital, the state that is created has more bonding character and therefore the vibrational quantum is larger. It is also reflected in the equilibrium internuclear distance, which is unaffected in the first state, is shifted to the right in the second case, and is shifted to the left in the third case.Thus the photoelectron spectrum gives us a qualitative idea of the kind of bonding. In addition, the photoelectron spectrum is a mirror image of the electronic states. It is possible to reconstruct the photoelectron spectrum if one knows the states involved. It is also possible to reconstruct the states if we know the photoelectron spectrum. However, it has to be remembered that photoelectron spectroscopy is concerned with electronic transitions and therefore, the Franck-Condon rule is valid here. Thus the spectrum probes only the region very close to the equilibrium internuclear distance.The potential energy surfaces span a larger area and photoelectron spectra give very little information on the regions away from the minimum distance.This is because the molecule is always close to the minimum distance and the excitation is around it.

The earlier discussion was about ultraviolet photoelectron spectroscopy. In XPS, one is concerned about the core electrons.The important thing is that the core electron binding energies of atoms are very specific to them. In fact, the core electron binding energy of an atom can distinguish what that atom is. Due to this reason, the elemental characterization of a material is possible by photoelectron spectroscopy. In Fig. 2.28, we show the 1s photoelectron peak of the first row atoms.

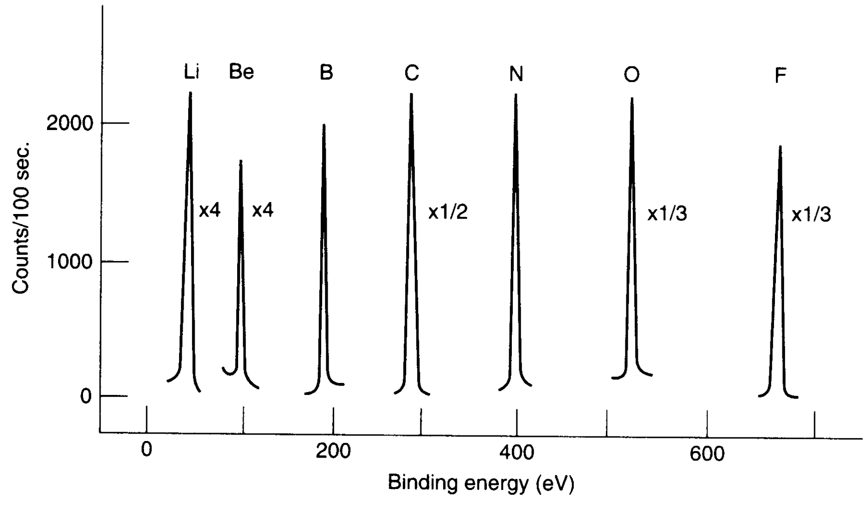

Fig. 2.28: *1s photoelectron feature of the first row atoms.*

From lithium to fluorine, it is seen that the 1s binding energy increases systematically. Besides, not only does the binding energy increase, but the intensity is also different. As can be seen, fluorine 1s is more intense than nitrogen 1s, and even if there is less amount of fluorine, it is possible to see it in the photoelectron spectrum. Not only does each level from a given atom have a specific energy but the level can also have different energies in different chemical situations. As in NMR spectroscopy, there are chemical shifts in X-ray photoelectron spectroscopy, which give us information about the kind of chemical environment. The photoelectron features of the core levels give quantitative information on the amount of that element present in the sample. Therefore, by using appropriate standards it is possible to obtain quantitative elemental information.

The photoelectrons emanating from the sample have the following three principal characteristics:

1. *The number distribution with kinetic energy*: A measurement of the number of photoelectrons with kinetic energy gives the energy distribution curve, which is normally referred to as the photoelectron spectrum. In normal photoelectron spectroscopy, the electron emission is performed at a fixed angle.
2. *The distribution of electron intensity as a function of the angle*: This measurement involves the study of intensity distribution of photoelectrons as a function of the electron take-off angle or photon propagation direction or with respect to both these parameters.
3. *The spin polarization or spin distribution of the photoelectron intensity*: This includes the preferential polarization of the electrons of the sample by an external magnetic field and studying the spin distribution of the ejected electron intensity. These measurements have not been done to a large extent, till recently.

In the photoelectron spectrum of solids, additional complications can result from the various inelastic processes that occur in the sample as the photoelectron leaves the material. This leads to a large background which may be overlapped with distinct peaks. These features are also informative and are often useful in providing a more detailed understanding of the electronic structure of the material under study.

X-ray photoelectron spectrum is normally measured with non-monochromatic X-ray sources; the principal limitation is the natural line width of the $K_{\alpha\,1,2}$ radiations. The width of this radiation is about 0.7 eV for Mg $K_{\alpha\,1,2}$ and about 0.8 eV for Al $K_{\alpha\,1,2}$. If one goes up in the periodic table, the Na $K_{\alpha\,1,2}$ lines has a width of about 0.4 eV. It is also possible to use neon, which has a natural line width of 0.2–0.3 eV and the K_α line occurs at 848.6 eV. The principal reason for the reduction in line width is the reduction in the $2p_{3/2}$–$2p_{1/2}$ spin orbit splitting and the increase in the lifetime of the 1s hole. However, neon K_α radiation is not generally used in X-ray photoelectron spectroscopy. In special cases, it is possible to use the $K_{\alpha\,1,2}$ radiation of fluorine in highly ionic compounds and certain studies have been performed with this radiation.

It is possible to monochromatize the Al $K\alpha$ or Mg $K\alpha$ radiations, thereby reducing the half width considerably. It is possible to achieve a photoelectron peak as narrow as 0.3 or 0.4 eV by using monochromatized Al $K\alpha$ or Mg $K\alpha$ radiation. The consequent reduction in intensity as a result of monochromatization is overcome by the use of rotating anode X-ray sources as well as by special detection devices, which enhance sensitivity. In addition to the $K\alpha$ radiation, it is also possible to use $M\xi$ radiation due to the $4p_{3/2}$ to $3d_{5/2}$ de-excitation process of elements from yttrium to molybdenum. These X-rays have energy in the range of 100–200 eV. Although these lines have substantially higher half widths of the order of 0.8 eV, the energy range is unique and therefore many photoelectron studies have been done with these. For example, $M\xi$ radiation of yttrium corresponds to 132.3 eV (FWHM 0.5 eV), and zirconium to 151.4 eV (FWHM 0.8 eV). One of the problems is that several aspects have to be kept in mind in these anode designs. One is that the X-rays are soft and they have less ability to penetrate through matter. Therefore, thin polymeric windows have to be used. It is also necessary to use high excitation energies so that X-ray emission takes place from the interior of the material where the element has not undergone chemical changes. In contrast, if the emission takes place from the exterior of the material, there is a possibility of emission from oxide where the valence levels are broad and the natural line width of the radiation increases. It is also necessary to use continuous deposition of fresh anode material during the operation of the apparatus. Sometimes, there are a number of threshold effects when the photon energy is very close to the ionization energy. For these experiments, it is necessary to either utilize the Bremsstrahlung radiation of an X-ray spectrum or to go to synchrotron radiation wherein the wavelength can be tuned. The huge intensity of a synchrotron radiation, the polarization and the pulsed character of the light are all utilized for many of the measurements.

Ultraviolet photoelectron spectroscopy

Ultraviolet photons from gas discharge sources such as HeI (21.22 eV) and HeII (40.82 eV) have high intensity and an inherently small line width. It is also possible to carry out photoelectron spectroscopy with higher harmonics of several lasers. This facilitates spectroscopy with higher resolution, which is also achieved with other kinds of analyzers such as time-of-flight and magnetic bottle, which have a higher resolution. In general, the resolution that one can achieve in UPS is limited only by the analyzer. The best instrumental resolution, under 2 meV, has been reported with the common hemispherical analyzer (which is also used for XPS). UPS is an important tool used for understanding the changes in the electronic structure of materials when adsorption occurs. Changes in the work function and chemical properties of the material are captured very well by UPS.

The spectra from solids is normally referenced with respect to the Fermi energy. A binding energy of zero refers to the Fermi level. This kind of a reference scheme works well as the sample and the spectrometer are in electrical equilibrium when the measurement is done, that is to say that the sample is electrically connected to the spectrometer so that their Fermi surfaces overlap. It is important to note that this kind of a description is valid only in the case of a metallic sample connected to a metallic spectrometer. The energy level diagram of the sample and the spectrometer are shown in Fig. 2.29. The electron kinetic energy in the spectrometer is modified as the electron comes into the spectrometer. In the case shown in the figure, a deceleration is observed. This is because the work function of the spectrometer is higher than that of the sample. In general, the Kinetic energy in the spectrometer, $KE = h\nu - E_B(k) - \varphi_{\text{spectrometer}}$ where $h\nu$ is the energy of the excitation source, KE and $E_B(k)$ are the kinetic energy of the electron and the Fermi referenced binding energy of the kth level of the sample and $\varphi_{\text{spectrometer}}$ is the spectrometer work function. In general, the electron suffers a deceleration amounting to $\varphi_{\text{spectrometer}} - \varphi_{\text{sample}}$.

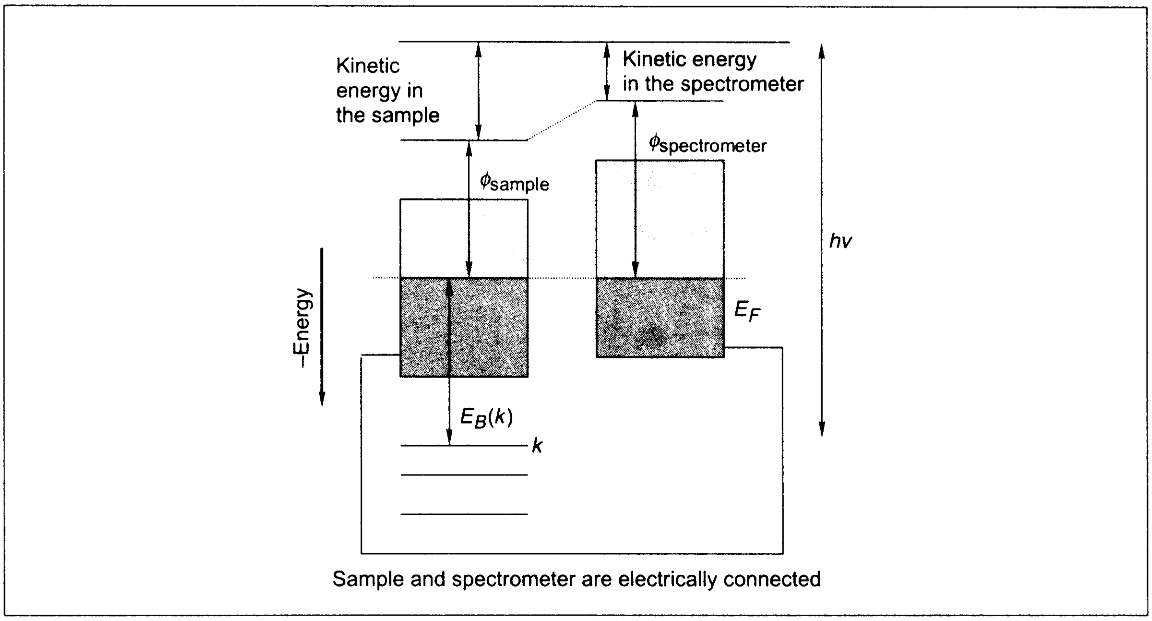

Fig. 2.29: *Schematic illustration of the sample and spectrometer energy levels.*

Aüger electron spectroscopy

The other kind of electron spectroscopy one uses is the Aüger electron spectroscopy. This refers to the energy analysis of the Aüger electron, thus named as the phenomenon was originally described by Aüger in 1925. The Aüger electron arises as a consequence of photoemission. When the core hole is produced, it is filled with a higher lying electron and the atom is now in an excited state. The excess energy is dissipated by the emission of another electron from a higher lying level. The electron kinetic energy is independent of the excitation energy of the photon used in creating the core hole, which is an important distinction from photoelectron spectroscopy where the kinetic energy of the electron increases with photon energy.

The Aüger electron ejected is labeled as KL_1L_2 in the case shown in Fig. 2.30. There can be several other Aüger electrons coming from the sample which can be labeled appropriately. All these Aüger electrons have characteristic energies, which can be used for identifying the element present in the sample or its chemical environment. The Aüger electron can be produced by other excitations also such as the electron and the ion. The electron excitation is convenient as the electron beam can be brought to a narrow size and the illumination of a microscopic area becomes possible. This allows for scanning Aüger microscopy, which analyzes the Aüger intensity of a peak as the electron beam is scanned to produce an image of the sample. The Aüger intensity decreases and X-ray fluorescence takes over at larger separations between the levels, and therefore Aüger is useful only for elements below $Z = 30$.

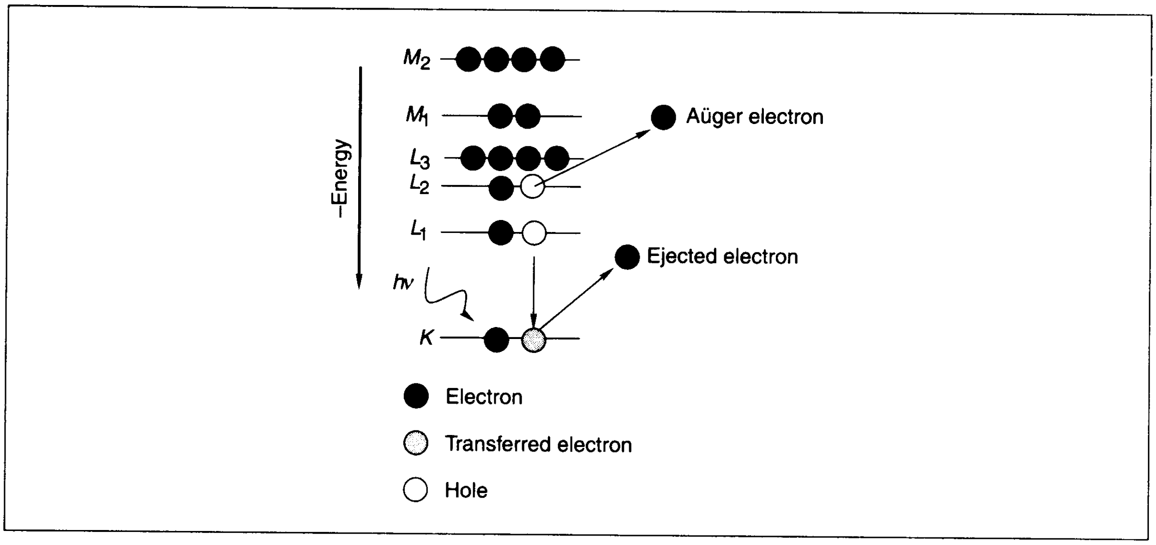

Fig. 2.30: *Schematic of the Aüger emission process.*

Surface enhancement

There are several ways to enhance the surface features in photoelectron spectroscopy. One of them is by varying the electron take-off angle (the angle between the sample plane and the electron direction). As the electron take-off angle varies, tne depth of material sampled also varies as the electron attenuation length in a sample is a constant. In order to see truly surface signals, the spectrum has to be acquired at a very low take-off angle, of the order of a few degrees. The intensity enhancement of surface features is observable with reduced photon incident angles also. However, in order to observe the features, the angles have to be close to zero. Experimental limitations come into the picture when studies are done at low take-off angles.

Improved surface sensitivity can be achieved with lower photon energy as well. As photon energy is reduced, the kinetic energy of the electron is reduced, thereby reducing the electron attenuation length. Apart from the variation in the electron take-off angle, a change in photon energy also causes a variation in the ionization cross sections. The enhancement of these cross sections makes it possible to observe the chemical signatures accompanying the surface processes.

Complications

The photoelectron spectrum is complicated with several effects which accompany photoemission. They can be grossly categorized as multiplet splitting, multielectron excitation and other many body effects. Multiplet effects occur upon electron emission from a filled level of a material containing unpaired spins. There can be more than two distinct signatures in the photoelectron spectrum of one level due to the coupling of spin and orbital angular momenta. These will give several multiplet features which may not be properly observable due to reduced intensities or reduced separation. In addition to multiplet splitting, photoelectron spectrum can be complicated due to multielectron effects such as shake-up, shake-down and shake-off. In these phenomena, photoelectron ejection accompanies electron excitation involving other orbitals. In most such cases, electronic excitation occurs by reducing the electron energy (shake-up). De-excitation processes can also take place, thus increasing the electron energy (shake-down). Excitation can also lead to complete electron removal (shake-off). Apart from these discrete excitations, there can also be many electron effects accompanying photoemission. In addition, plasmons in metals can also be excited with photoelectrons. These excitations may occur during the creation of photoelectron or upon the travel of photoelectron through the material. These are called intrinsic and extrinsic excitations, respectively. It is difficult to classify whether an event is intrinsic or extrinsic through an experiment. Several other processes of importance accompany photoemission.

Photoelectron ejection can also accompany ligand to metal charge transfer transitions. This is observable in a number of cases, with the most well-known being the ligand to metal transitions in Cu^{2+} systems.

The photoelectron spectrum can also lead to vibrational excitations due to low energy of the vibrational transitions. These features are not clearly observed in the case of many materials. However, when the vibrational energies are large (molecules of lower atomic number), vibrational excitations accompanying photoelectron ejection can be resolved.

Labeling in photoelectron spectroscopy

Photoelectron spectra are labeled as per the electronic state produced by photoionzation. In the case of molecules, the molecular electronic state formed is used to assign the peak as seen in the spectrum of nitrogen. In the case of complex molecules, the orbital from which photoionization occurs is used to label the peaks (using Koopmans' approximation, which states that the ionization potential is the negative of the orbital energy from which ionization occurs). In the case of XPS, note that each electronic state with $l > 0$ with one unpaired electron is split into two doublet states with $j = l \pm 1/2$. Two conventions are followed in naming the states. The first uses nL_j symbolism, where n is the principal quantum number and $L = s, p, d, f, \ldots$ corresponding to $l = 0, 1, 2, 3, \ldots$ This would make $2p_{1/2}$ and $2p_{3/2}$ states upon photoemission from Ne. In the alternate method, these are labeled as $L2$ and $L3$, corresponding to $l = 1$ and $j = 1/2$ and $3/2$. In this, the shell notations, $K, L, M, N, \ldots$ are used for $n = 1, 2, 3, 4, \ldots$ and subscript 1, 2, 3, 4 ... for lowest (l, j) to highest (l, j). The former is more commonly used.

Photoelectron microscopy

Photoelectrons can also be used for spatial information. There are several ways in which this can be done. In the first approach, a narrow probe beam (electrons or photons) is rastered over the sample. All the photoelectrons from the irradiated zone are collected as a function on the probe position. In the second approach, the whole sample is illuminated, but electrons from a smaller area are collected by a suitable aperture. The location of the sample from which data are collected is moved and an image is constructed. The third approach involves the illumination of the whole area and collection of the image with a position sensitive detector. The two kinds of images that are possible are spectromicroscopy and microspectroscopy. In spectromicroscopy, electrons of a specific energy range are collected. This implies energy resolved imaging used for compositional mapping. Microspectroscopy is a collection of spectral data as a function of the spatial location of the sample. The electronic structure of materials of smaller dimensions can be measured this way.

Focusing X-rays to narrow regions is difficult due to the difficulties involved in X-ray optics. It is possible to achieve photoelectron spectroscopy with 50 μm spatial resolution in this way. Imaging detectors can achieve a resolution of the order of 10 μm. However, with electrons one can get spatial resolution of the order of tens of nanometers. Scanning Aüger Microscopy (SAM) is carried out in this way. If sputtering is accompanied by SAM, three-dimensional imaging of the material composition is possible.

Another way of carrying out microscopy is through photoemission electron microscopy (PEEM). In normal photoelectron spectroscopy, the photon energy is much higher than the work function of the material. However, in the case of localized surface changes such as adsorption, only the local work function, near the area of adsorption is changed. If the sample is illuminated with a higher energy photon and the data are collected over a large area, only average effects will be seen. If, on the contrary, a low energy photon just enough to cause photoemission from the clean surface along with a higher resolution instrument is used, the region of higher work function such as an oxygen-adsorbed region will appear with a different contrast. Currently, this technique is being used to obtain sub-micron resolution in favourable cases.

2.5.5 Vibrational Spectroscopies

Vibrational spectra are characteristic of the material and are specific to the chemical bonds. Changes in the chemical characteristics of matter are reflected in the vibrational spectra. Vibrational energies are much smaller as compared to the chemical bond energies and even minute changes in the local atmosphere of a sample are reflected in the spectra. Spectroscopic information of this kind is commonly derived from infrared (IR) spectroscopy, Raman spectroscopy and electron energy loss spectroscopy (EELS). However, there are a few other less common techniques such as inelastic electron and neutron tunneling, helium scattering and sum frequency spectroscopy which may be used to obtain information on vibrations. All these are more involved techniques in terms of both money and effort. The first three techniques are more common and are used in various ways to analyse nanomaterials.

Vibrational spectroscopy is used to derive information on the vibrational excitation of molecules. Most of the time, the excitation is limited to the fundamental vibrational frequency. As the molecule is normally at the lowest vibrational level, namely $\nu = 0$, the harmonic oscillator approximation is a sufficient representation of the vibrational transitions. The transition frequency measured corresponds to the fundamental vibrational frequency, $\nu = 1/2\pi\sqrt{(k/\mu)}$, where k is the force constant of the bond and μ is the reduced mass of the system. There are several fundamental vibrational modes in the system depending on the symmetry. Several of these will be observed in the infrared and Raman spectroscopies. Altogether there are $3N - 6$ vibrational modes in a N atom containing non-linear molecule and $3N - 5$ modes in a linear molecule. The 6 and 5 correspond to the other degrees of freedom (translational + rotational) present in the molecule. The number of modes observed in Raman and IR depend on the symmetry of the system.

IR spectroscopy is possible only if the vibration changes the dipole moment of the molecule. The probability of a transition is proportional to the square of the transition dipole moment. $M_{vv'} = \int_{-\infty}^{+\infty} \psi(v)\mu\, \psi(v')d\tau$, where $\psi(v)$ and $\psi(v')$ are vibrational wavefunctions of states v and v' and μ is the dipole moment of the bond undergoing vibration. The value of the integral makes a vibration active or inactive in the IR. The symmetries of the molecule and the vibration decide this. The vibrational band intensity is a function of the intensity of the electric field of the radiation and its orientation with respect to the transition dipole. A study of the variation of infrared features as a function of the polarization of the light can be used to study the orientation of the dipole in a condensed system.

Electron energy loss spectroscopy is based on the inelastic collisions of a monochromatic beam of electrons and the study of the kinetic energy of the electrons. The energy loss of the sample corresponds to excitations in the sample. Electronic, vibrational and rotational excitations of the sample can be studied in EELS. Electronic excitations can be of the core levels or of the valence levels. While the former is referred to as inner shell EELS (ISEELS), the latter is referred to as EELS. The spectroscopy used in the study of vibrations is called high resolution electron energy loss spectroscopy (HREELS) and is generally used for the study of adsorbates. Due to experimental problems, it is not possible to observe all the excitations in one kind of spectrometer. Rotational spectra are not studied with EELS as electron energy analysis is not possible at the resolution required for rotational spectroscopy in most cases. The principal aspect of the spectrometer which limits resolution, is the electron energy analysis and the analyzer limits the instrumental performance. The analyzer performance is given in terms of the full width at half maximum (FWHM) which is generally of the order of a few meV in HREELS. A typical vibrational frequency occurs at 100 meV (806.5 cm^{-1}).

EELS involves three kinds of excitation mechanisms. The first is dipole excitation and the interaction between an electron and molecule is similar to light and matter. This leads to transitions similar to that observed in optical spectroscopy. This leads to specular scattering. The other kind of transition is impact-driven in which the electron behaves like a particle. The angular distribution is complex and non-allowed transitions can be excited in this process. The next kind is resonance excitation wherein the electron undergoes exchange with the sample. This results in isotropic scattering. Here again, the transitions which are not allowed can be excited. Thus a proper application of EELS can provide additional information which is not possible in the case of optical spectroscopy.

The infrared spectrum is measured by illuminating the sample with a polychromatic infrared light and by measuring the absorption of the sample. Two kinds of methodologies are normally used, one by a dispersive infrared spectrometer and another by using the Fourier transformation of the interferogram resulting from the interference of two light beams with different path lengths. The latter technique called FT-IR is the most common analytical method used these days. The Raman spectrum is measured by analyzing the scattered light coming from the sample. The illuminating light is generally in the visible region of the electromagnetic spectrum, which allows for focusing to a few hundreds of nanometers. If the light is focused on a sample using a SNOM aperture, it is possible to illuminate a single nano object and the Raman spectral measurement of this object becomes possible. The other illumination source used for vibrational spectroscopy, namely electrons, can be focused on the sample at smaller areas, as in the case of transmission electron microscopy. However, this beam is inherently of large energy and concomitantly of poor resolution, and therefore vibrational spectroscopy is impossible. At the same time, though poor in resolution, the features of inner shell excitation are useful in identifying the elemental constituents and nature of binding of materials at the nanometer regime. At lower excitation energies of the order of a few eV, the electron beam has a very narrow energy width, of the order of 1 meV or less, which allows the use of vibrational spectroscopy. This is normally performed on adsorbate molecules which are present on the surface at monolayer coverages. Because of this fact and also due to the fact that electrons are used, HREELS is done in ultra high vacuum. Due to the extreme surface sensitivity of the low energy electrons, the technique looks at the top monolayer only. In HREELS, one can observe low energy vibrational excitations, such as those representing the adsorbate-surface interactions. These are necessarily low energy vibrations as their force constants are small and the mass of the surface atom is large. It is not possible to see these low energy motions in infrared as far infrared spectroscopy is rather difficult at surfaces. These may be possible to observe in Raman, but regular Raman becomes difficult due to a poor scattering cross section.

Imaging materials with vibrational spectroscopies provides complete information about the sample. This is done in IR and Raman spectroscopies, and the instruments are called IR and Raman microscopes, respectively. Just as in XPS, in vibrational spectroscopy too, there is microspectroscopy and spectromicroscopy. The IR images of samples reveal the chemical details of the sample. Peak intensities, shifts, widths, etc. can be used for imaging. Figure 2.31 (Plate 3) shows a Raman image of a chemical vapor-deposited diamond. The spectrum of the sample is shown on the right side. Different regions of the sample give slightly different spectra with a distinguishable shift. These shifts correspond to the strain in the sample. The shift can be used to obtain a strain distribution in the sample. This is possible with a spatial resolution of the illumination source (of the order of $\lambda/2$). Sub-micron particles have been imaged by Raman spectroscopy using the vibrational band intensity. Using confocal techniques, it is possible to confine the scattering molecule within the interaction volume and to measure spectra from single molecules. This is possible only when the spectra can be enhanced, as in the case of surface-enhanced Raman spectroscopy.

2.5.6 Dynamic Light Scattering

Dynamic light scattering (DLS) is also called quasi-elastic light scattering (QELS) or photon correlation spectroscopy. This is one of the foremost techniques used to measure the radius of a particle in a medium. The motion of particles of micron or lower size is uncorrelated, i.e. they are random. As light scatters from such particles, there will be a shift in the phase of the scattered light which is random and as a result, when the scattered light rays from several particles are added together, constructive or destructive interference occurs. What we get is time-dependent fluctuation in the intensity of the scattered light. The scattering of light from particles undergoing Brownian motion also leads to a Doppler shift of the radiation, modifying the wavelength of the light. In a set-up, a laser light beam is sent through a sample containing particles. The sample has to be inhomogeneous in one of the several ways (such as due to the presence of particles, micelles, proteins, acoustic waves, etc.). The scattered light is received by a fast detector. If the intensity of the light is measured as a function of the scattered direction, we undertake what is called the static light scattering experiment. If the correlation of light intensity is measured as a function of time, we undertake a dynamic light scattering experiment.

The summary of the theory is that when the electric field of the light interacts with the molecules in the medium, an oscillating electric field is induced. The interaction leads to a shift in the frequency of the light and angular distribution of the scattered light, both of which are related to the size. If one assumes that the particles are in Brownian motion, one can apply the Stokes-Einstein equation and get the radii of the suspended particles; $a = k_b T/6\pi\eta D$, where k_b is be Boltzmann constant, D is the diffusion coefficient, η is the viscosity and T is the absolute temperature.

In a QELS measurement, the time-dependent fluctuations in the scattered light are measured. A quantitative measure of the fluctuation is the correlation function. A second order correlation function can be given as: $g^2(\tau) = < I(t)I(t+\tau) > / < I(t^2) >$, where $I(t)$ is the intensity at time t and $I(t+\tau)$ is the intensity at an incremental increase in time $t+\tau$. Brackets correspond to averaging over t. The correlation function can be analyzed to yield a decay rate Γ by using the equation, $g^2(\tau) = B + \beta\exp(-2\Gamma\tau)$, where B is the baseline at infinite decay and β is the amplitude at zero decay. The diffusion constant can be evaluated from $D = \Gamma/q^2$, where q is the magnitude of the scattering vector $(4\pi n_0/\lambda)\sin(\theta/2)$ where n_0 is the solvent index of refraction. Now the Stokes-Einstein equation can get the radii of the suspended particles.

In a typical experiment, only the wavelength and one scattering angle are used. In principle, the technique can distinguish the nature of particles, separated or aggregated, over a range of particle sizes. Typical measurements are done in the nanometer to one micrometer size regime.

2.6 X-Ray Diffraction

The genesis of XRD can be traced to the suggestion of Max von Laue in 1912 that a crystal can be considered as a three-dimensional diffraction grating. The suggestion was based on a Ph.D. thesis of Paul Ewald who considered a crystal as a three-dimensional array of oscillators separated at a distance. Experiments proved the suggestion of Laue. Methodologies of powder X-ray diffraction were developed independently in Germany and in the United States. Single crystal diffractometers were developed in the early 1950s. Although the method of X-ray diffraction is quantitative, in general, it is used for qualitative analysis. This form of analysis extends to all crystalline solids including ceramics, metals, insulators, organics, polymers, thin films, powers, etc. X-ray diffractometers can be used either for single crystals or for powders, with both using significantly different infrastructure. While single crystal diffractometers are used for the study of molecular structure, powder diffracrometers are used for the analysis of phases, though the latter can also be used to derive molecular information.

X-rays corresponds to electromagnetic radiation in the wavelength range of 1 Å. The wavelength range is below that of ultraviolet light and above that of gamma rays. This radiation is produced when charged particles are decelerated by metals, thus producing a continuum called Bremsstrauhlung radiation. X-rays are generally produced when electrons of several thousands of electron volts are decelerated or stopped by metals. This will produce a white radiation up to a threshold frequency corresponding to the kinetic energy of the particle. This threshold corresponds to a wavelength (in angstroms), $\lambda = 12399/V$ where V is the accelerating voltage of the electrons.

When particles such as electrons fall on matter with high energy, electrons can be ejected from various energy levels. Electron ejection from the core orbital is also accompanied by the emission of characteristic X-rays. In the case of electron from the 1s orbital an outer electron from the $2p$ or $3p$ orbital can fall down to occupy the vacant 1s orbital. This $2p \rightarrow$ 1s transitions leads to the emission of K_α radiation. A similar transition is possible from the $3p$ level resulting in K_β. The K_α is a doublet with $K_{\alpha 1}$ and $K_{\alpha 2}$ corresponding to electronic transition from the two possible spin states of the $2p$ electron ($2p_{3/2}$ and $2p_{1/2}$, respectively). In most of the diffraction experiments $K_{\alpha 1}$ and $K_{\alpha 2}$ are not separated and the statistically weighted average of the two wavelengths is taken. The wavelength of a given X-ray line depends on the atomic number.

The emission spectrum of a metal is shown in Fig. 2.32. Characteristic radiations are overlapped with the Bremsstruhlung. Various kinds of filter materials are used to avoid unwanted radiations. Monochromatization by diffraction can also be done to improve the optical purity of the radiation. In a typical X-ray tube used to generate X-rays, high energy electrons are accelerated to a target in an evacuated tube. Only a fraction of the incident electron energy is converted into X-rays. Most of it is converted to heat and efficient cooling of the anode is necessary to avoid it from melting. X-rays come out of the tube through a window made of small atomic number materials such as beryllium.

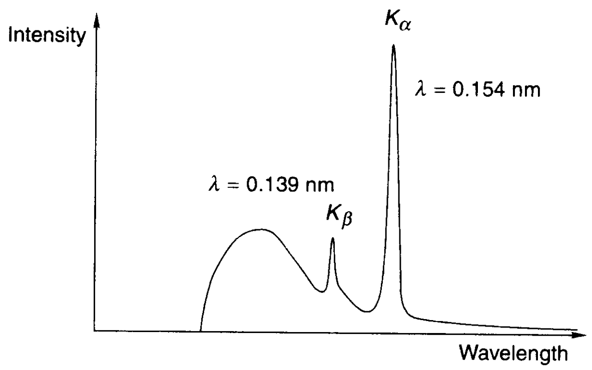

Fig. 2.32: *X-ray emission spectrum from copper. Copper K_α corresponds to 1.54 Å.*

Diffraction of light by crystals can be understood with the help of an optical grating consisting of several parallel lines drawn on a glass plate. As light is incident on the grating, each group will act as a line source and light will be radiated in all directions. Interference occurs between the waves and in a certain direction, constructive interference occurs. In Fig. 2.33, constructive interference is shown to occur in two directions, marked by lines. In the direction represented by the bottom arrow, the waves are in phase though each wave is shifted by one wavelength from the other. Between these two directions, in all the other directions interference occurs reducing the intensity. In the case of several line sources, as would be present in the case of a grating, interference occurs over several waves and no intensity can be seen between the directions shown. In the case of a grating, the condition of constructive interference is that the path length between the beams should be an integral multiple of the wavelength. This can be written as $n\lambda = d\sin\theta$, where d is the distance between the grooves and is θ the angle of observation. For the first order diffraction, $\lambda = d\sin\theta$. As the maximum value of $\sin\theta = 1$ and $\theta = 90°$, the first order diffraction will be observed at this angle. In general, the angle will be lower than 90° and for d less than λ only zero order direct beams will be observed. If d is much larger than λ, individual diffracted beams of different orders will be closed to each other and we get a diffraction continuum. In the case of visible light (4000 to 7000 Å wavelength), a grating spacing of 10,000 to 20,000 Å is used to observe diffraction.

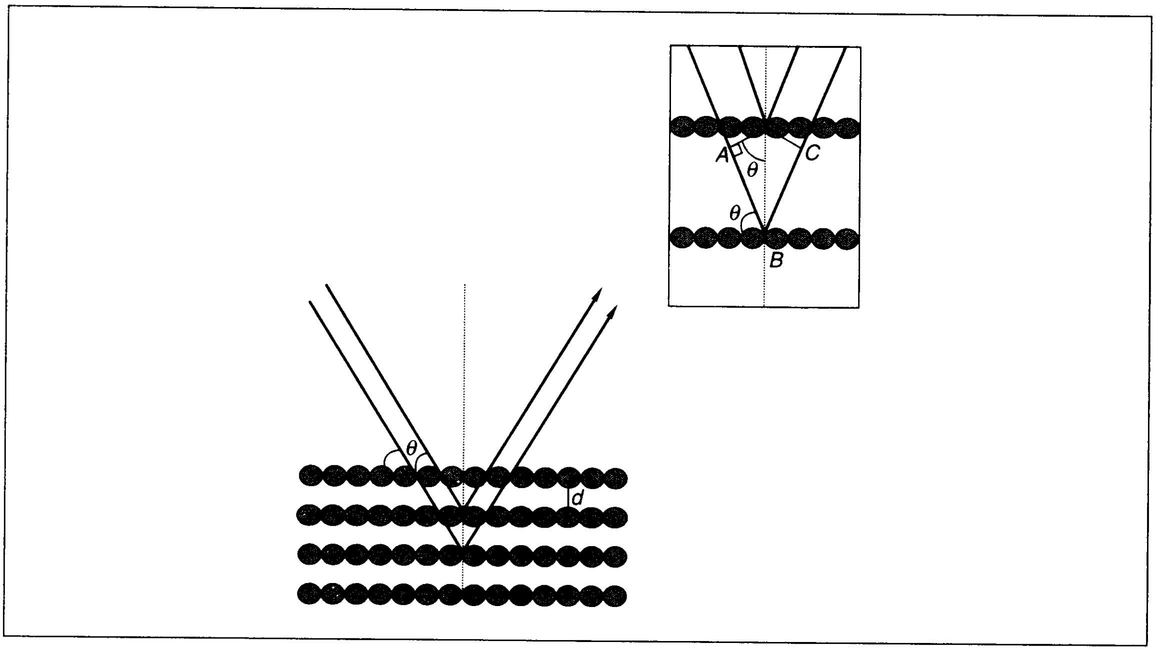

Fig. 2.33: *The conventional derivation of Bragg law. Between the directions shown, the path difference is a multiple of the wavelength and as a result, the intensity will be the maximum at the outward direction. The path length between the two lines, AB + BC = 2d sin θ (as shown in the inset).*

X-Ray Diffraction Three kinds of radiations are generally used for diffraction: X-rays, electrons and neutrons. Commonly, the characteristic X-ray used for diffraction is the copper $K\alpha$ radiation at 1.5418 Å wavelength. Two approaches are generally used for the analysis of X-ray diffraction data. These are the Laue equations and the Bragg's law. In the Laue equations, diffraction from a one-dimensional crystal may be treated in the same way as the diffraction by an optical grating. Upon projection, the grating is like an array of points similar to a crystal. The diffraction condition is again, $n\lambda = d\sin\theta$. In a crystal arrangement of atoms is periodic in all the three directions and three independent Laue equations can be written. The three equations have to be satisfied simultaneously for diffraction to occur.

In Bragg's law, a crystal is viewed as a plane containing several lattice points. The reflection of X-rays will take place from these planes with the angle of reflection being equal to the angle of incidence as shown in Fig. 2.33. The reflected beams are in phase when the path length between the beams is an integral multiple of the wavelength. The planes of light travelling after reflection will be in phase only when this condition is satisfied. This would mean that the distance, $ABC = n\lambda$ or $2d \sin\theta = n\lambda$ (shown in the inset). For all angles other than θ, destructive interference will occur leading to cancellation of the intensity. For crystals containing thousands of such planes, Bragg's law imposes severe restrictions on θ and the cancellation of intensities is usually complete. However, in cases where the number of diffracting planes is limited, the diffraction peak will broaden. In fact, this effect can be used to measure the particle size which is the basis of the Scherrer formula.

One should remember that the interaction of X-rays by atoms is a rather complex event involving electrons of the scattering centres. However, a simplistic picture of reflection is adequate to explain the observed phenomena.

The diffraction of X-rays is generally analyzed in terms of the experimental lattice of the crystal depicted in terms of the lattice vectors. There are relations between observed reflections and (*hkl*) values. The lowest *d* spacing observable is $d = \lambda/2$ since the maximum value of $\sin\theta = 1$. Although it appears that the number of lines observable is infinite, the possible number of planes is finite. The Miller indices used for calculating the *d* spacing can only have integral values. The largest *d* spacing corresponds to Miller indices such as (100), (010), etc. If the unit cell dimensions are known, the *d* spacing can be calculated by using the appropriate formula. There are relations such as $1/d^2 = h^2/a^2 + k^2/b^2 + l^2/c^2$ for orthogonal crystals ($\alpha = \beta = \gamma = 90°$). For tetragonal crystals ($a = b$), the equation is further simplified. For cubic crystals ($a = b = c$), the relation is $1/d^2 = (h^2 + k^2 + l^2)/a^2$. Several possible (*hkl*) combinations and their *d* spacings can be calculated. Depending upon the structure of the unit cell, several diffraction peaks may be absent in the diffraction patterns. Several diffractions are absent as a result of the symmetry such as non-primitive lattice type or certain elements of space symmetry. Consider the *bcc* lattice type. The (100) reflection has 0 intensity in the pattern. This is because at the Bragg angle for these planes, the body centre atoms diffract X-rays at 180° out of phase relative to the atoms in the corners. As the number of atoms in the corners is equal to those at the centre, the diffracted intensity gets completely cancelled. For a body-centred cell, all reflections for $(h + k + l)$ is odd are absent.

The X-ray diffraction experiment requires the following: a radiation, a sample and a detector for the reflected radiation. In each of these cases, there can be several variations. For example, the radiation can be of many kinds, a single monochromatic source or of variable frequency. The sample can be powder, single crystal, solid piece or a thin film. The detector can be of several kinds, ranging from a simple photographic plate to a sophisticated counter or an area detector. In a powder diffraction experiment, there are crystals arranged in all possible orientations in a finely powdered sample. The various lattice planes are also arranged in all possible orientations. For each crystal plane, there will be a number of orientations. The reflected X-rays may be collected on a photographic plate or by using a counter that is suitably connected to a recorder.

In the Debye-Scherrer method of diffraction, we use a monochromatic X-ray and a power sample with every possible set of lattice planes exposed to the radiation (Fig. 2.34). The diffracted radiation gives rise to a cone. The condition of diffraction is that the radiation is at an angle θ to the incident beam. The cone arises because there are several angular positions of the crystals. The cone is a result of several closely separated spots (inset). In the case of a finely ground sample, the spots will be replaced by a continuous line. Each (*hkl*) results in one core.The detector is moved in a circle to collect all the reflections corresponding to various (*hkl*).

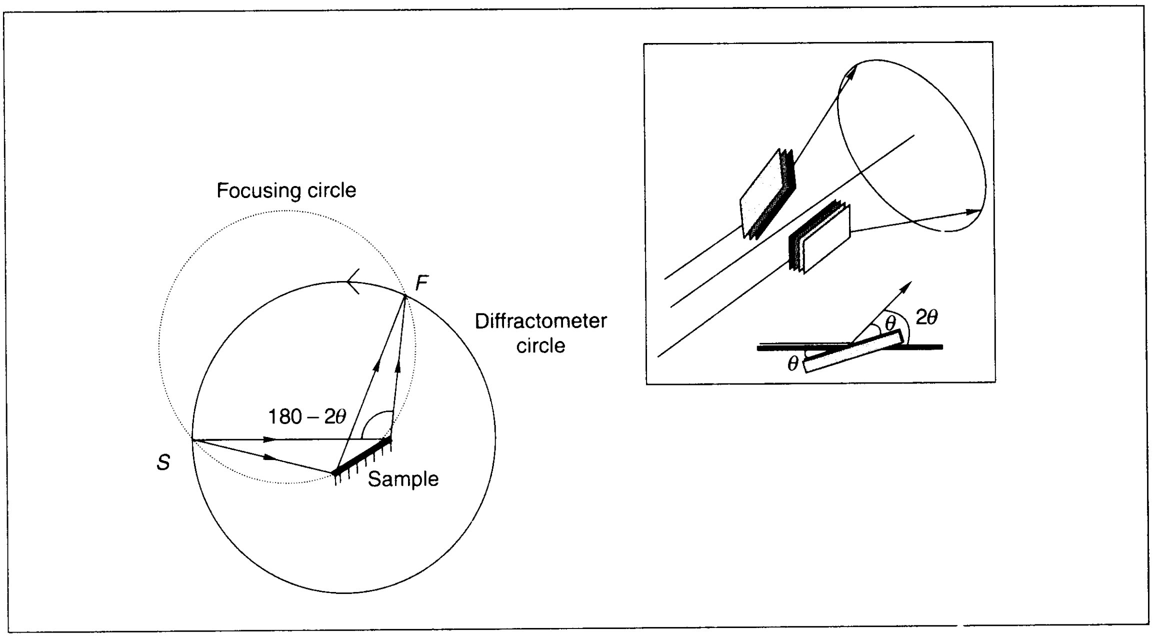

Fig. 2.34: *The Debye-Scherrer method of powder diffraction. S and F are source and detector, respectively. Two microcrystallites of different orientation with respect to the incident beam give diffracted rays that lie in a cone. The diffraction pattern is due to all the (hkl).*

In the modern diffraction method called diffractometry, a convergent beam strikes the sample and the intensity as a function of diffraction angle is measured. The position of the diffraction peak and the intensity at this point are the two factors used in the determination. Both these can be measured accurately and compared with standards in the literature. In fact, this is what one normally does in the phase identification work.

2.6.1 Intensities in X-ray Scattering

Intensities are important in X-ray analysis for determining unknown crystal structures and quantitative phase analysis. X-rays are electromagnetic waves and can interact with electrons, thus making them vibrate. The vibrating charge will emit electromagnetic radiation which is in phase (coherent) with the incident X-ray. Coherent scattering is similar to elastic collision and the wavelength of the X-ray is not changed. The intensity of the radiation scattered can be given by the Thomson equation, $I_p \alpha 1/2(1 + \cos^2 2\theta)$, where I_p is the scattered beam intensity at point p, and 2θ is the angle between the incident and the scattered beams. X-rays can also interact with matter and get inelastically scattered thus giving rise to Compton scattering. Loosely bound electrons are more involved with this and are responsible for the background in the diffraction measurements.

Scattering can be considered to occur from each electron. The total scattered intensity will be a sum of all the scattered intensities due to individual electrons. Thus the scattering factor or the form factor is proportional to the atomic number. The scattering factors of atoms of similar atomic numbers are close and therefore it becomes difficult to identify similar atoms. This becomes a problem in the single crystal diffraction of organic compounds containing C, N and O. This is also a problem in aluminosilicates due to the similarity of Si and Al. It is difficult to determine hydrogen in the presence of heavy elements. This is not a problem with neutrons as the scattering factors are not the functions of atomic numbers alone.

The structure factor or structure amplitude for each (*hkl*) can be defined and calculated from the measured intensities. This can be used to define a residual factor or R factor. The quality of the structure determination is understood in terms of the magnitude of the R factor, the lower the better. Generally it is in the range of .1 to .2. While solving the structure, one often determines the electron density maps. These maps are instructive for understanding bonding.

The most commonly used X-ray instrument is the powder diffractometer. It has a scintillation or Geiger counter. The detector spans a range of scattering angles. Generally it is a practice to mention 2θ, not θ, as the scattering angle. A 2θ range of 10 to 80 degrees is adequate for covering the most useful part of the pattern.

The *d* values can be readily calculated from the graph. The intensities are generally taken as peak heights unless an intensity analysis is performed where the peak area is taken. The peak of maximum height is taken as 100 and all the other peaks are scaled accordingly. A set of peaks and their heights is generally adequate for phase identification. In several cases, an accurate measurement of peak positions is needed. Preferred orientations exist for a number of materials and it is likely that only these peaks are manifested. In order to make all crystal planes observable (within the crystal system), it is important that the sample is finely ground. Several sample preparation methodologies are employed.

The convergent beam of X-ray is important for improved sensitivity and resolution. This is achieved by placing the source and detector at the circumference of a circle.

In focusing geometry, the configuration of the diffractometer is different. Here the source and the detector will form the circumference of a circle called the diffractometer circle and the surface of the sample must lie tangential to the focusing circle. While the detector has an angular speed of 2θ deg min^{-1}, the sample rotates in the same direction at an angular speed of θ deg min^{-1}.

2.6.2 Particle Size Effects

The normal diffraction line is of a finite width due to several factors such as the finite line width of the excitation source and the imperfections in the focusing geometry. The Bragg condition occurs when each plane in a crystal diffracts exactly one wavelength later than the previous plane. Constructive interference occurs due to this condition. When the incident ray at a larger angle, $\theta 1$ than the diffraction angle, θ strikes the crystal plane, the phase lag is greater than the wavelength, λ to become $\lambda + \delta\lambda$. As the number of planes becomes $j + 1$, the cumulative phase lag, $\sum \delta\lambda$ could increase to become λ i.e., $j\, \delta\lambda = \lambda/2$. For the ray incident at the larger angle $\theta 1$, the diffracted rays from plane 1 and plane, $j + 1$ are 180° out of phase. As a result, there is no net intensity for the diffracted ray at this angle. Now let us understand that we have several planes in the crystallite and the rays diffracted from the set of planes, 1 through j are exactly cancelled by the planes $j + 1$ through $2j$, if there are $2j$ planes present in the crystallite. What this means is that the intensity of the diffracted beam will fall to zero at a finite angle, with a peak maximum as a result of this effect. One should note that there is also a phase difference, $\lambda - \delta\lambda$ which occurs for an angle $\theta 2$, smaller than θ. The width of the diffraction peak is therefore determined by the number of planes present in the crystallite. For large crystallite, j is large, $\delta\lambda$ is small and the width is negligible. The particle size effects seen as broadening of the diffracted lines is given by the Scherrer formula, $t = 0.9\, \lambda/(B \cos\theta)$, where t is the thickness of the crystallite in (angstroms) and θ is the Bragg angle. B is the line broadening, indicating the extra peak width of the sample in comparison to the standard, derived using the Warren formula, $B^2 = B_M^2 - B_S^2$, where M and S refer to specimen and standard. B's are measured in radians at half height. The sample and standard should have peaks close to each other.

Particle sizes up to 200 nm can be measured by using the Scherrer formula. In the range of 5–50 nm, the broadening is easy to determine. At larger particle sizes, the difference between the sample and the standard is small and at small particle sizes, the peak is difficult to distinguish from the background. For smaller particle sizes, low angle peaks are used for size determination as they are less broad as compared to large angle peaks.

In passing, it may be mentioned that the powder pattern may be shifted or broadened as a result of stresses present in the material. Due to uniform compressive stress, the d spacing may reduce and the peak may shift to larger angles. If the stress is non-uniform throughout the crystallite, broadening will occur. A composite of these effects is generally observed.

2.7 Associated Techniques

In addition to the above, various analytical techniques are also used for nano measurements. Broadly, any technique used for material characterization can be applied in this area too. Several of these techniques such as zeta potential will be discussed at appropriate places in the text where a discussion on these relates to the subject matter. Such studies imply that almost every tool is adaptable for nanomaterial investigations.

Review Questions

1. Why objects in the nanoscale cannot be seen by visible light? How do we see them?
2. What are the principal differences between electron and scanning probe microscopies?
3. Why is it not possible to image nano objects with infrared or X-rays? What are the current capabilities with these techniques? What are their specific advantages?

4. What are the characteristic properties of objects in the nanoscale? Which of those properties we use to examine them?
5. Every property possessed by bulk materials is also possessed by nano objects. So, how can one study nano objects uniquely?
6. How do we study properties of single nano objects?
7. What are such properties being investigated? Describe them with an example.
8. Propose an experiment to study the strength of a single chemical bond.
9. Single molecules are governed by laws of quantum mechanics. So their position will be uncertain if we examine them. Then how is it possible to observe and manipulate them?
10. How will nanotechnology work if positioned atoms and molecules do not stay at the specific location?
11. Are there properties which we cannot measure with the techniques described?
12. Are there other techniques, other than those described here, to study nano objects? Propose a new technique or modify a technique known to you for this study.

References

1. Goldstein, J.I., C.E. Lyman, D.E. Newburry, E. Lifshin, P. Echlin, L. Sawyer, D.C. Joy and J.R. Michael, (2003), *Scanning Electron Microscopy and X-ray Microanalysis*, Kluwer Academic/Plenum Publishers, New York.
2. Thomas, G., and Goringe, M.J., (1979), *Transmission Electron Microscopy of Materials*, John Wiley and Sons, New York.
3. Treacy, M.M.J., T.W. Ebbesen and J.M. Gibson, (1996), *Nature*, **381**, p. 678.
4. Binning, G., H. Rohrer, Ch. Gerber and E. Weibel, (1982), *Phys. Rev. Lett.*, **49**, p. 57.
5. Wildoer, W.G., L.C. Venema, A.G. Rinzler, R.E. Smalley and C. Dekker, (1998), *Nature*, **391**, p. 59.
6. Eigler, D.M., and E.K. Schweizer, (1990), *Nature*, **344**, p. 524.
7. Crommie, M.F., C.P. Lutz and E. Eigler, (1993), *Science*, **262**, p. 218.
8. Manoharan, H.C., C.P. Lutz and D. Eigler, (2000), *Nature*, **403**, p. 512.
9. Stroscio A., and W.J. Keiser, *Scanning Tunneling Microscopy*, Academic Press, 1993.

SXM Techniques and Capabilities (From Ref. 9)

(a) *Scanning Tunneling Microscope*, (1981), G. Binnig, and H. Rohrer, "Atomic Resolution images of Conducting Surfaces", G. Binning, H. Rohrer, Ch. Gerber and E. Weibel, *Phys. Rev. Lett.*, **49** (1982), pp. 57–61.

(b) *Scanning Near-field Optical Microscope* (1982), D.W. Pohl, "50 nm (Lateral resolution) Optical Images", D.W. Pohl, W. Denk and M. Lanz, *Appl. Phys. Lett.*, **44** (1984), p. 651; A. Harootunian, E. Betzig, A. Lewis and M. Isaacson, *Appl. Phys. Lett.*, **49** (1986), p. 674.

(c) *Scanning Capacitance Microscope* (1984), J.R. Matey, J. Blanc, "500 nm (Lateral Resolution) Images of Capacitance Variation", J.R. Matey and J. Blanc, *J. Appl. Phys.*, **57** (1984), pp. 1437–1444.

(d) *Scanning Thermal Microscope* (1985), C.C. Williams, H.K. Wickramasinghe, "50 nm (Lateral Resolution) Thermal Images", C.C. Williams and H.K. Wickramasinghe, *Appl. Phys. Lett.*, **49** (1985), pp. 1587–1589.

(e) *Atomic Force Microscope* (1986), G. Binning, C.F. Quate, Ch. Gerber, "Atomic Resolution on Conducting/Non-conducting Surfaces", G. Binning and C.F. Quate, *Phys. Rev. Lett.*, **56** (1986), pp. 930–933.

(f) *Scanning Attractive Force Microscope* (1987), Y. Martin, C.C. Williams, H.K. Wickramasinghe, "5 nm (Lateral Resolution) Non-contact Images of Surfaces", Y. Martin, C.C. Williams, H.K. Wickramasinghe, *J. Appl. Phys.*, **61** (1987), pp. 4723–4729.

(g) *Magnetic Force Microscopy* (1987), Y. Martin, H.K. Wickramasinghe, "100 nm (Lateral Resolution) Images of Magnetic Bits/Heads", Y. Martin and H.K. Wickramasinghe, *Appl. Phys. Lett.*, **50** (1987), pp. 1455–1457.

(h) *"Frictional" Force Microscope* (1987), C.M. Mate, G.M. McClelland, S. Chiang, "Atomic-scale Images of Lateral ("Frictional") Forces", C.M. Mate, G.M. McClelland, R. Erlandsson, and S. Chiang, *Phys. Rev. Lett.*, **59** (1987), pp. 1942–1945.

(i) *Electrostatic Force Microscope* (1987), Y. Martin, D.W. Abraham, H.K. Wickramasinghe, "Detection of Charge as Small as Single Electron", Y. Martin, D.W. Abraham, and H.K. Wickramasinghe, *Appl. Phys. Lett.*, **52** (1988), pp. 1103–1105.

(j) *Inelastic Tunneling Spectroscopy STM* (1987), D.P.E. Smith, D. Kirk, C.F. Quate, "Photon Spectra of Molecules in STM", D.P.E. Smith, G. Binning, and C.F. Quate, *Appl. Phys. Lett.*, **49** (1987), pp. 1641–1643.

(k) *Laser Driven STM* (1987), L. Arnold, W. Krieger, H. Walther, "Imaging by Non-linear Mixing of Optical Waves in STM", L. Arnold, W. Krieger, H. Walther, *Appl. Phys. Lett.*, **51** (1987), pp. 786–788.

(l) *Ballistic Electron Emission Microscope* (1988), W.J. Kaiser, "Probing of Schottky Barriers in nm Scale", W.J. Kaiser, *Phys. Rev. Lett.*, **60** (1988), pp. 1406–1409.

(m) *Inverse Photoemission Force Microscopy* (1988), H. Coombs, J.K. Gimzewski, B. Reihl, J.K. Sass, R.R. Schlittler, "Luminescence Spectra on nm Scale", B. Reihl, J.H. Coombs and J.K. Gimzewski, *Surface Science* **1988** (1989), pp. 211–212, 156–164.

(n) *Near Field Acoustic Microscope* (1989), K. Takata, T. Hasegawa, S. Hosaka, S. Hosoki, T. Komoda, "Low Frequency Acoustic Measurements on 10 nm Scale", K. Takata, T. Hasegawa, S. Hosaka, S. Hosoki and T. Komoda, *Appl. Phys. Lett.*, **55** (1989), pp. 1718–1720.

    (o) *Scanning Noise Microscope* (1989), R. Moiler, A. Esslinger, B. Koslowski, "Tunneling Microscopy with Zero Tip-sample Bias", R. Möller, A. Esslinger, and B. Koslowski, *App. Phys. Lett.*, **55** (1989), pp. 2360–2362.
    (p) *Scanning Spin–Precession Microscope* (1989), Y. Manassen, R. Hamers, J. Demuth, A. Castellano, "1 nm (Lateral Resolution) Images of Paramagnetic Spins", Y. Manassen, R.J. Hamers, J.E. Demuth and A.J. Castellano Jr., *Phys. Rev. Lett.*, **62** (1989), pp. 2531–2534.
    (q) *Scanning Ion–Conductance Microscope* (1989), P. Hansma, B. Drake, O. Marti, S. Gould, C. Prater, "500 nm (Lateral Resolution) Images in Electrolyte", P.K. Hansma, B. Drake, O. Marti, S.A. Gould and C.B. Prater, *Science*, **243** (1989), pp. 641–643.
    (r) *Scanning Electrochemical Microscope* (1989), O.E. Husser, D.H. Craston, A.J. Bare, O.E. Hüsser, D.H. Craston and A.J. Bard, *J. Vac. Sci. and Tech.* B: *Microelectronics and Nanometer Structures*, **6** (1989), pp. 1873–1876.
    (s) *Absorption Microscope/Spectroscope* (1989), J. Weaver, H.K. Wickramasinghe, "1 nm (Lateral Resolution) Absorption Images/Spectroscopy", J.M.R. Weaver, L.M. Walpita, H.K. Wickramasinghe, *Nature*, **342** (1989), pp. 783–785.
    (t) *Scanning Chemical Potential Microscope* (1990), C.C. Williams, H.K. Wickramasinghe, "Atomic Scale Images of Chemical Potential Variation", C.C. Williams and H.K. Wickramasinghe, *Nature*, **344** (1990), pp. 317–319.
    (u) *Photovoltage STM* (1990), R.J. Hamers, K. Markert, "Photovoltage Images on nm Scale", R.J. Hamers and K. Markert, *Phys. Rev. Lett.*, **64** (1990), pp. 1051–1054.
    (v) *Kelvin Probe Microscopy* (1991), M. Nonnenmacher, M.P. O'Boyle, H.K. Wickramasinghe, "Contact Potential Measurements on 10 nm Scale", M. Nonnenmacher, M.P. O'Boyle and H.K. Wickramasinghe, *Appl. Phys. Lett.*, **58** (1991), pp. 2921–2923.

10. Wong, S.S., A.T. Woolley, T.W. Odom, J.L. Huang, P. Kim, D.V. Vezenov and C.M. Lieber, (1998), *App. Phys. Lett.*, **73**, pp. 3465–3467.
11. Hong, S., J. Im, M. Lee and N. Cho, (2005), in *Handbook of Microscopy for Nanotechnology*, N. Yao and Z. L. Wang (eds), Kluwer Academic Publishers, New York.
12. Kam, Nadine Wong Shi, Theodore C. Jessop, Paul A. Wender and Hongjie Dai, (2004), *J. Am. Chem. Soc.*, **126(22)**, pp. 6850–6851.
13. Synge, E.H., *Phil. Mag.*, **6** (1928), p. 356, 11 (1931), p. 65, **13** (1932), p. 297.
14. Anshup, J. Sai Venkataraman, Chandramouli Subramaniam, R. Rajeev Kumar, Suma Priya, T.R. Santhosh Kumar, R.V. Omkumar, Annie John and T. Pradeep, (2005), *Langmuir*, **21**, pp. 11562–11567.

Additional Reading

1. Ibach, H., and D.L. Mills, (1982), *Electron Energy Loss Spectroscopy and Surface Vibrations*, Academic Press, New York.

2. Vickerman, J.C., (1997), *Surface Analysis: The Principal Techniques*, John Wiley, Chichester, Sussex.
3. Kolasinski, K.W., (2002), *Surface Science Foundations of Catalysis and Nanoscience*, John Wiley and Sons, Ltd. Chichester.
4. Hufner S., (1995), *Photoelectron Spectroscopy*, Springer-Verlag, Heidelberg.
5. Chen, C.J., (1993), *Scanning Introduction to Tunneling Microscopy*, Oxford University Press.
6. Fadley, C.S., (1978), in *Electron Spectroscopy: Theory, Techniques and Applications*, C.R. Brundle and A.D. Baker (eds), Volume 2, Academic Press, New York.
7. Smith, G.C., (1994), *Surface Analysis by Electron Spectroscopy*, Plenum Press, New York.
8. Kimura, K., S. Katsumata, Y. Achiba, T. Yamazaki and S. Iwata, (1981), *Handbook of HeI Photoelectron Spectra of Fundamental Organic Molecules*, Japan Scientific Societies Press, Tokyo.
9. Willard, H.H., L.L. Merritt, Jr., J.A. Dean and F.A. Settle, Jr., (1986), *Instrumental Methods of Analysis*, VIth Edition, CBS Publishers, New Delhi.
10. West, A.R., (1986), *Solid State Chemistry and its Applications*, John Wiley and Sons, New York.

PART THREE

Diversity in Nanosystems

Contents:

- Fullerenes
- Carbon Nanotubes
- Self-assembled Monolayers
- Gas Phase Clusters
- Semiconductor Quantum Dots
- Monolayer-protected Metal Nanoparticles
- Core-shell Nanoparticles
- Nanoshells

Chapter 3

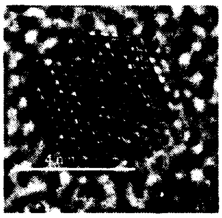

FULLERENES

The science of fullerenes is rather old, but its understanding is important as it has, in many ways, heralded giant leaps in nanoscience. The discovery of these molecules in 1985 opened up a new area of science. Fullerenes are molecular forms of carbon, which are distinctly different from the extended carbon forms known for millennia. There are numerous molecular forms, all of which are spheroidal in structure. We sketch here the fascinating area of this new allotrope of carbon, which may be the only allotrope of any element discovered in the 20th Century, focusing primarily on C_{60}*. The early history, synthesis and characterization, mass spectrometry, derivatization, orientational ordering, pressure effects, superconductivity, magnetism and photophysical properties of fullerenes and fullerene-based compounds are discussed in this chapter. The latest discoveries in this area are delineated at the end.*

Learning Objectives

- What are fullerenes and what are their properties?
- How is the discovery of fullerenes related to the development of nanoscience and technology?
- What are the unusual properties of fullerenes?
- How can gas phase spectroscopy be used to study condensed phase properties?

3.1 Introduction

The role of serendipity in scientific discoveries is widely recognized. The story of buckminsterfullerene (Ref. 1), C_{60} and of fullerenes, in general, is no exception. In their eagerness to understand the chemistry of interstellar molecules, scientists hit upon an unusual and extraordinary discovery in the history of chemistry. The molecule they discovered had 60 equivalent carbon atoms, which formed the pattern of a football that gave it the highest symmetry. Theoretical predictions (Ref. 2) of such structures were known since 1970. In chemistry, there is no other molecule formed by the same atom, which is as big as buckminsterfullerene. For millennia, elemental carbon has been known to occur in two polymorphic forms, graphite and diamond. Graphite has two-dimensional layers of sp^2 hybridized carbon atoms interlinked by weak van der Waals forces. Since its interlayer interaction is weak, graphite is used as a lubricant. Diamond, however, is one of the hardest materials known to man. This property arises from the strong three-dimensional bonding in diamond in which each sp^3 hybridized carbon atom is bonded to four other similar atoms. Fullerenes constitute another allotrope of carbon, which is probably the first allotrope of any element discovered in recent times. Figure 3.1 shows the structures of graphite, diamond and C_{60}. There also exist other all-carbon molecules similar to C_{60} with cage structure, collectively called 'fullerenes' in honour of the famous American architect Buckminister Fuller whose geodesic domes are landmarks of 20th Century architecture. Other forms of carbon such as carbon rings (Ref. 3) are also receiving considerable attention.

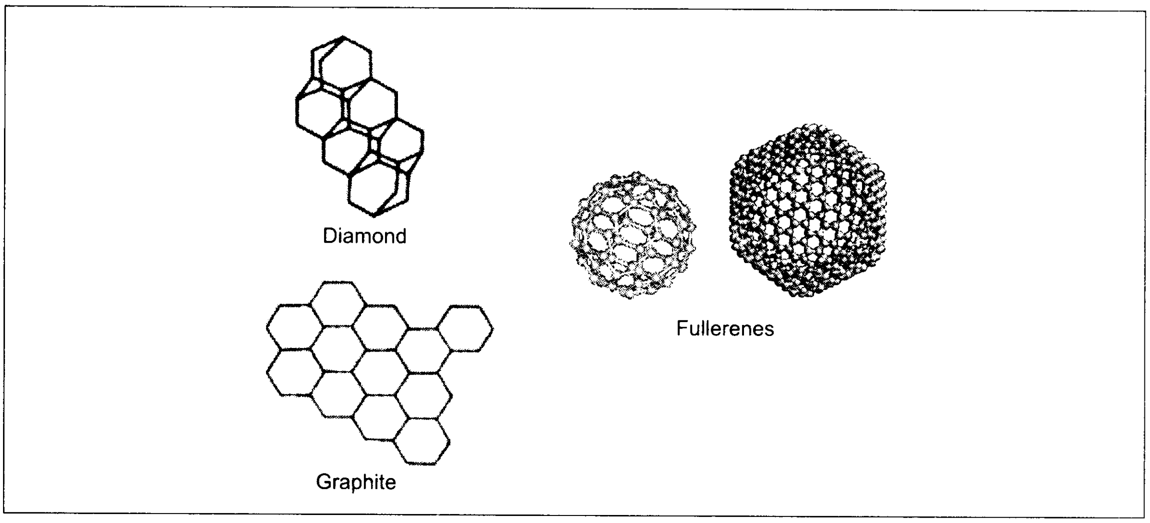

Fig. 3.1: *A schematic representation of the structures of graphite, diamond and fullerenes. While the two-dimensional sheets formed by hexagons are packed one over another in graphite, the diamond structure is three-dimensional. Only two fullerenes are shown. The smaller one is buckminsterfullerene, C_{60}. The bonds between the hexagons are more like double bonds showing the corannulene-type substructure. The double bonds are localized exocyclic to the pentagons giving [5]radialene character to the pentagons and cyclohexa-1,3,5-triene character to the hexagons.*

It is only natural for a molecule of such immense beauty to attract the entire scientific community (Refs 4, 5). The structure, spectroscopy, chemistry, materials science and applications of this molecule have been intensely investigated. Buckministerfullerene thus became the subject matter of nine out of ten of the most cited papers in chemistry in 1991. In 1992, it scored a perfect ten by becoming the subject of ten out of ten papers. According to statistics (Ref. 1), one paper per week got published in this area from 1985 to 1990. After 1990, the figure has risen to one paper per day. In 1995, it was slightly less than two per day. The statistics of the recent years show that this subject continues to attract intense interest. According to webofscience (www.webofscience.com), the number of papers on the subject for the years, 2000, 2001, 2002, 2003, 2004 and 2005 are, 1255, 1350, 1254, 1334, 1313 and 1578, respectively.

Molecules with 70, 76, 82 and other numbers of carbon atoms were soon characterized. The developments in 1991 showed that these molecules are found only with tens and hundreds of atoms but also with thousands of atoms. These giant molecules of carbon occur as nanometer size tubes and balls which are called carbon nanotubes and onions (Ref. 6), respectively. There is another chapter on this topic in this book itself. This chapter, gives an account of the chemistry, physics and materials science of this new form of carbon in a rather illustrative fashion. Numerous conferences have been held on the subject of fullerenes and even on specialized topics of fullerene chemistry and physics over the years. Several books (Refs 4, 5) have appeared on fullerenes and a comprehensive review of these is impossible here.

3.2 Discovery and Early Years

As noted earlier, the search for certain linear molecules of carbon normally found in the interstellar region called cyanopolyynes, was the starting point of this search (Ref. 7). Some of these molecules of the type $H-C\equiv C-C\equiv C-C\equiv N$ or HC_5N, have been synthesized in the laboratory. These molecules contain seven, nine, eleven and even up to 33 carbon atoms. This was the time when Prof. Smalley and his co-workers in Houston were working with a newly developed cluster source (Ref. 8), which used lasers for evaporation, supersonic molecular beam expansion for clustering, and photoionization mass spectrometry for detecting the products. Similar studies were also conducted by Dr. Kaldor and Dr. Cox in Exxon (Ref. 9). Their studies on graphite, which were preceded by those of Smalley and his colleagues, showed the presence of carbon clusters heavier than C_{33}, but interestingly no odd number cluster was seen. Soon after the beginning of these measurements, it was observed that species such as HC_7N and HC_9N are formed in the reaction of $C_n(n < 30)$ with H_2 and N_2. However, the major discovery was not the detection of cyanoplyynes, but of the unusually abundant species C_{60}, which dominated the mass spectrum under certain clustering conditions (Ref. 10). There were other heavier clusters too. It was found that these clusters were particularly unreactive as compared to the lower clusters. Reactivity and photofragmentation studies showed that the 60 atom cluster is extremely stable. The observed chemistry can be explained if one assumes that the graphitic sheets transform into a hollow chicken-wire cage similar to the domes of Buckminister Fuller (Ref. 11). Such a closed cage requires that (Ref. 12) $12 = 3\,n_3 + 2\,n_4 + 1\,n_5 + 0\,n_6 - 1\,n_7 - 2\,n_8 - \ldots$, where n_k represents the number of k-sided faces. For carbon, only values of k are 5 and 6, though 7 is also possible which has been detected in carbon nanotubes (Ref. 13). This means that there should be 12 pentagonal faces and the number of hexagonal faces is arbitrary. In C_{60} there are 12 pentagonal faces and 20 hexagonal faces. Fullerenes, belonging to a class of closed cage molecules, have the general formula C_{20+2n6}. C_{60} has only one chemically distinct carbon atom. However, in C_{70}, there are five distinct carbon atoms. In larger fullerenes, there is the possibility of isomers and some fullerenes are also chiral. It is seen that fullerenes have many more isomers than was previously believed of (Ref. 14). However, because of the isolated pentagon rule (observed generally), in which pentagons are separated by hexagons, the number of isomers is limited.

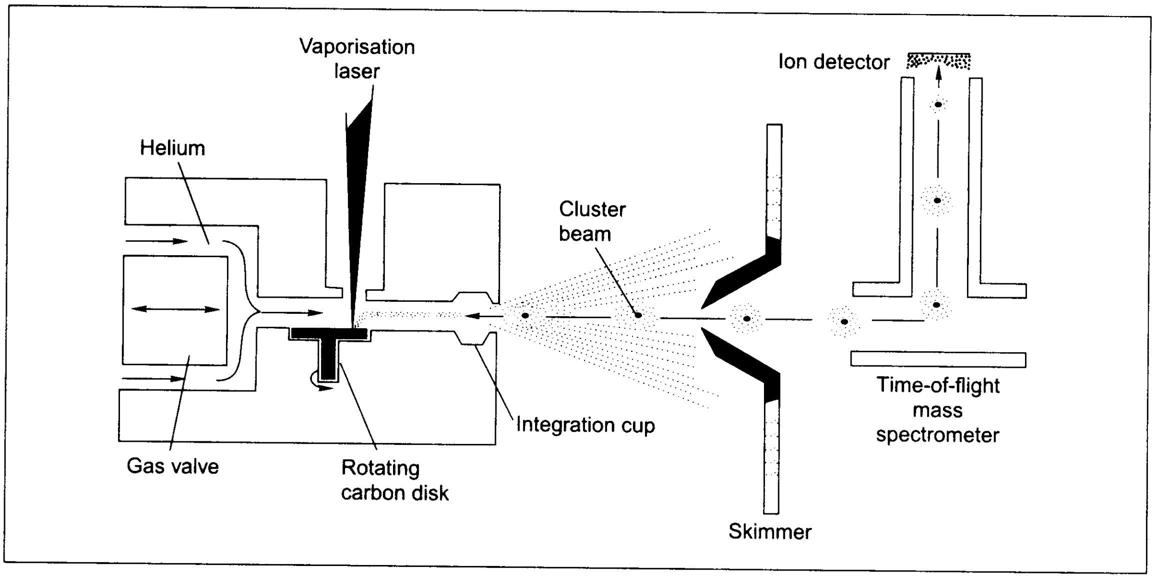

Fig. 3.2: *The experimental set-up used to discover C_{60}. The graphite disk is evaporated with a Nd:YAG laser and the evaporated carbon plasma is cooled by a stream of helium coming from a pulsed valve. The clusters of carbon are produced in the integration cup and are expanded into vacuum. The ions are detected by time of flight mass spectrometry.*

The experimental apparatus used in the discovery of C_{60} is shown in Fig. 3.2. This set-up is now commercially available for the study of a variety of clusters. A rotating disk of graphite is irradiated with a powerful laser to evaporate carbon. As the laser falls on the disk, a stream of helium gas is passed over the disk by releasing a valve. The gas carries the evaporated carbon species with it and during its passage to the nozzle, the species in the vapor undergoes clustering. The cluster beam emanating from the nozzle is selected by a skimmer. The clusters are then subjected to mass analysis by time of flight mass spectrometry. Under certain experimental conditions, the mass spectrum was very similar to that reported previously, showing a distribution of even-numbered species. But a variation in the experimental conditions, especially the introduction of the integration cup (see Fig. 3.2), increased the intensity of the sixty atom cluster to such a point that in some experiments, only C_{60} and C_{70} were seen (Fig. 3.3).

At the same time, experiments were also done using a Fourier transform ion-cyclotron resonance (FT–ICR) apparatus. In these set of experiments, mass selected cluster ions were subjected to reactions with a variety of gases. C_{60}^+ was extremely unreactive to gases such as O_2, NH_3 and NO. On the contrary, a cluster of other elements such as Si showed high reactivity. In fact, there was no evidence to show that Si_{60}^+ was special. A body of other experimental data was accumulated by the Houston group on the photophysics, photodetachment and optical spectrum of C_{60}. None of these studies, however, contradicted the proposed structure.

For nearly five years, C_{60} was truly a playground for chemical physicists. A large number of theoretical papers got published on the electronic structure (Ref. 15), reactivity (Ref. 16), magnetism (Ref. 17) and a

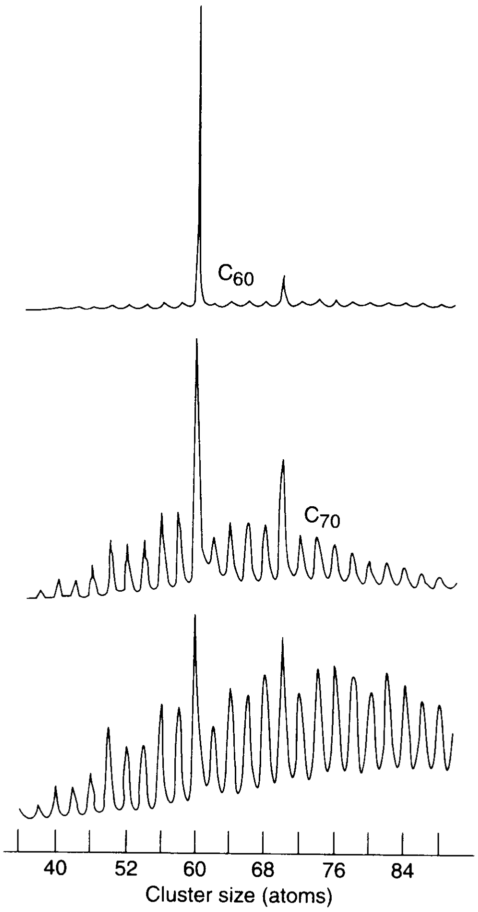

Fig. 3.3: *The mass spectrum of the carbon clusters under various experimental conditions. Under certain conditions, only* C_{60} *and* C_{70} *are seen (Adapted from, Ref. 1).*

number of other properties of C_{60}. The studies were simplified by the very high symmetry of the proposed structure. In fact, a close similarity between the observed peaks in the IR spectrum of an evaporated carbon soot and the theoretical frequencies (Ref. 18) made Kratschmer and his colleagues (Ref. 19) look for C_{60} in the soot. They were working on laboratory-produced carbon soot in order to understand the interstellar spectrum of carbonaceous materials. The soot they obtained after evaporating graphite resistively in an atmosphere of helium contained four bands in the infrared region. The absorption frequencies correlated well the proposed bands of C_{60}. The application of solvent extraction yielded significant quantities of fullerenes (Ref. 20) from the soot and a host of techniques were applied to the characterization of this newly made form of carbon.

3.3 Synthesis and Purification of Fullerenes

For a synthesis of fullerenes, all that is needed is a welding transformer, a chamber connected to a vacuum pump (even a single stage oil sealed rotary pump is adequate) and some graphite rods. The graphite electrodes are brought into close contact with each other and an arc is struck in an atmosphere of 100–200 torr of helium or argon. To sustain the arc, a voltage of 20 V (ac or dc) may be necessary. For a graphite rod of 6 mm in diameter, about 50–200 A current may be consumed. Generally, spectroscopically pure graphite of high porosity is used in order to achieve a high evaporation rate. The soot generated is collected on water-cooled surfaces which could even be the inner walls of the vacuum chamber. After sustaining the arc for several minutes, the vacuum is broken and the soot is collected and soxhlet extracted for about 5–6 hours in toluene or benzene, resulting in a dark reddish-brown solution which is a mixture of fullerenes. Of the entire soot collected in this manner, 20–30 per cent is soluble. This soluble material is subjected to chromatographic separation (Ref. 21). Over the years, several simple methods avoiding time consuming chromatography have been discovered including a filtration technique over an activated charcoal–silica gel column (Ref. 22). About 80 per cent of the soluble material is C_{60}, which can be collected in one pass using toluene as the mobile phase. C_{70} can be separated by using toluene/o-dichlorobenzene mixture as the eluant. Repeated chromatography may be necessary to get pure C_{70}. C_{60} solution is violet in colour while that of C_{70} is reddish-brown. Higher fullerenes such as C_{76}, C_{78}, C_{82}, etc., require HPLC for purification (Ref. 23). The spectroscopic properties of several of these fullerenes are now known. Normally, the preparation of a gram of C_{60} from graphite requires about five hours of work. But it may take as much as 250 hours to make 1 mg in the case the higher fullerenes. C_{60} and C_{70} are now commercially available from several sources. C_{60} costs about $25 a gram but C_{70} is not yet affordable for synthetic chemists. Therefore, a majority of the studies reported are carried out on C_{60}. Fullerenes crystallized from saturated solutions retain solvent molecules, removing which may require long hours of vacuum drying. Crystal growth by vapor transport is an excellent method of growing millimeter-sized crystals devoid of solvent for sensitive measurements. For solid state spectroscopic measurements, it is better to use evaporated fullerene films in high or ultrahigh vacuum to avoid solvent contamination. Evaporation is also used as a method of purification as there are substantial differences in the onset of evaporation between C_{60} and C_{70}. Calixarenes (bowl-shaped macrocycles with hydrophobic cavities) have been used (Ref. 24) in the purification of fullerenes. See Fig. 3.4 for a schematic procedure of the synthesis and purification and fullerenes.

Arc evaporation is not a unique way of making C_{60}. Fullerenes have been found in flames (Refs 25, 26), upon chemical vapor deposition used to produce diamond (Ref. 27), in a 1.85 billion year old bolide impact crater (Ref. 28) as well from spacecrafts (Ref. 29). They have also been made from diamond (Ref. 30). However, no one has made them through chemical reactions though such a possibility has excited many organic chemists (Ref. 31). They have also been synthesized from camphor (Ref. 32). Mass spectrometry has shown that higher clusters of carbons can be formed through the laser evaporation of polymers (Ref. 33). Upon laser evaporation (Ref. 34), highly unsaturated carbonaceous ring systems produce C_{60}. There are several other exotic means of producing C_{60}. However, the total synthesis would indeed be a landmark in chemistry though approaches to this have been suggested (Ref. 35).

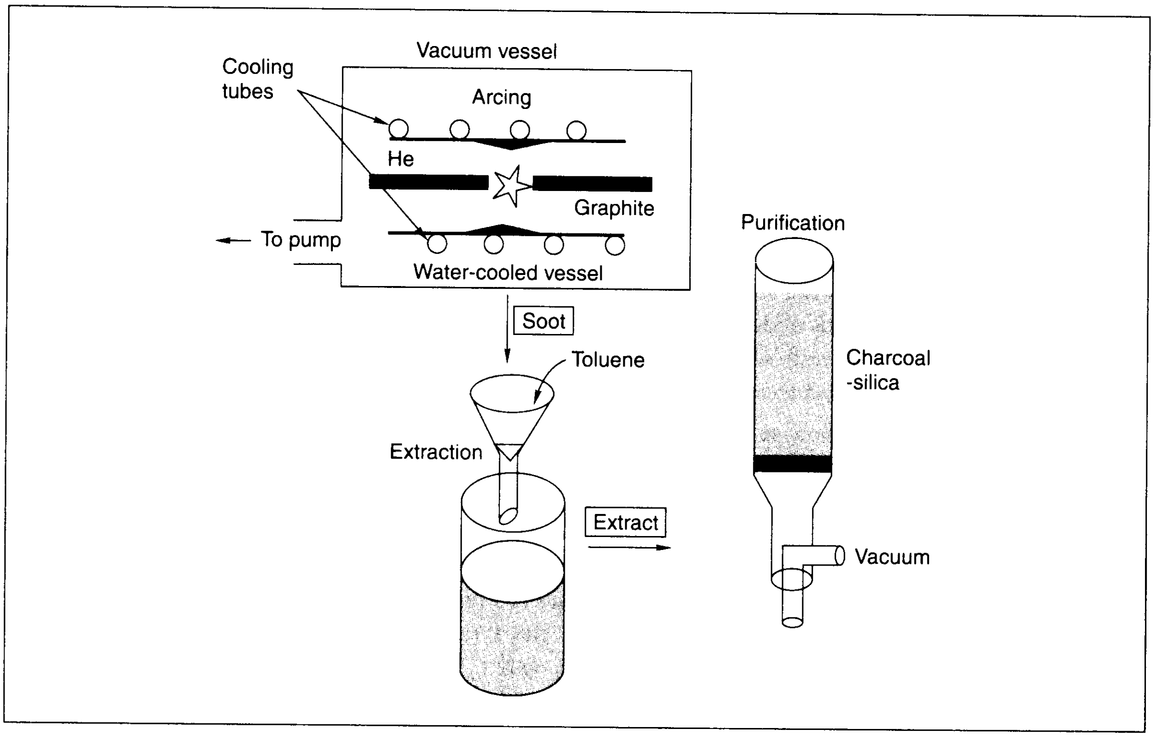

Fig. 3.4: *Schematic illustration of the processes involved in the synthesis and purification of fullerenes. Graphite rods are evaporated in an arc, under He atmosphere. The soot collected is extracted with toluene and subjected to chromatography.*

Synthesis and purification were followed by the characterization of fullerenes in term of a variety of spectroscopic techniques.The pivotal role played by mass spectrometry in characterizing fullerenes cannot be over-emphasized. Other techniques such as NMR showing a single line corresponding to the equivalence of the carbon atoms (Ref. 22), single crystal X-ray structure resolving the atomic positions (Ref. 36), characterization by UV/VIS (Refs 22, 37), IR and Raman (Ref. 38) spectroscopies, etc. soon followed. The predicted electronic structure was confirmed by HeI and HeII photoelectron spectroscopies (Ref. 39).

3.4 Mass Spectrometry and Ion/Molecule Reactions

Soon after a method of macroscopic synthesis of C_{60} was used, several ion/molecule reaction studies were carried out (Ref. 40). In the early days, fullerenes were expensive and a mass spectrometer was the ideal reaction vessel. C_{60}^- and $C_{60}H^+$ were produced by chemical ionization (CI) with methane (Ref. 41). It was shown that C_{60}^- was 15 times more abundant than $C_{60}H^+$, consistent with its high electron affinity. The methane CI spectrum showed protonated fullerenes and adducts of fullerenes with C_2H_5. Collision induced dissociation (CID) of C_{60}^+ in the keV range with helium showed the expected fragments of C_{58}^+, C_{56}^+, etc., just as in the earlier photofragmentation study. CID is a method of activating the ion by collisions with atoms or molecules. The fragmentation of C_{60}^{2+} yielded only C_n^{2+}, not C_n^+ in contrast to polycyclic aromatic hydrocarbons (PAHs), which undergo charge separation reactions. In addition to CID, surface-induced dissociation (Ref. 42) was also performed. This involves the collision of the ion with another surface for imparting energy transfer, which is higher in efficiency than CID. Collisions on both silicon and graphite surfaces showed that C_{60} does not dissociate appreciably at collision energies in the range of 200–300 eV. A number of studies have confirmed this unusual stability of C_{60}, which has been attributed to the 'resilience' of the molecule. Similar properties have been predicted for its hydrides also (Ref. 43). C_{60} collision also leads to delayed ionization and thermionic emission (Ref. 44). Surface collision experiments have been reported on higher fullerenes and metallofullerenes as well (Ref. 45). Mass spectrometry has also been used to study the thermodynamic properties of fullerenes (Ref. 46).

In addition to fragmentation, endohedral complex formation was also observed when high energy collisions were performed (Ref. 47). Eight keV collision of helium with C_{60}^+ produced a number of C_{n+4}^+ mass peaks. When the collision gas was changed to ^{3}He, the peaks shifted by one mass unit showing that the peak was due to the addition of helium atoms to C_{60}. Other scientists conducted experiments in different types of hybrid tandem mass spectrometers and confirmed the results. Ion kinetic energy and CID measurements showed unambiguously that $C_{60}@He^+$ (the @ symbolism implies that the species prior to @ is within the cage of the fullerene after the symbol) is an endohedral complex. Similar measurements were repeated with C_{60}^{2+} and C_{60}^{3+}. C_{70}^+ and C_{84}^+ were also shown to form endohedrals. $C_{60}@Ne^+$ and $C_{60}@Ar^+$ are hard to observe in conventional spectrometers due to large energy losses, but they have been seen in specially designed instruments (see also Section 3.6 on endohedral complexes).

In addition to the work on pure C_{60}, mass spectrometry has been extensively used to characterize the derivatives of C_{60} formed by reactions (Ref. 48). The identification of Birch reduction products of C_{60} was done with electron impact (EI) mass spectrometry. The products of C_{70} were also studied with the help of EI. Reaction products with fluorine showed mass peaks at $C_{60}F_{36}^+$ and $C_{70}F_{40}^+$. These products fragmented with the elimination of F, CF_3 and C_2F_5. Methylated C_{60} showed products with 1 to 24 methyl groups. C_{60} and C_{70} were found to add to aromatic molecules such as benzene, toluene, xylene, anisole and bromobenzene (Ref. 49).

3.5 Chemistry of Fullerenes in the Condensed Phase

Originally it was thought that C_{60} is an aromatic molecule because it has about 12,500 possible resonance structures. However, it should be remembered that in systems where pentagons are near hexagons, the system avoids double bonds in pentagons. The presence of double bonds in pentagons reduces the bond distances, thereby increasing the strain. In the case of C_{60}, there is only one structure which avoids double bonds in pentagons. This means that the delocalization of electrons is poor and C_{60} is poorly aromatic (Ref. 50). This 'poorly aromatic' classification immediately suggests a certain type of chemistry. C_{60} can be visualized in terms of corannulene subunits with two distinct chemical bonds. The 60 6–6 bonds (between hexagons) with a bond length of ca. 1.38 Å, have more double bond character than the 60 6–5 bonds (between pentagons and hexagons) of bond length ca. 1.45 Å, which are more like single bonds. This means that the pentagonal rings are extremely strained and the insertion of a double bond in the 6–5 ring can cause instability to the tune of 8.5 kcal/mol (Ref. 51). However, a description of its chemistry in terms of sub-structures such as radialene and paracyclene (see Fig. 3.1) does not reflect the chemical reality fully since these sub-structures are planar while fullerenes are spherical. Fullerenes are strained and continuous, and describing their chemistry in terms of a strained weakly aromatic molecule may be more appropriate (Ref. 52).

Since fullerenes have only carbon atoms, they cannot be used to achieve substitution reactions. However, such reactions can be achieved on their derivatives. The cage consists of sp^2 hybridized carbon atoms which have –I inductive effect. Therefore, fullerenes strongly attract electrons and react readily with nucleophiles. These reactions are similar to those of poorly conjugated alkenes. A major problem concerns the number of additional products created by each reagent. A given product can also have a large number of structural isomers. In addition, they may have very little solubility in organic solvents. Many of them do not have high stability due to the strain caused by the addition of other products, and therefore, they may revert to the parent fullerenes under mass spectrometric examination. Only a few of them crystallize easily to facilitate single crystal examination. Besides, the study has to be performed with a very small quantity of material, often measured in milligrams, though the situation has improved substantially in recent years. Sometimes, the purification procedures leave only tiny quantities of pure compound at the end. Many a time the purification of isomers becomes very difficult which makes a complete understanding of the chemistry extremely time-consuming, and often impossible. Therefore, a large number of reactions have still not been fully studied. However, there are certain investigations which stand out and have resulted in the creation of unique products. Because of its comparatively easy availability and its unique symmetry, C_{60} has been subjected to more detailed examinations.

Early electrochemical studies have suggested that fullerene C_{60}, undergoes six reversible reductions (Ref. 53) corresponding to the complete filling of the t_{1u} LUMO. The early C_{60} chemistry revolved around this high electron affinity of the cage. Adducts of C_{60} with radicals, nucleophiles, carbenes and dienophiles have been reported. In organometallic chemistry functionalization leading to η^2 complexes of transition metals (Refs 36, 54) was reported early. The alkylation of C_{60} leading to methanofullerenes (Ref. 55) is being intensely pursued by the groups of Wudl, Rubin and Diederich. A detailed account of this can be found in a book by Hirsch (Ref. 4). These reactions have been shown to result in fullerene polymers (Ref. 56), fullerene dendrimers (Ref. 57) (see Fig. 3.5), fullerene-based HIV protease inhibitors (Ref. 58), fullerene nucleotide conjugates (Ref. 59) and a number of other potentially useful materials. The electrochemical and photophysical characteristics of fullerene adducts can be technologically interesting. Although the chemistry of C_{60} has been intensely investigated, that of higher fullerenes is beginning to attract attention. The product distribution is more complex because of the presence of a large number of non-equivalent bonds.

The fullerene cage itself could include other elements such as boron (Ref. 60) and nitrogen (Ref. 61). The evaporation of boron nitride doped graphite disk produced boron doped fullerenes (Ref. 60) such as $C_{60-n}B_n^+$ with $n = 0$ to 6. Photodissociation showed that these species are resistant to fragmentation, but reactions with ammonia showed the acidic behavior of boron atoms. Species such as $C_{60-n}B_n(NH_3)_n^+$

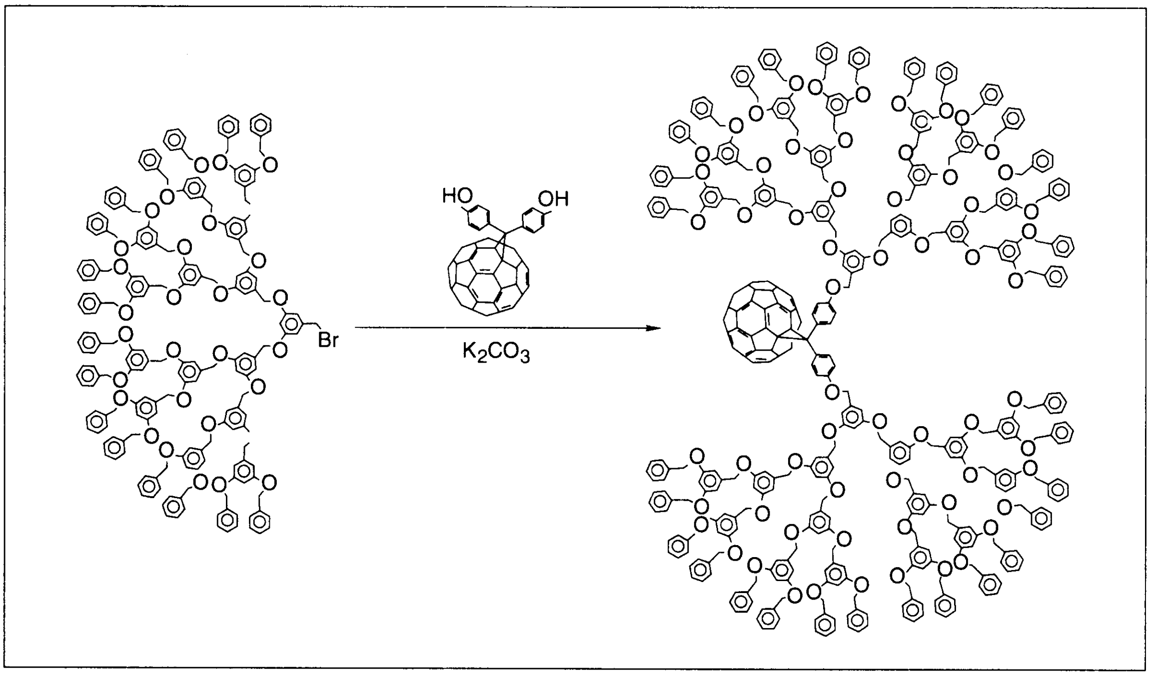

Fig. 3.5: *Schematic showing the synthesis of dendritic methanofullerene, using the established dentritic growth procedures. Reprinted with permission from Wooley, et al. (Ref. 51). Copyright (1993) American Chemical Society.*

were observed showing that boron has been incorporated into the cage. Substituted fullerenes such as $C_{59}NH$ are now prepared by synthetic chemistry (Ref. 62).

Photoionization time of flight mass spectrometry has been used to show that clusters of C_{60} are indeed formed during vaporization (Ref. 63). Intensity anomalies in the mass spectrum have been detected corresponding to $(C_{60})_n^+$ where $n = 13, 19, 23, 35, 39, 43, 46$ and 55. The numbers suggest that the closed shell clusters $n = 13$ and 55 are probably icosahedra. The magic numbers are similar to the clusters of Xe and Ar.

Fullerenes undergo coalescence reactions in the gas phase. In laser evaporation of fullerene films, it was found that the mass spectra show peaks at very high masses above m/z 720 with enhanced intensities in the range of $(C_{60})_n^+$ (Fig. 3.7) (Ref. 64). This proposes the fusion of C_{60} cages to form larger cage structures. The identities of the products were also studied by surface-induced dissociation which showed that the clusters are hard to dissociate and no parent fullerene is formed. This excludes the interpretation that the peaks could be due to difullerene-like structures. The reaction is supposed to be taking place in the excited dense plasma. Similar coalescence reactions have been reported by others also. Another type of reaction which has not been observed before has been the addition of C_{60} and C_2 in the gas phase (Ref. 65). In this study, a C_{60} film was bombarded by high energy ions. The mass spectrum of the produced ions shows peaks at C_{60}, C_{60+2}, C_{60+4}, etc. all the way up to C_{108}, with the mass limit of the instrument as shown in Fig. 3.6. This suggests that the C_n fragments add back to C_{60} in the plasma region immediately above the condensed phase where ion/molecule reactions occur. In fact such addition reactions are known to occur without any activation barrier (Ref. 66).

3.6 Endohedral Chemistry of Fullerenes

The cavity in the 7 Å diameter buckminsterfullerene molecule has intrigued chemists ever since the discovery of fullerenes. Later, Smalley and his colleagues (Ref. 67) showed that laser evaporation of graphite

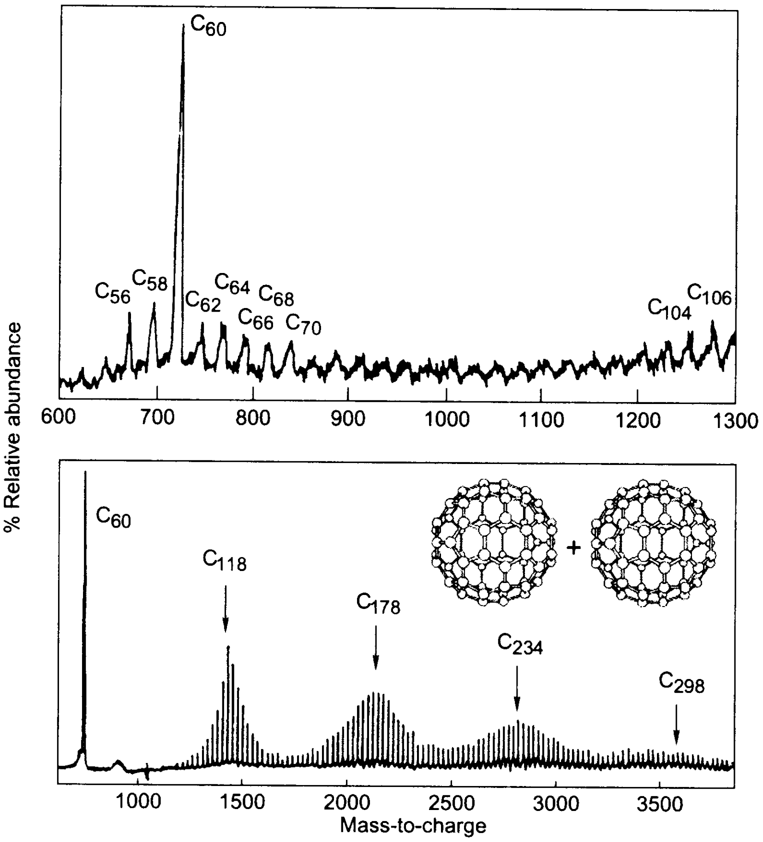

Fig. 3.6: *(Bottom) Mass spectrum of a laser evaporated C_{60} film showing coalescence of fullerenes. Mass peaks are seen at $(C_{60})_n$ (Ref. 64). (Top) Collision of high energy ions on C_{60} results in the addition of C_2s to C_{60}. The mass spectrum here shows the addition of a number of such species (Ref. 65). Combined figure originally published in, T. Pradeep, Current Science, 72 (1997) 124.*

impregnated with La_2O_3 can give $La@C_{82}$ and the product can be extracted in toluene. The molecule was shown to be a radical exhibiting EPR hyperfine structure (Ref. 68). Mass spectral evidence for other endohedrals was soon available. High energy collision experiments involving fullerene ions and noble gases were shown to result in noble gas encapsulated fullerenes (Ref. 47). For a substantial period of time, the characteristic mass spectral fragmentation pattern was the only experimental evidence for the existence of endohedral fullerenes. The fact that He could be put into the cage prompted Saunders to probe the chemistry of endohedrals through ^3He NMR (Ref. 69). $Rg@C_{60}$ (Rg = rare gas) molecules have been synthesized by a high temperature–high pressure method (Ref. 70). Studies showed the high diamagnetic shielding of the inner C_{60} surface indicating the existence of a high degree of aromaticity (Ref. 71). The ^3He endohedral chemistry has been extended to the study of derivatives of C_{60} (Refs 71, 72) and isomers of higher fullerenes (Ref. 15). Results show that there are at least eight C_{78} isomers and nine C_{84} isomers, which is much higher than the number originally suggested. $La@C_{82}$, $La@C_{80}$, $La@C_{76}$ and a number of Y, Sc and Mn endohedrals have been prepared and purified. The electrochemical, electronic and magnetic properties of these materials have been investigated (Refs 73, 74). $Gd@C_{82}$ is paramagnetic down to 3 K (Ref. 75). There are theoretical predictions about the various electronic properties of endohedrals but the experimental confirmation of these predictions is awaited. Another development in the endohedral chemistry is the preparation of $Li@C_{60}$ by low energy ion-beam collision of Li^+ on a C_{60} film (Ref. 76).

3.7 Orientational Ordering

As regards the several properties of fullerenes, a widely investigated aspect is their orientational ordering. Generally molecules of a high point group symmetry crystallize with a certain degree of orientational disorder. Some lower fullerenes are highly spherical and are held together by weak van der Waals forces, and their molecular orientations need not be ordered as in the case of an ordered crystal. This high asymmetry is proved by the fact that large thermal parameters are required to fit the observed diffraction patterns. This asymmetry is the reason why C_{60} had to be fixed with a molecular handle by complexation to refine the atomic positions as was done by Hawkins (Ref. 36).

In the pure form, C_{60} rotates freely in the lattice because of its high symmetry and weak intermolecular interactions. This may lead to interesting properties such as the unusual flow of liquids over C_{60} film (Ref. 77). This rotation can be frozen at low temperatures, resulting in an orientational ordering. Upon reaction or by co-crystallization, which inhibits the free rotation of C_{60} molecules, the atomic positions have been studied. At room temperature, C_{60} gives a sharp NMR signal at 143 ppm and the signal broadens at low temperatures as a result of chemical shift anisotropy (Ref. 78). This is due to the dynamic nature of the disorder, and the orientational correlation times are of the order of 16 picoseconds. The orientationally disordered face centred cubic (fcc) phase undergoes a transition to a simple cubic (sc) phase at 248 K (Ref. 79). In Fig. 3.7, a differential scanning calorimetric trace of the transition is shown. In the sc phase, the rotation exists only along the preferred axis. NMR studies have shown that below the ordering temperature, the molecules jump between preferred orientations over a barrier of 3000 K (Ref. 78). Phase transitions can be modeled which show that simple Lennard–Jones (L–J) potentials reproduce experimental behavior. Charge-transfer effects are, however, important (Ref. 80). Neutron diffraction studies indeed strongly support this suggestion in which it is found that the electron rich bonds of one molecule are located close to the electron poor pentagon rings of the adjacent molecule (Ref. 81).

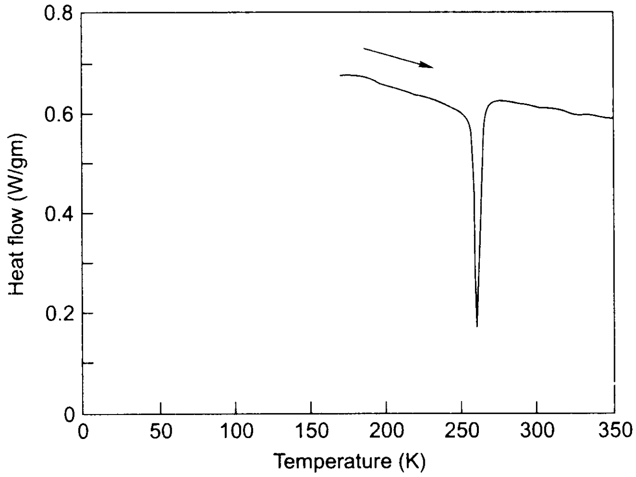

Fig. 3.7: *Results of a different scanning calorimetric measurement of a powder sample of C_{60}. The arrow indicates that the data were taken upon warming. Reprinted with permission from Heiney, et al. (Ref. 79). Copyright (1991) by the American Physical Society.*

Orientational ordering results can be seen in IR and Raman spectroscopies also (Ref. 82). A glassy phase has been observed around 80 K when molecular rotations are completely frozen (Ref. 83). It may be mentioned that many of the derivatives of C_{60} are also spherical and phase transitions of this type may be observed in them. We have (Ref. 84) observed such a transition in $C_{60}Br_{24}$.

C_{70} undergoes two-phase transitions at 337 and 276 K, and these transitions have been studied by IR and Raman spectroscopies (Ref. 85). Diffraction studies suggest a monoclinic structure for the lowest temperature phase and a rhombohedral or hexagonal structure for the in-between phase (Ref. 86). Complete orientational freezing occurs only at 130 K. Upon phase transition, the intramolecular phonons undergo hardening, a general feature observed for both C_{60} and C_{70}. Resistivity measurements have proved that there are two phase transitions in C_{60} and three in C_{70} (Ref. 87).

3.8 Pressure Effects

Both C_{60} and C_{70} are soft solids and their compressibilities are comparable to the c-axis compressibility of graphite. Upon the application of pressure, the orientational ordering temperature increases at a rate of

10 K/kbar (Ref. 88). Around 20 Gpa, C_{60} undergoes a transition to a lower symmetry structure (Ref. 89). Above 22 Gpa, the material undergoes amorphization and the phase shows evidence of sp^3 hybridized carbon. In C_{70}, amorphization take place around 12 Gpa and only sp^2 hybridized carbon is seen (Ref. 99). This suggests that while polymerization via Diels-Alder addition might be taking place in C_{60}, no such reaction occurs in C_{70}. Polymerization upon light irradiation has been observed in C_{60} (Ref. 91). Under extremely high pressures, it is possible to convert C_{60} to diamond at low temperatures (Ref. 92). Such a conversion is seen in C_{70} also.

At fairly low pressures below the amorphization pressure, the photoluminescence band originally at 1.6 eV undergoes a redshift (Ref. 93). At a pressure of 3.2 Gpa, the band merges with the background corresponding to the collapse of the photoluminescent gap. This arises due to the broadening of the HOMO and LUMO which is a result of shortening of the inter-molecular distance and a concomitant increase in the inter-ball hopping integral. This study has repercussions for the low temperature electrical properties found in doped fullerenes.

3.9 Conductivity and Superconductivity in Doped Fullerenes

Doping with potassium, corresponding to the stoichiometry K_3C_{60}, produces a superconductor with a transition temperature of 19.8 K (Ref. 94, 95) (Fig. 3.8). The K_xC_{60} phase was earlier found to be metallic

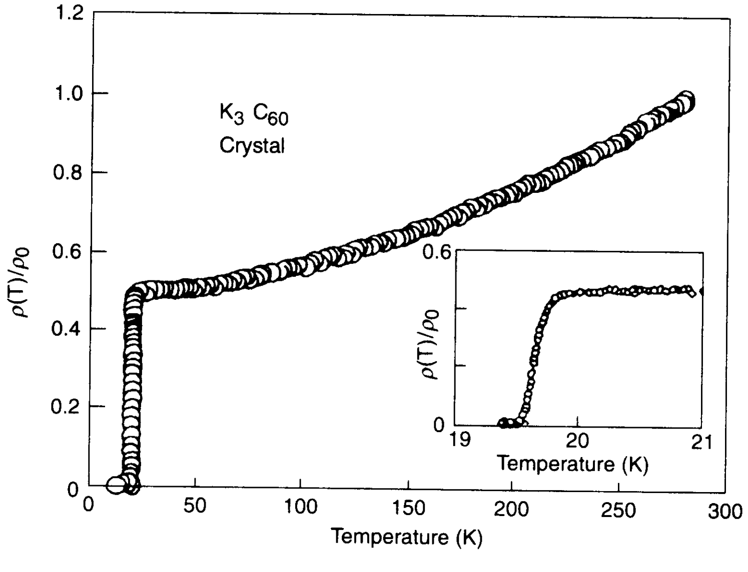

Fig. 3.8: *Normalized DC electrical resistivity ρ(T) of a K_3C_{60} single crystal. The T_c observed is 19.8K. ρ_0 is the resistivity at T = 280 K. Reprinted with permission from Xiang, et al. (Ref. 95). Copyright (1992) AAAS.*

(Ref. 96). It is interesting to note that doping graphite with potassium also results in superconductivity, but at extremely low temperatures. However, the doping of Na and Li does not result in superconductivity, but other alkali metals do produce superconductors with a high transition temperature (T_c).The mixture of metals also shows the same phenomenon. Since the t_{1u} LUMO is triply degenerate, six electrons can be pumped into C_{60}. Six more can be placed in the t_{1g} LUMO.These electrons can be easily transferred from metal atoms placed in the tetrahedral and octahedral voids of fcc C_{60}.The highest T_c organic superconductor, Rb_2CsC_{60}, has a T_c of 31 K (Ref. 97). A_6B_{60}(bcc) and A_4C_{60} (bct) phases are non-superconducting (Ref. 98). Electron spectroscopy shows that the continuous filling of the LUMO takes place upon doping but on prolonged exposure, the LUMO band is shifted below E_f, making it an insulator (Ref. 99). Upon exposure to transition-metals, the *d* states grow near E_f and incomplete metal to C_{60} charge–transfer is observed (Ref. 100). Studies show that T_c is a function of inter-ball separation. Thus, intramolecular phonons are responsible for the superconducting ground states in these materials. Superconductivity in A_3C_{60} has been treated as a special case of the BCS theory with intermediate electron-phonon coupling (Ref. 101). Ca_3C_{60} (Ref. 102), Ba_6C_{60} (Ref. 103) and Sm_3C_{60} (Ref. 104) are superconducting. Superconductivity in higher fullerenes has not been reported probably due to lower symmetry.

3.10 Ferromagnetism in C_{60}.TDAE

Another important property which arises as a result of charge–transfer is ferromagnetism. Organic ferromagnetism is a rare phenomenon and is proved conclusively only in a few systems. So far there is only one donor that is known to produce ferromagnetism as a result of complexation with C_{60}, which is TDAE, tetrakisdimethylaminoethylene (Ref. 105). The T_c observed is 16.1 K, which is the highest T_c found for an organic material. The material belongs to the monoclinic system with short C_{60}–C_{60} contact along the c axis (Ref. 106). The quasi one-dimensional behavior has been suggested by susceptibility measurements also (Ref. 107). Single electron transfer has been confirmed by EPR (Refs 107, 108) and Raman studies (Ref. 109). The magnetic and electrical transport properties of C_{60}.TDAE have been reported on single crystals also (Ref. 110). A number of organic donors have been investigated for potential organic magnetism. Although all of them show pronounced magnetic correlation, no ferromagnetism has been reported (Ref. 111). In C_{60}.TDAE spontaneous magnetization has been verified by the zero-field muon relaxation technique as well (Ref. 112).

3.11 Optical Properties

C_{60} trapped in molecular sieves gives intense red light (Ref. 113). The light-transmitting properties of C_{60} embedded silica films have been investigated (Ref. 114). C_{60} is found to be an interesting material for non-linear optics, especially for third harmonic generation (Ref. 115). It would also be interesting to study C_{60} derivatives in this regard. The third harmonic generation optical susceptibility of C_{70} film is interpreted in terms of the totally symmetric ground state along with two excited states: a one-photon state and a two-photon state (Ref. 116). Photoconduction and photoinduced electron transfer, optical switching properties and second harmonic generation are also thoroughly investigated. Several conferences have devoted exclusive sessions on the subject of photophysics of fullerenes (Ref. 117).

3.12 Some Unusual Properties

In this section, are briefly summarized some of the fascinating discoveries in this area.

C_{60} shows anomalous solubility behavior. Normal solutes show a linear temperature dependence of solubility. In most cases, the solubility increases upon warming. In inorganic systems, unusual phenomena are seen due to solute-solvent interactions. Studies of solubility of C_{60}, studied in a number of solvents, indicate that there is a solubility maximum at near room temperature (Ref. 118) (280 K), dissolution is endothermic below room temperature and exothermic above the latter. The results have been interpreted as occurring due to a phase change in solid C_{60} modified by wetting due to the solvent. The solubility maximum in organic materials is unprecedented.

Ordinarily materials have a critical point above which the distinction between liquid and solid disappears. The liquid is not seen below the triple point where solid and vapor co-exist. C_{60} is one substance in which no liquid phase exists according to theoretical investigations of the phase diagram (Ref. 119), though the question is has still not been resolved (Ref. 120). If at all such a liquid phase does exist, it will be only at high temperatures above 1800 K where the molecules may not be stable.

The functionalization of C_{60} makes it soluble in water and the interaction of organofullerenes with DNA, proteins, and living cells, has been investigated. The interesting biological activity of organofullerenes is due to their photochemistry, radical quenching, and hydrophobicity to form one- to three-dimensional supramolecular complexes (Ref. 121). The cytotoxicity of water-soluble fullerene species is sensitive to surface derivatization. The lethal dose of fullerene changed over seven orders of magnitude with relatively minor alterations in fullerene structure. Under ambient conditions in water, fullerenes can generate superoxide anions and it has been suggested that these oxygen radicals are responsible for membrane damage and subsequent cell death (Ref. 122).

Several new forms of fullerenes have been made. The simplest dimer of C_{60}, namely C_{120}, linked by a cyclobutane ring alone, has been synthesized by the solid-state mechanochemical reaction of C_{60} with potassium cyanide (Ref. 123). X-ray structural analysis shows that the C_4 ring connecting the cages is square rather than rectangular. The dimer dissociates cleanly into two C_{60} molecules on heating, but in the gas phase, during mass-spectrometric measurements, it undergoes a successive loss of C_2 units, shrinking to even-numbered fullerenes such as C_{118} and C_{116} in a sequence similar to that of other fullerenes. The smallest possible fullerene is C_{20}, which consists solely of pentagons. But the extreme curvature and reactivity of this structure make it unstable. While a few isomeric structures, namely bowl and ring, have been identified, no cage structure is known so far. The cage-structured fullerene C_{20} can be produced from its perhydrogenated form (dodecahedrane $C_{20}H_{20}$) by replacing the hydrogen atoms with bromine atoms, followed by gas phase debromination (Ref. 124). The gas phase C_{20} clusters have been characterized by using mass-selective anion photoelectron spectroscopy.

Most of the metallofullerenes prepared so far have been based on C_{82}, and have incorporated most of the lanthanide elements, but there has been some debate about the endohedral nature of these compounds. Various observations such as scanning tunneling microscopy, extended X-ray absorption fine structure, transmission electron micrscopy and electron spin resonance, have strongly suggested that the metal atoms are indeed inside the fullerene cages. There are also theoretical suggestions that endohedrals do exist. However, no structural model has confirmed the endohedral nature of metallofullerenes. The endohedral nature of the metal atom has been proved through the use of synchrotron X-ray powder diffraction of $Y@C_{82}$, (Ref. 125).

Several advances have been made in the synthesis of endohedral fullerenes. One of the most recent ones is the synthesis of C_{60} with molecular hydrogen inside. This has been done by a four-step reaction completely closing an open cage fullerene (Ref. 126).

Notable quantities of C_{60} have been synthesized in 12 steps from commercially available starting materials by using rational chemical methods (Ref. 127). A molecular polycyclic aromatic precursor bearing chlorine substituents at key positions forms C_{60} when subjected to flash vacuum pyrolysis at 1100 °C. No other fullerenes are formed as by-products.

Review Questions

1. What made the discovery of fullerenes possible?
2. What are the principal properties of C_{60}?
3. What is the condition for a geometrical structure to be closed-caged?
4. Due to sphericity, are there specific properties possible with C_{60}?
5. Is it possible to understand the chemistry of C_{60} starting from that of ethylene? If so, what are the differences between the two?
6. Why C_{60} chemistry is investigated in the gas phase?
7. Are the molecules similar to C_{60}, formed by other elements?
8. What are the principal challenges in understanding the chemistry of fullerenes?
9. Are there other closed cage objects formed by carbon? Can one propose a few chemically consistent structures?
10. Why only cages? How about rings and boxes? Are such structures possible and what would be their properties?

References

1. For a historical review of this area see, Aldersey-Williams, (1995), Hugh, (1995), *The Most Beautiful Molecule, The Discovery of the Buckyball,* John Wiley and Sons, Inc., New York.
2. Osawa, E., *Kagaku (Kyoto)*, **25** (1970), p. 854; D.A. Bochvar and E.G. Gal'pern, *Proc. Acad. Sci. USSR*, **209** (1973), p. 239.
3. Hunter, J., J. Fye and M.F. Jarrold, *J. Phys. Chem.*, **97** (1993), p. 3460; Gert von Helden, P.R. Kemper, N.G. Gotts and M.T. Bowers, *Science*, **259** (1993), p. 1300; Gert von Helden, Ming-Teh Hsu, P.R. Kemper and M.T. Bowers, *J. Chem. Phys.*, **95** (1991), p. 3835.
4. Jena, P., B.K. Pao and S.N. Khanna, (1987), *Physics and Chemistry of Small Clusters*, Plenum Press, New York, H.W. Kroto, J.E. Fischer and D.E. Cox, (eds) *The Fullerenes*, Pergamon, Oxford, (1993): W.E. Billups and M.A. Ciufolini, (eds) *Buckminsterfullerene*, VCH, New York, (1993); K.M. Kadish and R.S. Ruoff, (eds) *Fullerenes: Recent Advances in the Chemistry and Physics of Fullerenes and Related Materials*, Electrochemical Society, Pennington, New Jersey, (1994); J. Baggot, *Perfect Summetry: The Accidental Discovery of Buckminsterfullerene*, Oxford University Press, New York, (1994); J. Cioslowski, *Electronic Structure Calculations on Fullerenes and their Derivatives*, Oxford University Press, New York, (1995); M.S. Dresselhaus, G. Dresselhaus and P.C. Eklund, *Science of Fullerenes and Carbon Nanotubes*, Academic, New York, (1996); M.C. Flemings, J.B. Watchman Jr., E.N. Kaufman and J. Giordmaine, (eds) *Annual Review of Materials Science*, **24**, 1994.
5. A. Hirsch, (1994), *The Chemistry of Fullerenes*, Stuttgart, Thieme.
6. S. Iijima, *Nature*, **354** (1991), p. 56; P.M. Ajayan and T.W. Ebbesen, *Nature*, **358** (1992), p. 220.
7. For an account of the early researches in this area, please refer to H.W. Kroto, *Science*, **242** (1988), p. 1139; R.F. Curl and R.E. Smalley, *Science*, **242** (1988), p. 1017.
8. Brucat, P.J., L.S. Zheng, C.L. Pettiette, S. Yang and R.E. Smalley, *J. Chem. Phys.*, **84** (1986), p. 3078; S.C. O'Brien, Y. Liu, Q. Zhang, J.R. Heath, F.K. Tittel, R.F. Curl and R.E. Smalley, *J. Chem. Phys.*, **84** (1986), p. 4074.
9. Rohlfing, E.A., D.M. Cox and A.J. Kaldor, *J. Chem. Phys.*, **81** (1984), p. 3322.
10. Kroto, H.W., J.R. Heath, S.C. O'Brien, R.F. Curl and R.E. Smalley, *Nature*, **318** (1985), p. 162.
11. Marks, R.W., (1960), *The Dymaxion World of Buckminister Fuller*, Reinhold, New York.
12. Jones, D.E.H., *New Sci.*, **3** Nov. (1966). p. 245; D.E.H. Jones, *The Inventions of Daedalus*, Freeman, Oxford, (1982), pp. 118–119.
13. Mackay, A.L. and H. Terrons, *Nature*, **352** (1991), p. 762; T. Lenosky, X. Gonze, M. Tester and V. Elser, *Nature*, **355** (1992), p. 333.
14. Saunders, M., H.A. Jimenéz-Vazques, R.J. Cross, W.E. Billups, C. Gessenberg, A. Gonzalez, W. Luo, R.C. Haddon, F. Diederich and A. Herrmann, *J. Am. Chem. Soc.*, **117** (1995), p. 9305.
15. Haddon, R.C., L.E. Brus and K. Raghavachari, *Chem. Phys. Lett.*, **125** (1986), p. 459; R.L. Disch and J.M. Schulman, **125** (1986), p. 465.

16. Zhang, Q.L., S.C. O'Brien, J.R. Heath, Y. Liu, R.F. Curl, H.W. Kroto and R.E. Smalley, *J. Phys. Chem.*, **90** (1986), p. 525; S.W. McElvany, H.H. Nelson, A.P. Baronowski, C.H. Watson and J.R. Eyler, *Chem. Phys. Lett.*, **134** (1987), p. 214; F.D. Weiss, J.L. Elkind, S.C. O'Brien, R.F. Curl and R.E. Smalley, *J. Am. Chem. Soc.*, **110** (1988), p. 4464.
17. Elser, V. and R.C. Haddon, *Phys. Rev., A* **36** (1987), p. 4579.
18. Santon, R.E. and M.D. Newton, *J. Phys. Chem.*, **92** (1988), p. 2141; Z.C. Wu, D.A. Jelski and T.F. George, *Chem. Phys. Lett.*, **137** (1987), p. 291; A.D.J. Haymet, *J. Am. Chem. Soc.*, **108** (1986), p. 319; D.E. Weeks and W.G. Harter, *J. Chem. Phys.*, **90** (1989), p. 4727.
19. Krätschmer, W., K. Fostiropoulos and D.R. Huffmän, *Chem. Phys. Lett.*, **170** (1990), p. 167.
20. Krätschmer, W., L.D. Lamb, K. Fostiropoulos and D.R. Huffmän, *Nature*, **347** (1990), p. 354.
21. Taylor, R., J.P. Hare, A. Abdul-Sada and H.W. Kroto, *J. Chem. Soc., Chem. Commun.*, **20** (1990), p. 1423.
22. Issacs, L., A. Wehrsig and F. Diederisch, *Hew. Chem. Acta.*, **76** (1993), p. 1231; W.A. Scrivens, P.V. Bedworth and J.M. Tour, *J. Am. Chem. Soc.*, **114** (1992), p. 7917; A. Govindaraj and C.N.R. Rao, *Fullerene Sci. Technol.*, **1** (1993), p. 557.
23. Diederisch, F. and R.L. Whetten, *Acc. Chem. Res.*, **25** (1992), p. 119; F. Diederich, R. Ettl, Y. Rubin, R.L. Whetten, R.D. Beck, M.M. Alvarez, S. Anz, D. Sensharma, F. Wudl, K.C. Khemani and A. Koch, *Science*, **252** (1991), p. 548; K. Kikuchi, N. Nakahara, T. Wakabayashi, M. Honda, H. Matsumiya, T. Moriwaki, S. Suzuki, H. Shiromaru, K. Saito, K. Yamauchi, I. Ikemoto and Y. Achiba, *Chem. Phys. Lett.*, **188** (1992), p. 177.
24. Atwood, J.L., G.A. Koutsantonis and C.L. Raston, *Nature*, **368** (1994), p. 229.
25. Howard, J.B., J.T. Mckinnon, Y. Makarovsky, A. Lafleur and M.E. Johnson, *Nature*, **352** (1991), p. 139.
26. Pradeep, T. and C.N.R. Rao, *Curr. Sci.*, **61** (1991), p. 432.
27. Chow, L., H. Wang, S. Kleckly, T.K. Daly and P.R. Buseck, *Appl. Phys. Lett.*, **66** (1995), p. 430.
28. Becker, L., J.L. Bada, R.E. Winans, J.E. Hunt, T.E. Bunch and B.M. French, *Science*, **265** (1994), p. 642.
29. Radicati di Brozolo, F., T.E. Bunch, R.H. Fleming and J. Macklin, *Nature*, **369** (1994), p. 37.
30. Yosida, Y., *Appl. Phys. Lett.*, **67** (1995), p. 1627.
31. Scott, L.T., M.S. Bratcher and S. Hagen, *J. Am. Chem. Soc.*, **118** (1996), p. 8743.
32. Mukhopadhyay, K., K.M. Krishna and M. Sharon, *Phys. Rev. Lett.*, **72** (1994), p. 3182.
33. Brenna, J.T., W.R. Creasy, *J. Chem. Phys.*, **92** (1990), p. 2269; E.E.B. Campbell, G. Ulmer, B. Hasselberger, H.G. Busmann and I.V. Hertel, *J. Chem. Phys.*, **93** (1990), p. 6900.
34. McElvany, S.W., M.M. Ross, N.S. Goroff and F. Diederich, *Science*, **259** (1993), p. 1594.
35. Mehta, G., S.R. Shah and K. Ravikumar, *J. Chem. Soc., Chem. Commun.*, **12** (1993), p. 1006; G. Mehta, G.V. Sharma, R. Kumar, M.A. Krishna, T.V. Vedavyasa and E.D. Jemmis, *J. Chem. Soc., Perkin Trans.*, **1** (1995), p. 2529.

36. Hawkins, J.M., A. Meyer, T.A. Lewis, S. Loren and F.J. Hollander, *Science*, **252** (1991), p. 312.

37. Aijie, H., M.M. Alvarez, S.J. Anz, R.D. Beck, F. Diederich, K. Fostiropoulos, D.R. Huffmän, W. Krätschmer, Y. Rubin, K.E. Schriver, K. Sensharma and R.L. Whetten, *J. Phys. Chem.*, **94** (1990), p. 8630; J.P. Hare, H.W. Kroto and R. Taylor, *Chem. Phys. Lett.*, **117** (1991), p. 394.

38. Bethune, D.S., G. Meiger, W.C. Tang and H.J. Rosen, *Chem. Phys. Lett.*, **174** (1990), p. 219.

39. Lichtenberger, D.L., K.W. Nebeshy, C.D. Ray, D.R. Huffmän and L.D. Lamb, *Chem. Phys. Lett.*, **176** (1991), p. 203.

40. For a review on the mass spectrometry of fullerenes, see S.W. McElvany and M.M. Ross, *J. Am. Soc. Mass Spectrom.*, **3** (1992), p. 267.

41. McElvany, S.W. and J.H. Callahan, *J. Phys. Chem.*, **951** (1991), p. 6186.

42. Campbell, E.E.B., G. Ulmer, B. Hasselberger, H.G. Busmann and I.V. Hertel, *J. Chem. Phys.*, **93** (1990), p. 6900; R.D. Beck, P. St. John, M.M. Alvarez, F. Diederich and R.L. Whetten, *J. Phys. Chem.*, **95** (1991), p. 8402.

43. Rathna, A. and J. Chandrasekhar, *J. Mol. Struct.*, **327** (1994), p. 255.

44. Campbell, E.E.B., G. Ulmer and I.V. Hertel, *Phys. Rev. Lett.*, **67** (1991), p. 1986.

45. Yeretzian, C., R.D. Beck and R.L. Whetten, *Int. J. Mass Spectrom. Proc.*, **135** (1994), p. 79; R.D. Beck, P. Weis, G. Brauchle and J. Rockenberger, *Rev. Sci. Instr.*, **66** (1995), p. 4188.

46. Baba, M.S., T.S.L. Narasimhan, R. Balasubramanian, N. Sivaraman and C.K. Mathews, *J. Phys. Chem.*, **98** (1994), p. 1333.

47. Weiske, T., D.K. Bohme, J. Hrusak, W. Kratschmer and H. Schwarz, *Angew. Chem. Int. Ed. Engl.*, **30** (1991), p. 884; R.C. Mowrey, M.M. Ross and J.H. Callahan, *J. Phys. Chem.*, **96** (1992), p. 4755; S.W. McElvany, *J. Phys. Chem.*, **96** (1992), p. 4935.

48. Haufler, R.E., J. Conceicao, L.P.F. Chibante, Y. Chai, N.E. Byrne, S. Flanagan, M.M. Haley, S.C. O'Brien, C. Pan, Z. Xiao, W.E. Billups, M.A. Ciufolini, R.H. Hauge, J.L. Margrave, L.J. Wilson, R.F. Curl and R.E. Smalley, *J. Phys. Chem.*, **94** (1990), p. 8634; J.M. Wood, B. Kahr, S.H. Hoke, L. Dejarme, R.G. Cooks and D. Ben-Amotz, *J. Am. Chem. Soc.*, **113** (1991), p. 5907; S.H. Hoke, J. Molstad, B. Kahr and R.G. Cooks, *Int. J. Mass Spectrom. Ion Process.*, **138** (1994), p. 209.

49. Bohme, D.K., *Chem. Rev.*, **92** (1992), p. 1487; S. Petrie, G. Javahery, J. Wang and D.K. Bohme, *J. Am. Chem. Soc.*, **114** (1992), p. 6268; S. Petrie, G. Javahery, H. Wincel and D.K. Bohme, *J. Am. Chem. Soc.*, **115** (1993), p. 6290.

50. Taylor, R. and D.R.M. Walton, *Nature*, **363** (1993), p. 685.

51. Matsuzawa, N., D. Dixon and T. Fukunaga, *J. Phys. Chem.*, **96** (1992), p. 7594.

52. Haddon, R.C., *Science*, **261** (1993), p. 1545.

53. Dubois, D. and K.M. Kadish, *J. Am. Chem. Soc.*, **113** (1991), p. 7773; Q. Xie, F. Arias and L. Echegoyen, *J. Am. Chem. Soc.*, **115** (1993), p. 9818; C. Jehoulet, A.J. Bard and F. Wudl, *J. Am. Chem. Soc.*, **113** (1991), p. 5456.

54. Balch, A.L., V.J. Catalano, J.W. Lee and M.M. Olmstead, *J. Am. Chem. Soc.*, **114** (1992), p. 5455; R.S. Koefod, M.F. Hudgens and J.R. Shapley, *J. Am. Chem. Soc.*, **113** (1991), p. 8957; A.L. Balch, J.W. Lee, B.C. Noll and M.M. Olmstead, *J. Am. Chem. Soc.*, **114** (1992), p. 10984; P.J. Fagan, J.C. Calabrese and B. Malone, *J. Am. Chem. Soc.*, **113** (1991), p. 9408; P.J. Fagan, J.C. Calabrese and B. Malone, *Acc. Chem. Res.*, **25** (1992), p. 134.

55. Suzuki, T., Q. Li, K.C. Khemani, F. Wudl and O. Almarsson, *Science*, **254** (1991), p. 1186.

56. Shi, S., K.C. Khemani, Q. Li and F. Wudl, *J. Am. Chem. Soc.*, **114** (1992), p. 10656.

57. Wooley, K.L., C.J. Hawker, J.M.J. Frechet, F. Wudl, G. Sardanov, S. Shi, C. Li and M. Rao, *J. Am. Chem. Soc.*, **115** (1993), p. 9836.

58. Friedman, S.H., D.L. Decamp, R.P. Sijbesma, G. Srdanov, F. Wudl and G.L. Kenyon, *J. Am. Chem. Soc.*, **115** (1993), p. 6506; R.F. Schinazi, R. Sijbesma, G. Srdanov, C.L. Hill and F. Wudl, *Antimicrob. Agents Chemother*, **37** (1993), p. 1707.

59. Toniolo C., *et al.*, *J. Med. Chem.*, **37** (1994), p. 4558.

60. Guo, T., D. Jin and R.E. Smalley, *J. Phys. Chem.*, **95** (1991), p. 4948.

61. Pradeep, T., V. Vijayakrishnan, A.K. Santra and C.N.R. Rao, *J. Phys. Chem.*, **95** (1991), p. 10564.

62. Keshavarz-K, M., R. Gonzalez, R.G. Hicks, G. Srdanov, V.I. Svdanov, T.G. Collins, J.C. Hmmelen, C. Bellavia-Lund, J. Pavlovich, F. Wudl and K. Holczer, *Nature*, **383** (1996), p. 147.

63. Martin, T.P., U. Naher, H. Schaber and U. Zimmermann, *Phys. Rev. Lett.*, **70** (1993), p. 3079.

64. Yeretzian, C., K. Hansen, F. Diedrich and R.L. Whetten, *Nature*, **359** (1992), p. 44.

65. Pradeep, T. and R.G. Cooks, *Int. J. Mass Spectrom. Ion Process*, **135** (1994), p. 243.

66. Yi, J.Y. and J. Bernholc, *Phys. Rev.*, **B48** (1993), p. 5724.

67. Chai, Y., T. Guo, C. Jin, R.E. Haufler, L.P.F. Chibante, J. Fure, L. Wang, J.M. Alford and R.E. Smalley, *J. Phys. Chem.*, **95** (1991), p. 7564.

68. Johnson, R.D., M.S. de Vries, J. Salem, D.S. Bethune and C.S. Yannoni, *Nature*, **355** (1992), p. 239; T. Suzuki, Y. Maruyoma, T. Kato, K. Kikuchi and Y. Achiba, *J. Am. Chem. Soc.*, **115** (1993), p. 11006.

69. Saunders, M., H.A. Jimenéz-Vazques, R.J. Cross, S. Mroczkowski, M.L. Gross, D.E. Giblin, R.J. Poreda, *J. Am. Chem. Soc.*, **116** (1994), p. 2193; M. Saunders, R.J. Cross, A. Hugo, H.A. Jimenéz-Vazques, R. Shimshi and A. Khong, *Science*, **271** (1996), p. 22.

70. See for a review of rare gas encapsulated fullerenes, Saunders, M., H.A. Jimenéz-Vazques, R.J. Cross and R.J. Poreda, *Science*, **259** (1993), p. 1428; M. Saunders, H.A. Jimenéz-Vazques, R.J. Cross, S. Mroczkowski, D.I. Freedberg and F.A.L. Anet, *Nature*, **367** (1994), p. 256.

71. Saunders, M., H.A. Jimenéz-Vazques, R.J. Cross, W.E. Billups, C. Gesenberg and D. McCord, *Tetrahedron Lett.*, **35** (1994), p. 3869; A.B. Smith III, R.M. Strongin, L. Brard, W.J. Romanow, M. Saunders, H.A. Jimenéz-Vazques and R.J. Cross, *J. Am. Chem. Soc.*, **116** (1994), p. 10831.

72. Saunders, M., H.A. Jimenéz-Vazques, B.W. Bangerter and R.J. Cross, *J. Am. Chem. Soc.*, **116** (1994), p. 3621.

73. Suzuki, T., S. Nagase, K. Kobayashi, Y. Maruyama, T. Kato, K. Kikuchi, Y. Nakao and Y. Achiba, *Angew. Chem. Int. Ed. Engl.*, **34** (1995), p. 1094.
74. Kikuchi, K., S. Suzuki, Y. Nakao, N. Nakahara, T. Wakabayashi, H. Shiromaru, K. Saito, I. Ikemoto and Y. Achiba, *Chem. Phys. Lett.*, **216** (1993), p. 67.
75. Funasaka, H., K. Sakurai, Y. Oda, K. Yamamoto and T. Takahashi, *Chem. Phys. Lett.*, **232** (1995), p. 273.
76. Tellgmann, R., N. Krawez, S.H. Lin, I.V. Hertel and E.E.B. Campbell, *Nature*, **382** (1996), p. 520.
77. Campbell, S.E., G. Leungo, V.I. Srdanov, F. Wudl and J.N. Israelachivili, *Nature*, **382** (1996), p. 520.
78. Yannoni, C.S., R.D. Johnson, G. Meijer, D.S. Bethune and J.R. Salem, *J. Phys. Chem.*, **95** (1991), p. 9.
79. Heiney, P.A., J.E. Fischer, A.R. McGhie, W.J. Romanow, A.M. Denenstein, J.P. McCauley Jr. and A.B. Smith III, *Phys. Rev. Lett.*, **66** (1991), p. 2911.
80. Chakrabarti, A., S. Yashonath and C.N.R. Rao, *Chem. Phys. Lett.*, **215** (1993), p. 591; M. Sprik, A. Cheng and M.L. Klein, *J. Phys. Chem.*, **96** (1992), p. 2027; J.P. Lu, X. P. Li and R.M. Martin, *Phys. Rev. Lett.*, **68** (1992), p. 1551.
81. David, W.I.F., R.M. Ibberson, J.C. Matthewman, K. Prassides, T.J.S. Dennis, J.P. Hare, H.W. Kroto, R. Taylor and D.R.M. Walton, *Nature*, **353** (1991), p. 147.
82. Chase, B., N. Herron and E. Holler, *J. Phys. Chem.*, **96** (1992), 4262; P.H.M. van Loosdrecht, P.J.M. van Bentum and G. Meijer, *Phys. Rev. Lett.*, **68** (1992), p. 1176.
83. Akers, K., K. Fu, P. Zhang and M. Moscovits, *Science*, **259** (1992), p. 1152; F. Gugenberger, R. Heid, C. Meingast, P. Adelmann, M. Braun, H. Wudl, M. Haluska and H. Kuzmany, *Phys. Rev. Lett.*, **69** (1992), p. 3774.
84. Resmi, M.R., L. George, S. Singh, U. Shankar and T. Pradeep, *J. Mol. Struct.*, **435** (1997), p. 11.
85. Varma, V., R. Seshadri, A. Govindaraj, A.K. Sood and C.N.R. Rao, *Chem. Phys. Lett.*, **203** (1993), p. 545; N. Chandrabhas, K. Jayaraman, D.V.S. Muthu, A.K. Sood, R. Seshadri and C.N.R. Rao, *Phys. Rev.*, **B47** (1993), p. 10963.
86. Christides, C., I.M. Thomas, T.J.S. Dennis and K. Prassides, *Europhys. Lett.*, **22** (1993), p. 611; M.A. Verheijin, H. Meeks, G. Meijir, P. Bennema, J.L. de Boer, S. van Smaalen, G. van Tendeloo, S. Amelinckx, S. Muto and J. van Landuyt, *Chem. Phys.*, **166** (1992), p. 287.
87. Ramasesha, S.K., A.K. Singh, R. Seshadri, A.K. Sood and C.N.R. Rao, *Chem. Phys. Lett.*, **220** (1994), p. 203.
88. Samara, G.A., J.E. Schriber, B. Morosin, L.V. Hansen, D. Loy and A.P. Sylwester, *Phys. Rev. Lett.*, **67** (1991), p. 3136.
89. Duclos, S.J., K. Brister, R.C. Haddon, A. Kortan and F.A. Thiel, *Nature*, **351** (1991), p. 380.
90. Chandrabhas, N., A.K. Sood, D.V.S. Muthu, C.S. Sundar, A. Bharati, Y. Hariharan and C.N.R. Rao, *Phys. Rev. Lett.*, **73** (1994), p. 3411; C.N.R. Rao, A. Govindaraj, H.N. Aiyer and R. Seshadri, *J. Phys. Chem.*, **99** (1995), p. 16814.

91. Zhou, P., Z.H. Dong, A.M. Rao and P.C. Eklund, *Science*, **259** (1993), p. 955.

92. Nunez-Regueiro, M., P. Monceau, A. Rassat, P. Bernier and A. Zahab, *Nature*, **354** (1994), p. 289.

93. Sood, A.K., N. Chandrabhas, D.V.S. Muthu, A. Jayaraman, N. Kumar, H.R. Krishnamurthy, T. Pradeep and C.N.R. Rao, *Solid State Commun.*, **81** (1992), p. 319.

94. Hebard, A.F., M.J. Rosseinsky, R.C. Haddon, D.W. Murphy, S.H. Glarum, T.T.M. Palstra, A.P. Ramirez and A.R. Kortan, *Nature*, **350** (1991), p. 600.

95. Xiang, X.D., J.G. Hou, G. Briceno, W.A. Vareka, R. Mostovoy, A. Zettl, V.H. Crespi and M.L. Cohen, *Science*, **256** (1992), p. 1190.

96. Haddon, R.C., A.F. Hebbard, M.J. Rosseinsky, D.W. Murphy, S.J. Duclos, K.B. Lyons, B. Miller, J.M. Rosamilia, R.M. Flemming, A.R. Kortan, S.H. Glarum, A.V. Makhija, A.J. Muller, R.H. Eick, S.M. Zahurak, R. Tycko, G. Dabbagh and F.A. Thiel, *Nature*, **350** (1991), p. 320.

97. Tanigaki, K., T.W. Ebbesen, S. Saito, J. Mizuki, J.S. Tsai, Y. Kubo and S. Kuroshima, *Nature*, **352** (1991), p. 222; S.P. Kelty, Chia-Chun Chen and C.M. Leiber, *Nature*, **352** (1991), p. 223.

98. Chalet, O., G. Ozlanyi, L. Forro, P.W. Stephens, M. Tegze, G. Faigel and A. Janossy, *Phys. Rev. Lett.*, **72** (1994), p. 2721; S. Pekker, A. Janossy, L. Mihaly, O. Chauvet, M. Carrord and L. Forro, *Science*, **265** (1994), p. 1077.

99. Benning, P.J., J.L. Martins, J.H. Weaver, L.P.F. Chibante and R.E. Smalley, *Science*, **252** (1991), p. 1417.

100. Santra, A.K., R. Seshadri, A. Govindaraj, V. Vijayakrishnan and C.N.R. Rao, *Solid State Commun.*, **85** (1993), p. 77; J.H. Weaver, *J. Phys. Chem. Solids*, **53** (1992), p. 1433.

101. Varma, C.M., J. Zaanen and K. Raghavachari, *Science*, **254** (1993), p. 989.

102. Kortan, A.R., N. Kopylov, S. Glarum, E.M. Gyorgy, A.P. Ramirez, R.M. Fleming, F.A. Thiel and R.C. Haddon, *Nature*, **355** (1992), p. 529.

103. Kortan, A.R., N. Kopylov, S. Glarum, E.M. Gyorgy, A.P. Ramirez, R.M. Fleming, F.A. Thiel and R.C. Haddon, *Nature*, **360** (1992), p. 566.

104. Chen, X.H. and G. Roth, *Phys. Rev.*, **B52** (1995), p. 15534.

105. Allemand, P.M., K.C. Hemani, A. Koch, F. Wudl, K. Holczer, S. Donovan, G. Gruner and J.D. Thompson, *Science*, **253** (1991), p. 301.

106. Stephens, P.W., D. Cox, J.W. Lauher, L. Mihaly, J.B. Wiley, P.M. Allemand, A. Hirsch, K. Holczer, Q. Li, J.D. Thompson and F. Wudl, *Nature*, **355** (1992), p. 331.

107. Seshadri, R., A. Rastogi, S.V. Bhat, S. Ramasesha and C.N.R. Rao, *Solid State Commun.*, **85** (1993), p. 971.

108. Tanaka, K., A.A. Zhakidov, K. Yoshizawa, K. Okahara, T. Yamabe, K. Yakushi, K. Kikuchi, S. Suzuki, I. Ikemoto and Y. Achiba, *Phys. Lett.*, **A64** (1992), p. 221.

109. Muthu, D.V.S., M.N. Shashikala, A.K. Sood, R. Seshadri and C.N.R. Rao, *Chem. Phys. Lett.*, **217** (1994), p. 146.

110. Suzuki, A., T. Suzuki and Y. Maruyama, *Solid State Commun.*, **96** (1995), p. 253.

111. 1Klos, H., I. Rystau, W. Schutz, B. Gotschy, A. Skiebe and A. Hirsch, *Chem. Phys. Lett.*, **224** (1994), p. 333.

112. Asai, Y., M. Tokumoto, K. Tanaka, T. Sato and T. Yamabe, *Phys. Rev.*, **B53** (1996), p. 4176.

113. Gu, G., W. Ding, G. Cheng, W. Zang, H. Zen and Y. Du, *Appl. Phys. Lett.*, **67** (1995), p. 326.

114. Maggini, M., G. Scorrano, M. Prato, G. Brusatin, P. Innocenzi, P. Guglielmi, A. Renier, R. Signorini, M. Meneghetti and R. Bozio, *Advan. Mater.*, **7** (1995), p. 404.

115. Kajzar, F., C. Taliani, R. Zamboni, S. Rossini and R. Danieli, (1993), *Proc. Of the SPIE-The Int. Soc. Optical Eng.*, San Diego, U.S.A. 2025, 352 and other papers in the Conference Proceedings.

116. Kajzar, F., C. Taliani, R. Danieli, S. Rossini and R. Zamboni, *Phys. Rev. Lett.*, **73** (1994), p. 1617.

117. See for, e.g., *Proc. of the SPIE-The Int. Soc. Optical Eng.*, (1995) San Diego, U.S.A.

118. Ruoff, R.S., R. Malhotra, D.L. Heustis, D.S. Tse and D.C. Lorentz, *Nature*, **362** (1993), p. 140.

119. Cheng, A., M.L. Klein and C. Caccamo, *Phys. Rev. Lett.*, **71** (1993), p. 1200.

120. Hagen, M.H.J., E.J. Meijer, G.C.A.M. Mooij, D. Frenkel and H.N.W. Lekkerkerker, *Nature*, **365** (1993), p. 425.

121. Nakamura, E., H. Isobe, *Acc. Chem. Res.*, **36** (2003), pp. 807–815.

122. Sayes, C.M., J.D. Fortner, W. Guo, D. Lyon, A.M. Boyd, K.D. Ausman, Y.J. Tao, B. Sitharaman, L.J. Wilson, J.B. Hughes, J.L. West, V.L. Colvin, *Nano Lett.*, **4** (2004), pp. 1881–1887.

123. Wang, G.W., K. Komatsu, Y. Murata, M. Shiro, *Nature*, **387** (1997), pp. 583–586.

124. Prinzbach, H., A. Weller, P. Landenberger, F. Wahl, J. Worth, L.T. Scott, M. Gelmont, D. Olevano, B. von Issendorff, *Nature*, **407** (2000), pp. 60–63.

125. Takata, M., B. Umeda, E. Nishibori, M. Sakata, Y. Saito, M. Ohno, H. Shinohara, *Nature*, **377** (1995), pp. 46–49.

126. Komatsu, K., M. Murata, Y. Murata, *Science*, **307** (2005), pp. 238–240.

127. Scott, L.T., M.M. Boorum, B.J. McMahon, S. Hagen, J. Mack, J. Blank, H. Wegner, A. de Meijere, *Science*, **295** (2002), pp. 1500–1503.

Additional Reading

Recent Books

1. Kadish, K.M. and R.S. Ruoff (eds) (2000), *Fullerenes: Chemistry, Physics, and Technology*, Wiley VCH.
2. Hirsch, A., M. Brettreich and F. Wudl, (2005), *Fullerenes: Chemistry and Reactions*, Wiley VCH.
3. Kroto, H.W., (2002), *The Fullerenes: New Horizons for the Chemistry, Physics and Astrophysics of Carbon*, Cambridge University Press.
4. Guldi, D.M. and N. Martin, (2002), *Fullerenes: From Synthesis to Optoelectronic Properties*, Springer.

5. R. Taylor (ed.) (1995), *The Chemistry of Fullerenes*, World Scientific.
6. Osawa, E., (2002), *Perspectives of Fullerene Nanotechnology*, Springer.
7. Shinar, J., Z.V. Vardeny, Z.H Kafafi (eds) (1999), *Optical and Electronic Properties of Fullerenes and Fullerene-Based Materials.*
8. See also ref. 4.

This work was originally published in, Current Science, **72** (1997) 124.

Chapter 4

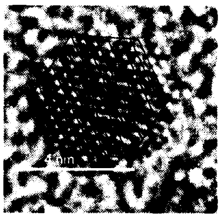

CARBON NANOTUBES

Carbon nanotubes are among the most extensively researched materials today. Research in this area is throwing up numerous surprises. This is the most versatile material, with the properties ranging from optical absorption and emission on one hand to the mechanical properties of bulk materials such as Young's modulus, on the other. The various aspects of science such as chemistry, physics, biology and material science are creating numerous possibilities for application. An overview of carbon nanotubes and their applications is presented here.

Learning Objectives

- What are carbon nanotubes?
- How do you make them?
- What are their properties?
- Can you fill the nanotube?
- What do you use carbon nanotubes for?
- Do carbon nanotubes have industrially relevant applications?

4.1 Introduction

Carbon is responsible for creating the most diverse variety of compounds. It has more allotropes than any other element. The most recent additions to this list are fullerenes and *nanotubes*. The sp^2 hybridized state of carbon makes two-dimensional structures and the most studied of them is its allotrope, graphite. The other well-known allotrope, diamond has sp^3 hybridized atoms. The two-dimensional sheets made of sp^2 hybridized carbon can curl, just like a piece of paper, and make cylinders. By using hexagons alone, carbon cannot yield closed three-dimensional structures. The inclusion of pentagons results in a closed-cage structure; at least six pentagons are needed on each sides of the cylinder, thereby making a closed pipe. This is called a carbon nanotube as the diameter of such a tube is typically in the nanometer range. The tube can be closed or open and the length can be several hundred times the width. The aspect ratio typically encountered is of the order of 100. The longest nanotubes can have lengths of the order of micrometers.

A single sheet of graphite is called graphene. A carbon nanotube is produced by curling a graphene sheet. Just like a sheet of paper, planar carbon sheets can also curl in a number of ways. This makes the carbon sheet helical around the tube axis. If we fold the graphene symmetrically as shown in Fig. 4.1, the hexagons in the resulting tube will be neatly arranged side to side as shown by the arrow. Imagine that the graphene is folded differently, at an angle. This results in a tube in which the hexagons form a coil around the tube axis. One can see that there are infinite ways of folding the graphene sheet, thereby resulting in tubes of different helicities. All these are different kinds of tubes. Since the extent of *helicity* varies, numerous tube structures are possible, which results in both variety and diversity in the properties of the tubes. The electronic structure of the tube also varies as the helicity changes.

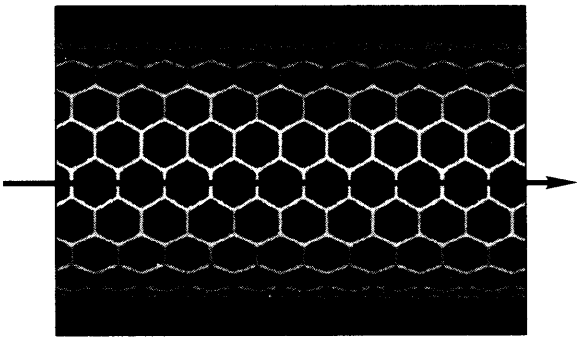

Fig. 4.1 : *A part of the nanotube. The tube is highly symmetrical and is made from a graphene sheet.*

The structure of a cylindrical tube is best described in terms of a tubule diameter d and a chiral angle θ as shown in Fig. 4.2. The *chiral vector* $\mathbf{C} = n\mathbf{a}_1 + ma_2$ along with the two parameters d and θ define the tube. The unit vectors $\mathbf{a}_1$ and $\mathbf{a}_2$ define the graphene sheet. In a planar sheet of graphene (a single sheet of graphite), carbon atoms are arranged in a hexagonal structure, with each atom being connected to three neighbours. In Fig. 4.2, each vertex corresponds to a carbon atom. The vector $\mathbf{C}$ connects two crystallographically equivalent points. The angle θ is with respect to the zigzag axis, and it is 30° for the armchair tube. If we roll over from one end of the tube to the other end, we obtain a cylinder. The rolling can be done in several ways. The bond angles of the hexagons are not distorted while making the cylinder. The properties of the tube get modified depending on the chiral angle θ and the diameter d.

The tubes are characterized by the (n, m) notation, with the tube constructed in Fig. 4.2 being (4, 2). Here the vector $\mathbf{C} = 4\mathbf{a}_1 + 2\mathbf{a}_2$. It is made by making four translations along the zigzag direction and two translations at 120° from the zigzag axis, as shown in Fig. 4.2. There are numerous ways in which the tubes can be rolled. While the $(n, 0)$ tubes are called 'zigzag tubes' where θ is zero, the (n, n) tubes are called 'armchair tubes' where θ is 30°. These two types of tubes have high symmetry and a plane of symmetry perpendicular to the tube axis. Any other tube (n, m) is a chiral tube, which can be either left-handed or right-handed. The tubes will be optically active to circularly polarized light, circulating along the tube axis.

The two important tube parameters, d and θ can be found from n and m.

$d = C/\pi = \sqrt{3}r_{C-C}(m^2 + mn + n^2)^{1/2}/\pi$ and $\theta = \tan^{-1}[\sqrt{3}m/(m + 2n)]$, where $rC\text{-}C$ is the $C\text{-}C$ distance of the graphene layer (1.421 Å) and C is the length of the chiral vector. Due to the symmetry of the graphene layer, several tubes, although having different (n, m) notations are indeed the same. A tube of $(0, n)$ is the same as $(n, 0)$. The tube diameter will increase with an increase in n and m.

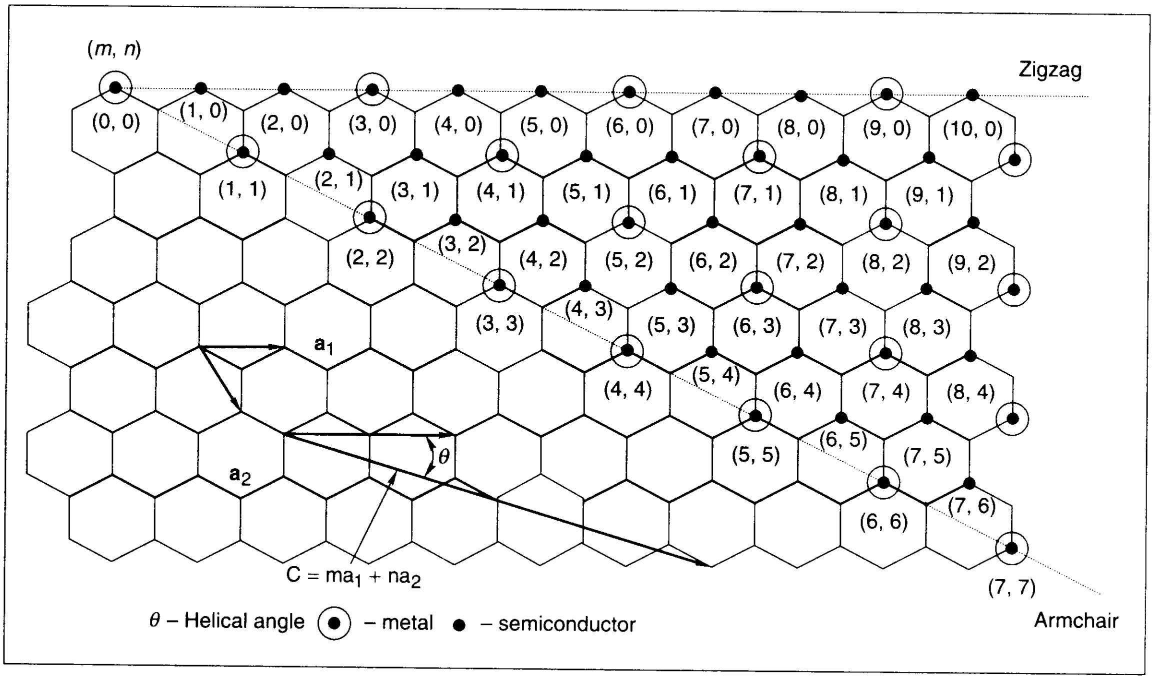

Fig. 4.2: *Illustration of the notations used in understanding carbon nanotubes and the indexing scheme used in carbon nanotubes.*

Hitherto the discussion was confined to single nanotubes, which are called single-walled nanotubes. However, the experimentally observed tubes are also multiwalled, i.e. several tubes are stacked one within the other. In the nanotube assemblies of this kind, there is no three-dimensional order between the graphite layers as in the case of bulk graphite. This is due to the rotational freedom existing between the tubes which is called turbostratic constraint. This lack of three-dimensional order within a multiwalled nanotube (MWNT) has been found in atomically resolved STM measurements. It is not possible to fit any arbitrary tube in a given tube due to lack of space. For a tube to fit into another, there must be a gap of at least 3.44 Å between the layers. We can fit a (10,0) tube in a (19,0) tube, but not in a (18,0) tube. This is because in order to insert a 7.94 Å diameter tube, the larger diameter tube has to have a diameter of 14.82 Å or larger [(7.94) + 2(3.44) Å]. The diameters of (19,0) and (18,0) tubes are 15.09 Å and 14.29 Å, respectively.

4.2 Synthesis and Purification

Carbon nanotubes were first noticed in the graphitic soot deposited on the negatively charged electrode used in the arc–discharge synthesis of fullerenes. In the Kratschmer-Huffman procedure (Ref. 1), the graphite rods are evaporated in a dynamic atmosphere of helium (helium is leaked in while the vacuum system is pumped). Typically a pressure of 130 torr of helium is used and the arc is run at 30 V dc with current being maintained at ~180 A. The carbon deposited on the cathode has a soft inner core and a hard outer cover. The core containing MWNTs is extracted and suspended in suitable solvents. The tubes are seen as empty cylinders lying perpendicular to the electron beam along with amorphous carbon material. The interlayer gap is 0.34 nm, close to the spacing found in graphite. The very first images taken by Iijima (Ref. 2) are shown in Fig. 4.3 along with the imaging geometry. The tube's inner diameter, interlayer spacing, length as also chiral angle θ can be determined from the TEM images. While the first three are straightforward from a high resolution image, the determination of the chiral angle necessitates measurement of the interference pattern of the parallel planes and is usually not done during the routine TEM examination of nanotubes.

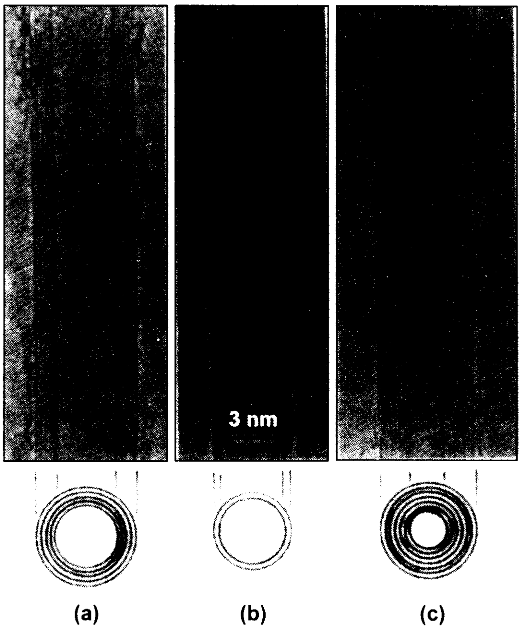

Fig. 4.3: *Multiwalled carbon nanotubes of various diameters observed by Iijima (Ref. 2). Cross-sectional view of the tube is also shown. Copyright Nature.*

Nanotubes are mostly found with closed ends on either side, though open tubes are also seen. Thus these are three-dimensional closed-cage objects, and may be considered as elongated fullerenes. In order to make a closed-cage structure, there must be at least 12 pentagons according to the Euler's theorem, considering only pentagons and hexagons. The hexagons make the elongated body of the tube and the ends contain both hexagons and pentagons, with a minimum of six pentagons on each face. However, the tube body and the ends can have defects. While pentagons result in positive curvature, heptagonal defects result in negative curvature. Both these types of defects have been observed. The former makes a larger tube smaller while the latter can remove this curvature. Various kinds of end tube morphologies have been found, which are illustrated in Fig. 4.4.

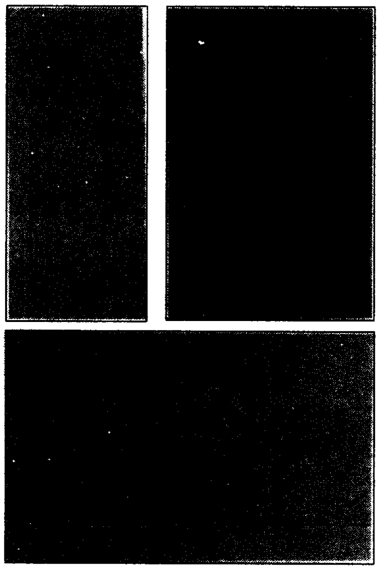

Fig. 4.4: *Transmission electron microscopic images of multiwalled tubes showing the various tip morphologies (Ref. 3). Defects incorporating pentagons (marked 5) and heptagons (marked 7) are shown. While a pentagon gives positive curvature, a heptagon gives negative curvature. Reprinted from Ajayan and Ebessen (Ref. 3). Used with permission from IOP publishing.*

Various modifications to the arc–discharge process are reported in the literature for the synthesis of nanotubes. In the process a smaller diameter (typically 3 mm) anode evaporates on the face of a larger diameter (6 mm) cathode in a direct current arc-discharge apparatus. The bowl that grows on the cathode contains multiwalled tubes. The bowl can be broken and ground, and the nanotubes may be suspended in a suitable solvent and deposited on the TEM grids for examination.

The incorporation of transition metals in catalytic amounts results in the formation of single-walled nanotubes. The catalytic metal is added into the anode. The most common metals used are iron and nickel, but it is better to use a mixture of transition metals. Several bimetallic systems such as Co–Ni, Co–Pt and

Ni–Y have been tried for this purpose. Web-like deposits are found around the cathode or the cooler regions of the reaction vessel. These materials contain significant quantities of single-walled nanotubes. These are seen in the form of ropes containing 5–100 individual SWNTs with amorphous carbon and nanoparticles of the metal/metal–carbon compounds. Optimized synthesis utilizes an Ni–Y catalyst in the atomic ratio of 4:1 and several grams of SWNT containing material can be prepared.

Laser evaporation is another way in which a large yield of SWNTs can be produced (Ref. 4). It is possible of synthesize SWMTs by heating a mixture of graphite with Fe and Ni catalysts at a temperature of 1200 °C and irradiating the material with laser. The yield of the nanotubes is about 50–70 per cent of the product. Nanotubes thus synthesized are found to form ropes in which individual tubes organize into a hexagonal assembly. This clearly shows the homogeneity of the tubes synthesized.

Chemical vapour deposition is another useful way in which the synthesis of SWNTs and MWNTs can be achieved (Ref. 5). Here, an organometallic precursor is mixed with a carbon containing feed gas, it is pyrolyzed in a quartz tube and the nanotubes are collected from the cooler end of the reaction vessel. The feed gas may contain several species and is often mixed with an inert gas. Nanotubes are also grown on solid catalytic substrates such as SiO_2, quartz, alumina, etc., which contain transition metal precursors. Such approaches are important for making supported MWNT assemblies for specific applications. By feeding suitable precursor species, it is possible to incorporate other atoms such as nitrogen into the nanotube structure, by substitution. It is also possible to change the morphology of the tubes by changing the precursors.

Both MWNTs and SWNTs are formed with significant quantities of carbonaceous material. One way of separating the tubes from the carbon mass is to heat-treat the product. Although all the carbon forms react with oxygen, they do so at different rates. All the amorphous carbon materials can be burnt off by heating the soot at 750°C for half an hour (Ref. 6). At the end of this process, only less than 1 per cent of the original material is left, but the product thus obtained is essentially a mixture of nanotubes. The existence of a large number of defects in amorphous carbon make it react at a higher rate, in comparison to nanotubes. Acid-based cleaning procedures can also be used.

In a number of applications, it is important to have aligned nanotubes oriented perpendicular to the surface. One of the approaches that has received significant attention in recent times is the synthesis of aligned nanotube bundles on substrates (Ref. 7). Here a two-furnace approach is used along with metallocenes and organic precursors. Compact aligned nanotube bundles can be obtained by introducing acetylene during the sublimation of ferrocene. Such assemblies grown on substrates, especially in a patterned fashion, have important applications such as field emission displays, see Fig. 4.6 (Plate 4).

4.3 Filling of Nanotubes

The nanotubes obtained directly from the synthetic processes are closed on both the ends. The ends can be opened by suitable chemistry. One of the methods used is acid treatment which oxidizes the ends and leaves behind the oxide containing functionalities. The common functional groups are —COOH and —OH. These may be removed by heating the tubes at 600 °C in flowing Ar. Other methods such as treating with liquid bromine followed by heat treatment, are also used. There are several ways to fill the open tubes with materials. In one, the nanotubes are soaked in a concentrated solution of the desired metal salt, dried and fired in a reducing atmosphere at high temperatures to form metals in the nano form (Ref. 8). This has been done with metals such as Au and Ag. Filling can also be done from the melt of the filling material, if the surface tension is less than 100–200 nN/m. This leads to long crystals of the filled material, filling uniformly inside the tube. A number of different materials are found to be stuck into the nanotube cavity.

There are also other ways of filling nanotubes (Ref. 9). The simplest one is to use the arc evaporation process with graphite anodes filled with appropriate metals. This produces metals or metal carbides inside the tubes. Pyrolysis of organic molecules over metals can also produce MWNTs with metals or metal carbides. In most of such pyrolytic efforts, the objective is to make pure nanotubes by using catalytic processes.

Filled SWNTs have also been made. The general protocol for these is the same as that for MWNTs, with the opening followed by filling with suitable precursor species and firing at the appropriate temperature in a suitable atmosphere. Most of the time, such filling leads to coverage of the filled material both inside as well as over the surface of the nanotube. A selective purification method is thus required to remove the filled material from the outer surface of the nanotube.

Nanotubes may be used as templates to fill materials. In such strategies, the tubes are fired after filling so as to burn off the carbon and obtain nanorods or tubes of the required materials (Ref. 10).

4.4 Mechanism of Growth

The process of nanotube growth has still not been fully understood. The presence of MWNTs and SWNTs in uncatalyzed and catalyzed conditions, respectively, indicate that two different growth mechanisms may be operative. In an open-end mechanism, in which atoms are continuously added to the growing end, the dangling bond energy is stabilized by interaction between the adjacent layers. The bond may be breaking and forming at the periphery of an open-ended tube. In the case of SWNTs, catalysts are important and it appears that catalyst atoms decorate the growing end, which absorb and incorporate the incoming carbon atoms into the nanotube structure. The most recent suggestion (Ref. 11) pertaining to this mechanism is that carbon fibres grow on nickel nanocrystals through reaction-induced reshaping of the particles. The nucleation and growth of the graphene layers occur along with the dynamic formation and restructuring of mono-atomic step edges at the nickel surface. The surface diffusion of carbon and nickel atoms takes place during the growth of the nanotubes.

4.5 Electronic Structure

Nanotubes can have distinctly different electronic properties depending on the chirality. Early calculations predicted that they can be semiconducting or metallic depending on the type of structure. While armchair tubes are always metallic, others can be semiconducting or metallic. Obviously as the diameter increases, tubes resemble graphite, which can be metallic. The curling of the graphite layers and a decrease in the number of layers cause changes in the electronic structure of the metallic tubes, as compared to those of graphite. The presence of defects on the body of the tube can alter the electronic structure and can make regions of specific electronic properties, such as metallic and semiconducting. This would help one make nanoscopic device structures within one tube itself. During one such attempt, a single tube was seen to possess a *y*-junction. Each arm of this tube can have different electrical transport properties, thereby making a transistor possible within one tube (Ref. 12).

Early theoretical studies predicted drastic change in the properties with change in the tube indices. In the figure below (Fig. 4.5) the electronic density of states of (12, 8) and (10, 10) tubes are presented. The density of states shows a distinct gap in the (10, 0) tube, while no gap exists in the (12, 8) tube. Gapless conduction is thus possible in this tube, making it metallic. The (10, 10) tube is semi-conducting and in general, the band gap varies depending on the tube indices.

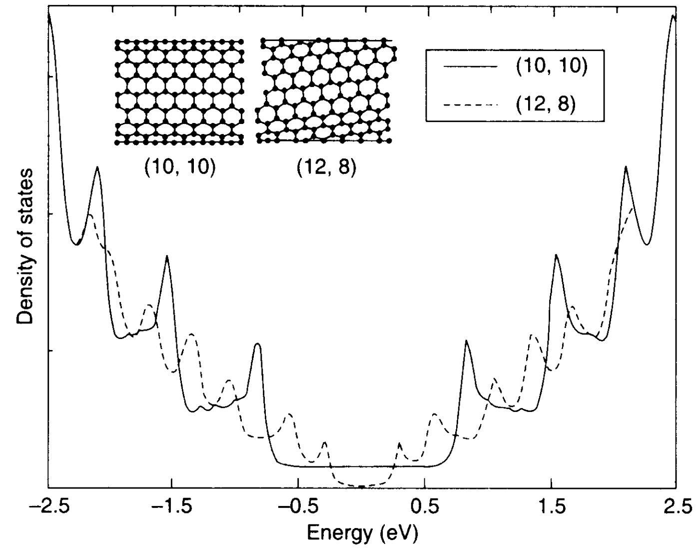

Fig. 4.5: *Calculated electronic density of states for two SWNTs (Ref. 13). The tubes corresponding to the indices (10, 10) and (12, 8) are shown. Used with permission from the author.*

The electronic structure of the tubes has to be probed with tools in order to ensure that nothing else is sampled. This is indeed a difficult task as probes such as photons are typically larger in dimension than the nanotubes. Electron energy loss spectroscopy is thus superior to photon based techniques as the incident electron beam is comparable to the dimensions of the nanotube. In addition to the graphite-like plasmon features at 7 and 25 eV, nanotubes also show features in the range of 10–16 eV. This is attributed to the low dimensionality of the tubes and also to the dimensional cross-over from one to three dimensions.

The 1s resonance in the inner shell electron energy loss spectrum shows features at 285 and 291 eV, due to $1s \rightarrow \pi^\star$ and $1s \rightarrow \sigma^\star$ resonances. These are similar to graphite in MWNTs but are distinctly different in SWNTs (Ref. 14).

Raman scattering is found to be highly diameter-dependent (Ref. 15). There are specific vibrations in the 100–1600 cm^{-1} region which are strongly diameter dependent. The features of specific tubes can be enhanced at specific excitation energies in resonance Raman experiments. This is a manifestation of one dimensionally confined electronic structure. Raman spectroscopy can be used to determine many properties of nanotubes such as tube diameter due to its extreme sensitivity to various tube parameters.

In a synthesis both metallic and semiconducting SWNTs are formed simultaneously. It has been shown recently that chemical processes can be used to separate metallic SWNTs from the others (Ref. 16).

4.6 Transport Properties

Scanning tunneling spectroscopy has shown that the band gaps of the nanotubes vary from 0.2 to 1.2 eV (Ref. 17). The gap varies along the tube body and reaches a minimum value at the tube ends. This is due to the presence of localized defects at the ends due to the extra states. The measurements on SWNTs show the helicity and size-dependent changes in the electronic structure.

The transport properties of MWNTs and NWNTs have been measured (Ref. 18). However, the principal problem in these measurements relates to the need for making proper contacts. Due to large contact resistances, it is not possible to obtain meaningful information without four probe measurements. The conductive behaviour of MWNTs was consistent with the weak two-dimensional localization of the carriers. The inelastic scattering of carriers from lattice defects is more significant than carrier–carrier or carrier–phonon scattering. In SWNTs, conduction occurs through discrete electronic states that are coherent between the electrical contacts (hundreds of nanometers). This means that nanotubes can be treated as quantum wires, at least at very low temperatures.

4.7 Mechanical Properties

The strength of the carbon–carbon bond is among the highest and as a result, any structure based on aligned carbon–carbon bonds will have the ultimate strength. Nanotubes are therefore the ultimate high-strength carbon fibres. The measurement of Young's modulus gave a value of 1.8 TPa (Ref. 19). The theoretical prediction is in the range of 1–5 TPa, which may be compared to the in-plane graphite value of 1 TPa. It is difficult to carry out measurements on individual nanotubes. The problem with MWNTs is that the individual cylinder can slide away thus giving a lower estimate for Young's modulus. It is also possible for individual SWNTs to slip from a bundle, thereby again reducing the experimentally measured Young's modulus. Measurements based on vibration spectroscopy, AFM and transmission electron microscopy can be used in determining estimates, and all of them come up with nearly the same numbers (see Chapter 2).